HOT-WIRE CHEMICAL VAPOUR DEPOSITION OF CARBON NANOTUBES

By

FRANSCIOUS RICCARDO CUMMINGS

Submitted in partial fulfilment of the requirements of the degree of
Magister Scientiae in the Department of Physics,
University of the Western Cape

Supervisor: Dr. C. J. Arendse, Council for Scientific and Industrial Research (CSIR)

Co-supervisors: Prof. D. Knoesen, University of the Western Cape (UWC)
Dr. G. F. Malgas, Council for Scientific and Industrial Research (CSIR)

November 2006

To Melanie

ACKNOWLEDGEMENTS

I am very grateful to the following people and organisations without whose assistance, advice and guidance this thesis would not have been possible.

Dr. Christopher Arendse (Nano Research Group, CSIR) for the excellent supervision of this thesis, his guidance, encouragement, friendship and for the many stimulating discussions.

Prof. Dirk Knoesen (Department of Physics, University of the Western Cape), who acted as co-supervisor, for his constant encouragement and interest in my progress.

Dr. Gerald Malgas (Nano Research Group, CSIR), who also acted as co-supervisor during my period at the CSIR, for his guidance, friendship and many fruitful discussions.

The late Dr. Terence Marais, for unlocking my love for physics research and his constant motivation and interest in my career.

The staff of the Physics Department, University of the Western Cape, for their support and encouragement.

The Energy and Processes Competence Area of the CSIR, who granted me the opportunity to conduct research at one of the most outstanding research institutes.

To my immediate, extended family and friends, for their encouragement and support:

To my mother and grandmother for their believe in me and always inspiring me to greater things!

Melanie for your continuous love, support in time of need and constant encouragement.

Barry, Merle, Christina, Zonika, Candice, Tessa, Rico, Joeharr, Gail, Carmen, Lee-Ann, Junior, Shannique, Setta, Jenera, Lionel, Medwin, Clayton, Candice for being there in my time of need when your support was truly needed.

Theophillus, Grant M, Grant T, Reagan, Eric, John S, Joshwayne, Mervyn, Carlos, Daniel, John B, Darrel, Brendon, Clive, David, Sidwill, Bradwill.

The National Research Foundation (NRF), iThemba Labs, University of the Western Cape and the Council for Scientific and Industrial Research for the financial support during this study.

To the Big Man above, my Creator and God Almighty!

Thank You!

DECLARATION

I declare that

‘‘HOT-WIRE CHEMICAL VAPOUR DEPOSITION OF CARBON NANOTUBES’’

is my own work, that it has not been submitted for any degree or examination in any other university, and that all the sources I have used or quoted have been indicated and acknowledged by means of complete references.

Franscious Riccardo Cummings **November 2006**

Signature: ……..

KEY WORDS

HOT-WIRE CHEMICAL VAPOUR DEPOSITION OF CARBON NANOTUBES

FRANSCIOUS RICCARDO CUMMINGS

Nano-structures

Carbon Nanotubes

Hot-Wire Chemical Vapour Deposition

Raman Spectroscopy

Scanning Electron Microscopy

X-Ray Diffraction

Graphitization

Nano-islands

Structural Perfection

Nanoscience

Aspect Ratio

Field Emission

ABSTRACT

HOT-WIRE CHEMICAL VAPOUR DEPOSITION OF CARBON NANOTUBES

FRANSCIOUS RICCARDO CUMMINGS

M.Sc. Thesis, Department of Physics, University of the Western Cape

Carbon nanotubes (CNTs) can be described as graphene sheets rolled up to form a tube and exist in two forms; single-wall (SWCNTs) or multi-wall carbon nanotubes (MWCNTs). Three main synthesis techniques exist for CNTs, namely arc-discharge, laser vaporisation and chemical vapour deposition (CVD).

Currently, researchers are unable to predict the growth of CNTs in either single or multi-wall form, resulting from the inability to accurately control the deposition parameters of the underlying synthesis technique. However, due to its repeatable and controllable nature, the hot-wire chemical vapour deposition (HWCVD) technique has been identified as a possible solution to the current dilemma faced by CNT researchers. In addition, due to its gas phase nature, HWCVD is also identified as an industrially applied technique for the mass production of CNTs.

In this study we report on the effect of the deposition parameters on the morphology and structural properties of CNTs, synthesized by means of the hot-wire chemical vapour deposition technique. SEM, Raman and XRD results show that the optimum deposition conditions for the HWCVD synthesis of aligned MWCNTs, with diameters between 50 and 150 nm and lengths in the micrometer range are: Furnace temperature of 500 ºC, deposition pressure between 150 and 200 Torr, methane/hydrogen dilution of 0.67 and a substrate-to-filament distance of 10 cm.

November 2006

TABLE OF CONTENTS

CHAPTER ONE

Background of Carbon Nanotubes

1.1 Discovery

Up until 1985 only two types of all-carbon crystalline structures were known to scientists, namely the naturally occurring allotropes of diamond and graphite. In August of that year Harry Kroto, of the University of Sussex, Richard Smalley and Robert Curl, both of Rice University in Houston, collaborated on a set of experiments involving graphite vaporization by means of a high-powered laser. Using mass spectrometry, they discovered a new allotrope of carbon, the fullerenes, with C_{60} (also known as the Buckminsterfullerene) the dominant species. The C_{60} fullerene contains precisely sixty carbon atoms in a closed, spherical structure of high stability and symmetry, as shown in Figure 1.1. The Smalley group received the Nobel Prize in 1996 for this groundbreaking work [1.1].

The synthesis technique of Kroto *et al*. was intricate and yielded very small amounts of C_{60}. This led to scientists Wolfgang Kratschmer of the Max Planck Institute, Donald Huffman of Arizona University and their co-workers to follow up on the Kroto-Smalley experiments, using a simple carbon arc to vaporise the graphite. Their work yielded far greater amounts of C_{60}, with much less effort. Kratschmer *et al*. demonstrated with their simple technique that C_{60} could be manufactured in ordinary experimental laboratories, as it was previously believed that fullerenes could only be synthesised with complicated techniques. Their work was published in Nature in 1990 [1.2].

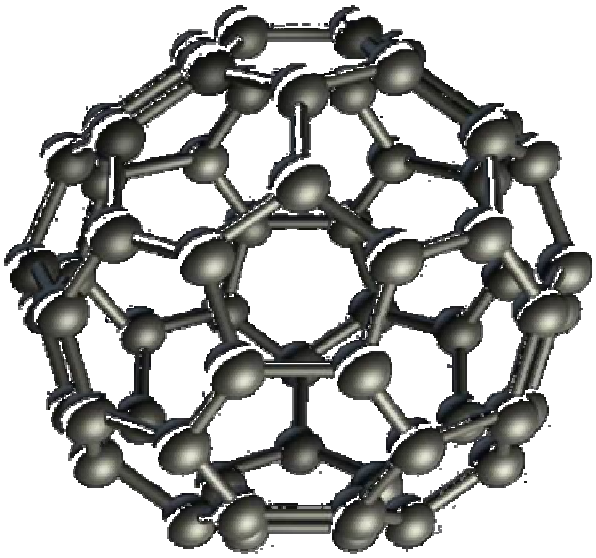

Figure 1.1: Buckminsterfullerene containing 60 carbon atoms [1.1]

Fascinated by the work done by Kratschmer and Huffman, electron microscopist, Sumio Iijima of the Nippon Electric Company, Ltd. (NEC) laboratories in Japan, set pursuit on a detailed high resolution transmission electron microscopy (HRTEM) study of the soot produced by their experiments. After months of research Iijima eventually discovered that the hard, cylindrical residue, which formed on the graphite cathode after evaporation (usually discarded as waste), contained a whole range of novel graphitic structures. Of these new structures, the most noticeable were the long, hollow fibres, which were finer and more perfect than any other previously reported. These new structures, shown in Figure 1.2 were later on christened multi-wall carbon nanotubes (MWCNTs). They can be visualised as 'molecular carbon fibres' consisting of tiny concentric cylinders of graphite closed at each end with half a C_{60} fullerene cap. Iijima's work was published in November of 1991 and created an excitement amongst fullerene scientists the world over [1.3 -1.5].

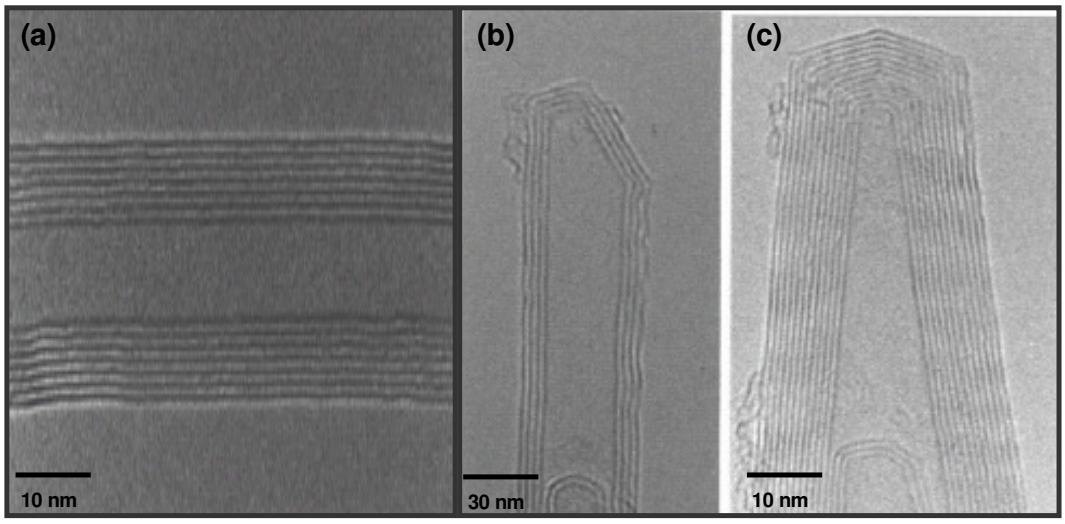

Figure 1.2: HRTEM micrographs of (a) the cross section of a MWCNT, showing the different walls, (b) non-symmetrical and (c) symmetrical end-caps of MWCNTs [1.3]

Almost two years after his discovery of MWCNTs, Iijima and his group discovered single-wall carbon nanotubes (SWCNTs). These structures are considered as the fundamental structure for carbon nanotubes as it consists of a single sheet of graphite (graphene) rolled-up to form a cylinder. This cylinder is then end-capped by a C_{60} hemisphere, as shown in Figure 1.3 [1.6].

1.2 Carbon Nanotube Structures

As mentioned above, carbon nanotubes (CNTs) can be visualised as graphene sheets 'rolled' into a tube and closed at the ends by a C_{60} fullerene cap. It has been shown by various scientists (e.g. [1.5]) that the structural properties entirely depend on the direction in which the graphene sheet is rolled along a certain axis.

Figure 1.3 shows the two possible high symmetry structures for single-wall carbon nanotubes, namely (a) the 'armchair' and (b) 'zigzag' structure. These structures are determined by the way in which the hexagons are arranged

around the tube axis. In practice, however, nanotubes aren't this highly symmetric and are found in 'chiral' structures, in which the hexagons are helically arranged around the tube axis, as shown in Figure 1.3 (c). Chirality refers to a nanotube structure which does not have mirror symmetry.

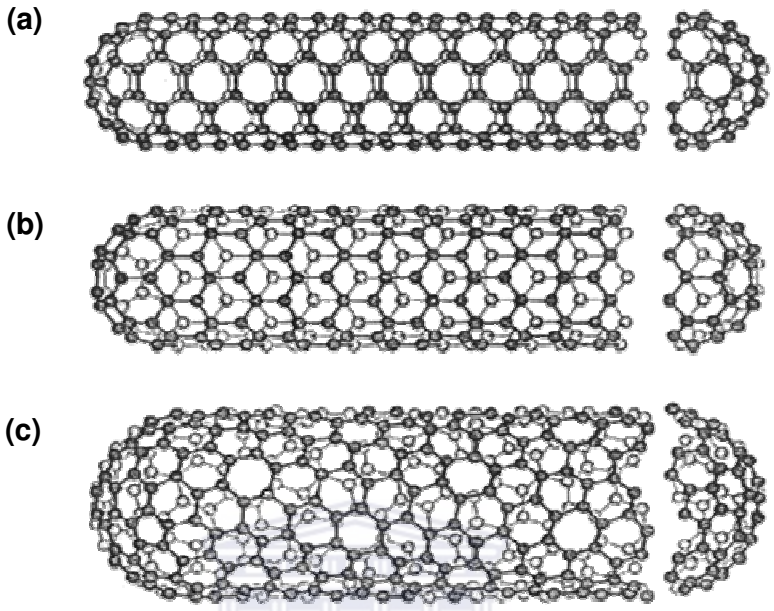

Figure 1.3: Single-wall carbon nanotube structures: (a) armchair, (b) zigzag and (c) chiral structure [1.6]

1.2.1 Single-Wall Carbon Nanotubes

The structure of an individual nanotube is described by the chiral vector, $\vec{C}$ joining two equivalent points on the original graphene lattice and the chiral angle, θ [1.7 – 1.10]. Equivalence means that when the graphene sheet is rolled up to produce a cylinder, these two end-points are superimposed, thus making the magnitude of $\vec{C}$ the circumference of the tube. The schematic of Figure 1.4 shows that $\vec{C}$ can be expressed as

$$\vec{C} = n\hat{a}_1 + m\hat{a}_2 \qquad (1.1)$$

where $\hat{a}_1$ and $\hat{a}_2$ are the graphene unit cell base vectors and each pair of integers (n, m) represents a possible tube structure, with n ≥ m. Figure 1.4 also shows that the vectors (n, 0) and (0, m) represent zigzag tubes, whereas the (n, n) vector produces armchair tubes, and all other vectors (n, m) result in chiral tubes. Now, $|\hat{a}_1| = |\hat{a}_2| = \sqrt{3}\, a_{c\text{-}c}$, = 0.246 nm where $a_{c\text{-}c}$ is the C-C bond length, equal to 1.42 Å [1.8]. Thus, from equation (1.1), the magnitude of $\vec{C}$, in nanometers, is given by

$$\left|\vec{C}\right| = 0.246\sqrt{n^2 + nm + m^2} \qquad (1.2)$$

resulting in a tube diameter length, d_t, given by $|\vec{C}|/\pi$.

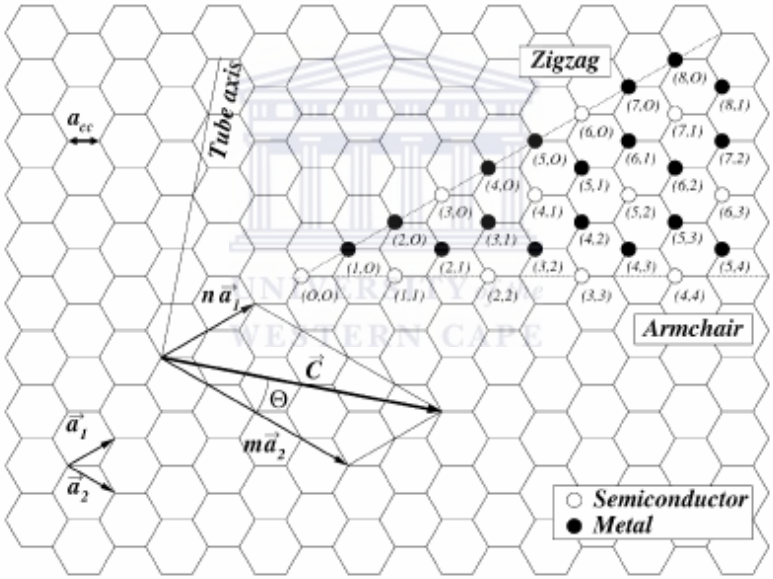

Figure 1.4: Nomenclature of CNTs. Also shown is the definition of the chiral vector and angle on the graphene sheet [1.7]

By making use of geometry the chiral angle θ, which determines the amount of twist in the tube [1.9], is obtained by the expression [1.10],

$$\theta = \tan^{-1} \frac{\sqrt{3}n}{2m+n} \qquad (1.3)$$

From equation (1.3) and Figure 1.4 it follows that θ = 30º for the (n, n) armchair nanotube and that the (n, 0) zigzag tube would result in θ = 60º. However, if θ is limited between 0º ≤ θ ≤ 30º, then by symmetry θ = 0º for all zigzag nanotubes, θ = 30º for all armchair nanotubes and 0º < θ < 30º for chiral carbon nanotubes.

The rectangle formed in Figure 1.5 by the chiral vector $O\vec{A} = \vec{C}$ and the translation vector $O\vec{B} = \vec{T}$ determines the unit cell of the one-dimensional (1D) lattice. For armchair nanotubes the width of this cell is equal to the magnitude of $\hat{a}_1$, the unit vector of the original 2D graphene lattice, whereas zigzag carbon nanotubes will have a unit cell width of $\sqrt{3}a$.

Dresselhaus *et al*. [1.8 – 1.10] who have performed numerous studies on the structure of carbon nanotubes, have calculated expressions for the magnitude of the translation vector, T, in terms of the chiral vector length, C and the highest common divisor of n and m, d_H. These expressions for T then subsequently lead to an expression for N, the number of hexagons per unit cell.

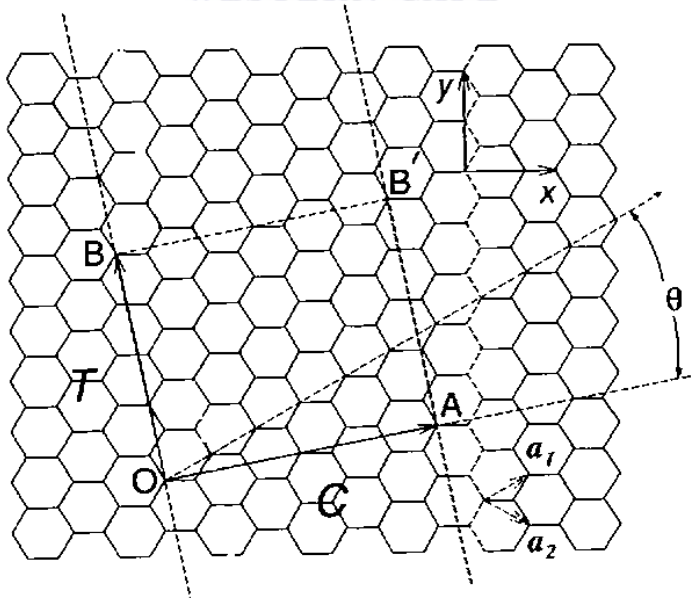

Figure 1.5: Definition of the unit cell for carbon nanotubes [1.8]

According to the calculations by the Dresselhaus group, the expression for T and N is respectively given by

$$T = \frac{\sqrt{3}C}{d_H}$$

and

$$N = \frac{2\left(n^2 + nm + m^2\right)}{d_H} \qquad (1.4)$$

if n – m is not a multiple of $3d_H$. However, if n - m is a multiple of $3d_H$, then

$$T = \frac{\sqrt{3}C}{3d_H}$$

and

$$N = \frac{2\left(n^2 + nm + m^2\right)}{3d_H} \qquad (1.5)$$

Each hexagon contains 2 carbon atoms, thus the unit cell of a carbon nanotube has 2N carbon atoms. Using these expressions the diameter and unit cell parameters of the nanotube can be calculated, which then also determines the properties of the CNT.

1.2.2 Multi-Wall Carbon Nanotubes

The structural relationship between the concentric layers of a multi-wall carbon nanotube has been investigated by Zhang and his co-workers [1.11] as well as Reznik *et al*. [1.12]. Graphene sheets are separated by a distance approximately 0.334 nm, as shown in Figure 1.6. Therefore, if they are rolled to produce cylinders the distance in their circumference should be 2π x 0.334nm ≈ 2.1nm. However, for a zigzag tube with a circumference of $|\vec{C}| = n|\vec{a}|$ = n x (0.246 nm), it can be seen that 2.1 nm is not a multiple of 0.246 nm. However, calculations by the Zhang group, confirmed by Reznik *et al*. showed that the correct separation distance for concentric zigzag CNTs is obtained if the cylinders differ by nine rows of hexagons, resulting in an inter-tube distance of 0.352 nm as shown in Figure 1.7.

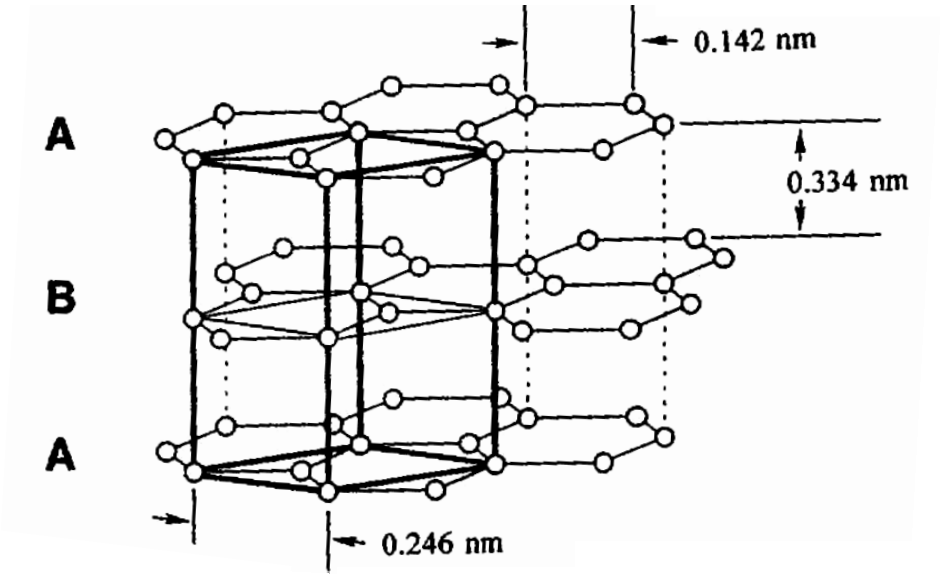

Figure 1.6: The structure of graphite, showing the unit cell and interlayer spacing [1.8]

Figure 1.7 gives a schematic representation of a three-layered zigzag nanotube, where the bold, V-shaped lines indicate the nine and eighteen extra rows of hexagons added to the middle and outer tubes, respectively. The Figure also shows that the ABAB stacking of perfect graphite is not maintained over great distances, but only over the regions where the extra atoms have been inserted.

Multi-walled structures can be assembled in the ABAB stacking arrangement with an interlayer distance of 0.34 nm for armchair CNTs. This is permissible since the ideal circumference of 2.1 nm is a good approximation to 5 x 0.426 nm, where 0.426 nm $= \sqrt{3}a$, the length of the repeat unit of an armchair CNT. For chiral nanotubes things are a bit more complicated and in general it is not possible to have two tubes with exactly the same chiral angle separated by the graphite interplanar distance.

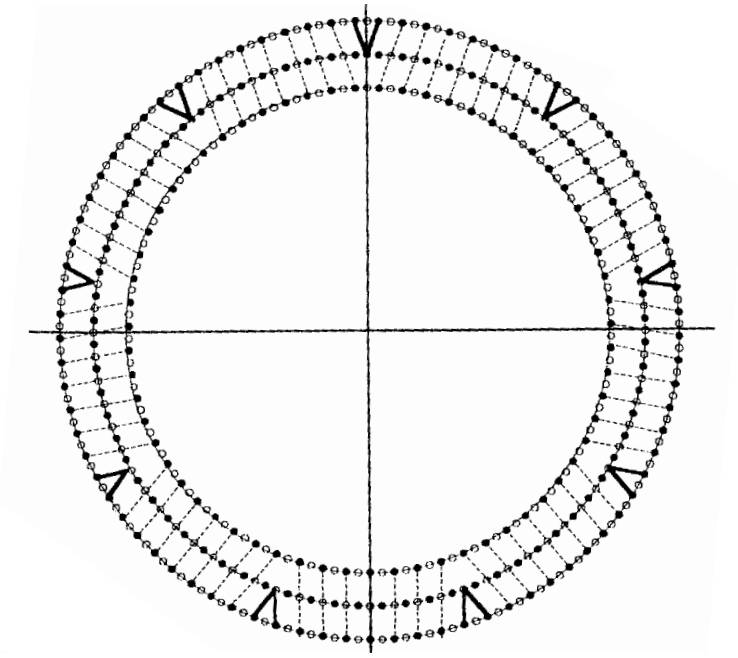

Figure 1.7: Three-layered nanotube showing how the extra rows of hexagons can be introduced to accommodate strains on the tubes. Full circles represent atoms in the plane of the paper and open circles out of the plane of the paper [1.11]

1.3 Properties of Carbon Nanotubes

The small diameter (nanoscale) and long length (microscale) of CNTs lead to such large aspect ratios that they can be considered as ideal one-dimensional (1D) systems [1.8]. This attribute of CNTs expose them to quantum effects, which, combined with their unique symmetries, has led to their unique electronic, optical, magnetic and mechanical properties. These unique properties have resulted in CNTs being identified as possible components in various applications, including nano-electronics devices, tips for scanning probe microscopes, power applications and field emitters, amongst others.

1.3.1 Electronic Properties

Dresselhaus *et al*. [1.8 – 1.10, 1.13] as well as Hamada *et al*. [1.14] have done numerous work on the electronic properties of carbon nanotubes. They have independently shown that all armchair CNTs are metallic by determining a set of allowed values for the tube's wavevector $\vec{k}$, in the circumferential direction. These values were then used to determine the electronic energy dispersion relations for the CNT. The resulting band structures show that the valence and conduction bands touched at a position 2/3 of the distance from k = 0 to the Brillioun zone boundary k = π/a, as shown in Figure 1.8 (a).

Furthermore, they've shown that for a (9, 0) zigzag CNT the valence and conduction bands touch at k = 0, as can be observed in Figure 1.8 (b), making them metallic as well. However, this is not the case for all (n, 0) zigzag tubes and only occurs if n is divisible by three. This is illustrated in Figure 1.8 (c) where there is a clear gap between the bands at k = 0 for a (10, 0) CNT, meaning that the tube is a semiconductor.

Chiral nanotubes have also been demonstrated to be either metallic or semi-conducting depending on its chiral angle and tube diameter. Dresselhaus *et al*. [1.8] have shown that metallic conduction occurs when

$$n - m = 3q \tag{1.6}$$

where n and m were defined in Figure 1.4 and q is an integer. Equation (1.6) implies that one-third of all chiral CNTs are metallic and two-thirds semiconducting.

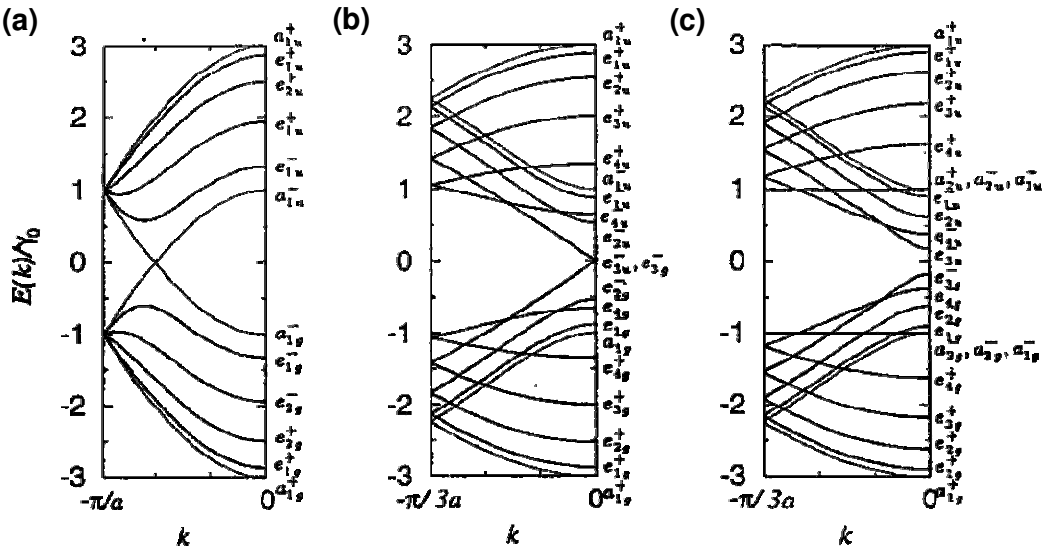

Figure 1.8: Dispersion relations for (a) armchair (5, 5) CNT, (b) zigzag (9, 0) CNT and (c) zigzag (10, 0) CNT [1.8]

Studies on the electronic properties of MWCNTs by Saito *et al*. [1.15] as well as a Belgian group [1.16, 1.17] have shown that the interlayer interaction had little effect on the electronic properties of the individual tubes. This implies, for example, if two individual metallic CNTs formed a coaxial tube, then the resulting double-walled CNT would also be metallic.

De Heer *et al*. [1.18] have shown that due to its unique electronic properties carbon nanotube films produce large emission currents at relatively low applied electric fields and compared it to that of diamond films. Two important features of merit when dealing with field emitting surfaces are the turn-on field, E_{on}, defined as the electric field required to produce a current of 10 μA/cm^2 and the threshold field E_{th}, i.e. the field required to produce a current of 10 mA/cm^2. For undoped diamond films values of E_{on} = 50 V/μm and E_{th} = 80 V/μm were reported. Typical values obtained by the De Heer research group for the CNT films showed a turn-on field of ~ 4 V/μm and threshold field of ~ 6.5 V/μm. Various groups, apart from De Heer *et al*., have demonstrated that the electronic properties of CNTs can be utilized in field-emitting devices (FEDs). For example, Uh *et al*. [1.19] have employed CNTs as the electron-emitting

source in a triode-type FED, subsequently showing that CNTs hold great promise to industrial FEDs, e.g. flat panel displays.

1.3.2 Optical Properties

A typical optical absorption spectrum for a specific CNT is a consequence of the electronic density of states (DOS) of the CNT. As an example, Figure 1.9 shows an absorption spectrum in the range from ultraviolet (UV) to infrared (IR) for a film of purified SWCNTs as measured by Minami *et al*. [1.20]. The peaks labelled S1 and S2 at 0.68 eV and 1.2 eV respectively, are due to absorption by the semiconducting nanotubes in the film, whereas the peak, M1, around 1.8 eV is because of metallic absorption in the film. Popov [1.21] reported similar results to that of Minami *et al*.

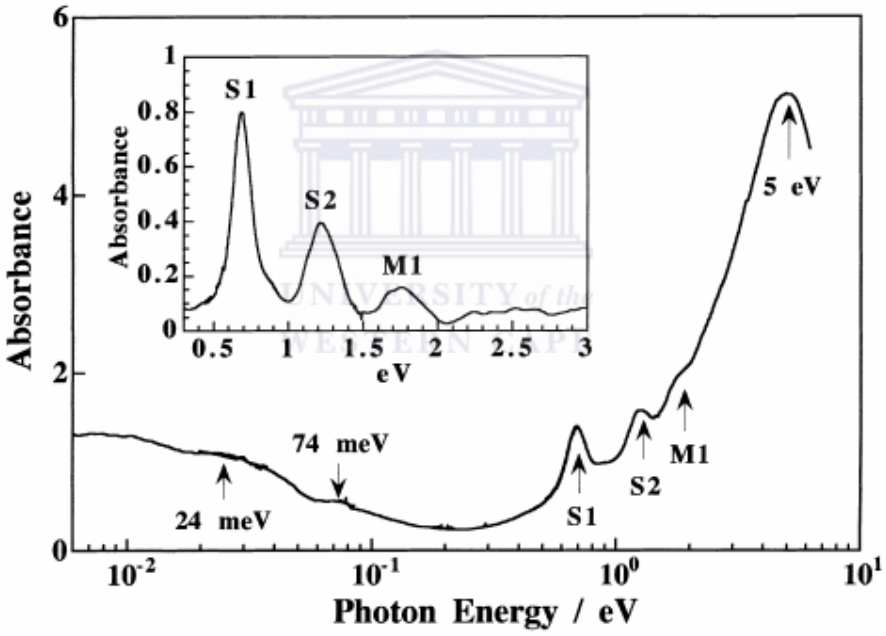

Figure 1.9: Optical absorption spectrum of a SWCNT film in air at atmospheric pressure in a wide energy range from UV to far IR [1.20]

Zhao *et al*. [1.22] reviewed the research currently focusing on the optical properties of CNTs and showed that the SWCNT film used in Figure 1.9 can be doped or wrapped with polymers to enhance the film's non-linear optical

behaviour, which is an important factor for the manufacturing of optical switches. Furthermore, Zhao *et al* also reported on the photoconductivity of CNTs, a direct characteristic of the optical properties. It was found that CNTs exhibit enhanced levels of photocurrents, which could lead to highly efficient solar cells and other optoelectronic devices.

1.3.3 Magnetic Properties

The plot in Figure 1.10 shows the relationship between induced magnetic flux density, **B** and a magnetizing force, **H** of a material. A number of magnetic properties of the material can be determined by such a plot (hysteresis loop) and include its magnetic saturation, retentivity, residual magnetism, coercivity as well as the permeability and reluctance of the material.

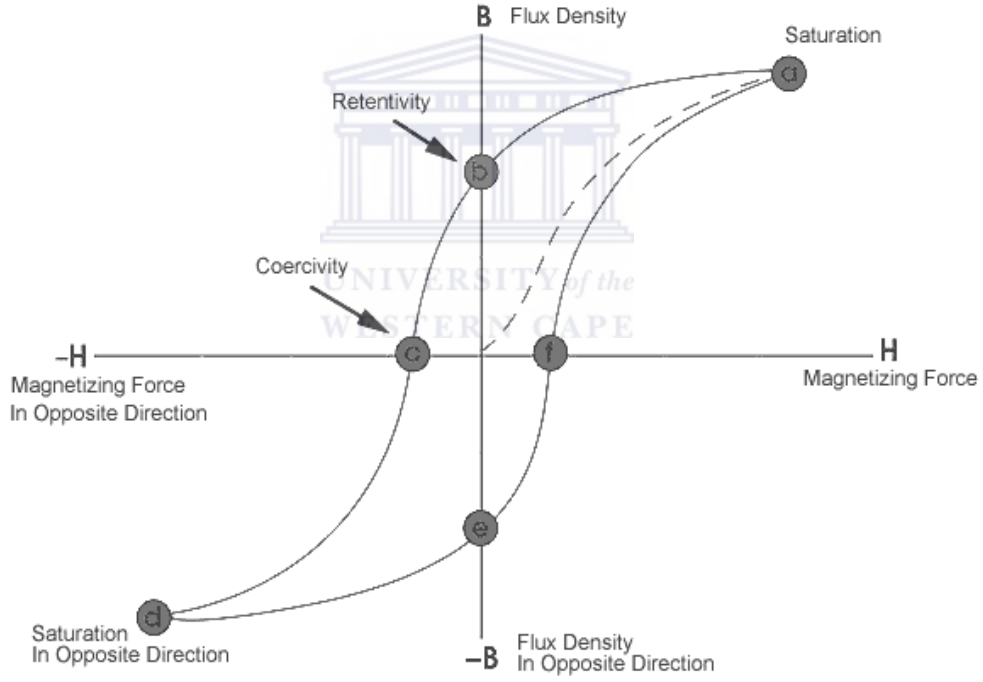

Figure 1.10: Hysteresis loop for a paramagnetic material

Ellis *et al*. [1.23] investigated the magnetic properties of a film of carbon nanotubes before and after ridding the sample of the transition metal catalyst. It was shown that the metal particles induced paramagnetic behaviour in the

nanotubes, which remained even after removal of the transition metal. Ghao *et al*. [1.24] performed a similar study to that of Ellis *et al*. However, they went a step further by attaching the magnetic nanotubes onto the red blood cells of sheep in a phosphate solution, to form magnetic cells. These blood cells can then be manipulated with a magnetic field. With these results Ghao and his group showed that the magnetic properties of CNTs can be made great use of in the biomedical and other medical fields.

1.3.4 Mechanical Properties

Consider a MWCNT with inner diameter of 1 nm, wall thickness of 0.34 nm resulting in an outer diameter of 1.68 nm. Thus the cross-sectional area of the tube will be $2.2 \times 10^{-19}\ m^2$. Following from the formulas

$$\text{tensile stress} = \frac{\text{tensile load}}{\text{area}} \tag{1.7}$$

and

$$Y = \frac{\text{stress}}{\text{strain}} \tag{1.8}$$

where Y = Young's modulus, if a tensile load of 100 nN is applied to the tube and assuming a Young's modulus equal to that of graphite (1060 GPa), it would result in a stress of ~ 45 GPa and a tensile strain of about 4.2 %. Comparing a tube with inner and outer diameter of 10 and 10.68 nm, respectively, resulting in a stress of roughly 1.1 GPa and a strain of 0.1 %, demonstrates the way in which the tube stiffness increases with increasing diameter. These results are in agreement with experimental observations that single-wall carbon nanotubes (with typical diameters of 1 nm) appear to be curly, whereas multi-wall carbon nanotubes tend to be straight.

Various groups have attempted to determine the Young's modulus for carbon nanotubes, each resulting in a different approximation, stemming from the difficulties in defining the wall thickness. Treacy *et al*. [1.25] suggested that, based upon the work done by the Tomanek group [1.26] the tensile modulus for

carbon nanotubes is in the range 1500 – 5000 GPa. Calculations by Lu [1.27] showed a Young's modulus of 970 GPa, which was found to be independent of the tube structure or diameter, however, similar calculations by Rubio *et al*. [1.28] showed an elasticity modulus of 1240 GPa which depended on the diameter and structure of the tubes. Thus there is no accepted value for the Young's modulus of carbon nanotubes, but it is agreed upon that CNTs have a Young's modulus > 1000 GPa and a yield strength in the region of 150 GPa [1.29]. Table 1 compares the mechanical properties, e.g. Young's modulus, tensile strength and density of CNTs to that of other well-known materials. These extraordinary properties of nanotubes have led to their identification as the ultimate fibre for the strengthening of materials.

Table 1.1: Mechanical properties of CNTs compared to those of other well-known materials [1.29]

Material	Young's Modulus (GPa)	Tensile Strength (GPa)	Density (g/cm^3)
SWCNT	~1054	~150	
MWCNT	~1200	~150	2.6
Steel	208	0.4	7.8
Epoxy	3.5	0.005	1.25
Wood	16	0.008	0.6

1.4 Synthesis of Carbon Nanotubes

Both SWCNTs and MWCNTs can be grown by several synthesis techniques. The three main techniques employed by scientists for the synthesis of CNTs are the arc-discharge, laser ablation and chemical vapour deposition (CVD) techniques. The CVD techniques include thermal (TCVD), hot-wire (HWCVD), plasma-enhanced (PECVD), microwave (MCVD), laser assisted (LACVD) and alcohol catalytic chemical vapour deposition (ACCVD). However, out of all these techniques, HWCVD seem to hold the most promise as an industrially applied technique as a result of it controllable and repeatable nature.

1.4.1 Arc-Discharge Technique

Two graphite rods (an anode and a cathode) are placed end-to-end, 1 mm apart in an enclosure filled with an inert gas (usually helium or argon), at pressures between 50 and 700 mbar [1.5]; recent studies have also shown that a liquid nitrogen environment can be employed. A voltage of approximately 20 V drives a direct current between 50 and 100 A, creating a high temperature discharge between the graphite rods. The discharge vaporises the anode, creating a small deposit on the cathode. This deposit consists out of carbon nanotubes as well as other carbonaceous material.

Figure 1.11 illustrates a typical experimental setup for the arc-discharge technique. This technique usually produces CNTs of high structural quality. However, the low yields of CNTs as well as the high voltages and synthesis temperatures make this technique inappropriate as an industrial technique for the mass production of CNTs.

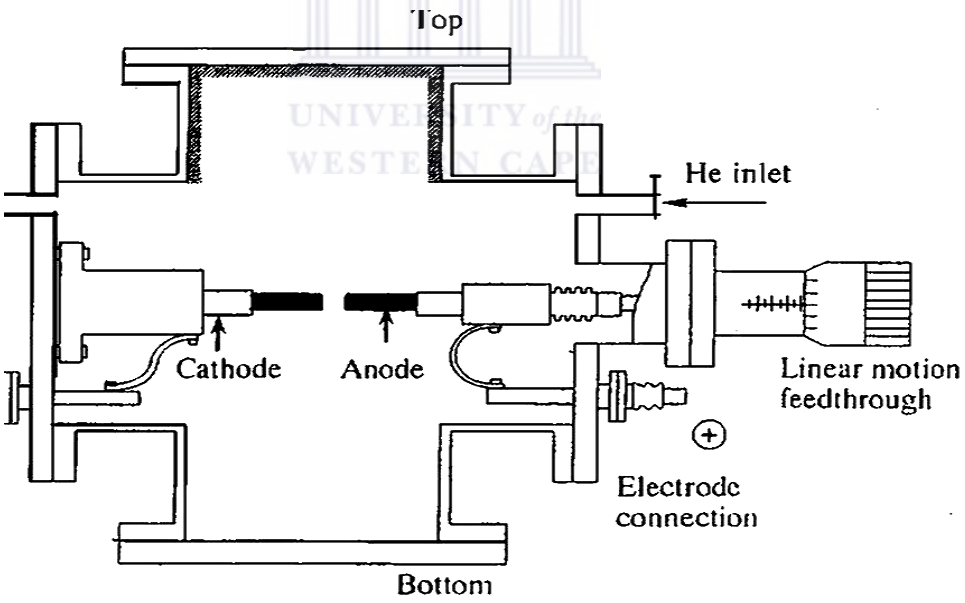

Figure 1.11: Experimental set-up for an arc-discharge apparatus [1.5]

1.4.2 Laser Vaporisation Method

Smalley *et al*. [1.30] first reported the synthesis of CNTs via laser vaporisation in 1995. A graphite target is placed in a furnace set at about 1200 ˚C. The furnace is then filled with inert gas. A high-energy laser is used to vaporise the target, as shown in Figure 1.12. The inert gas acts as carriers and also keeps the system pressure at about 500 Torr. The interaction of the laser with the graphite target creates very hot vapours which firstly expands and then rapidly cools down, where after it is collected on a cooled target, as shown in the schematic.

Upon cooling of the vaporised species, small carbon atoms and molecules condense to form large clusters. During this time the catalyst also begins to condense, but at a slower rate, and attaches itself to the carbon clusters, preventing them from forming cage structures, or it can open cage structures upon attachment, resulting in tubular molecules, which eventually grow into CNTs [1.6]. As is the case with arc-discharge, the laser ablation technique also makes use of very high deposition temperatures. Furthermore, if one considers the expenses involved in maintaining a laser, it can be seen that this technique would not be a candidate for industrial use.

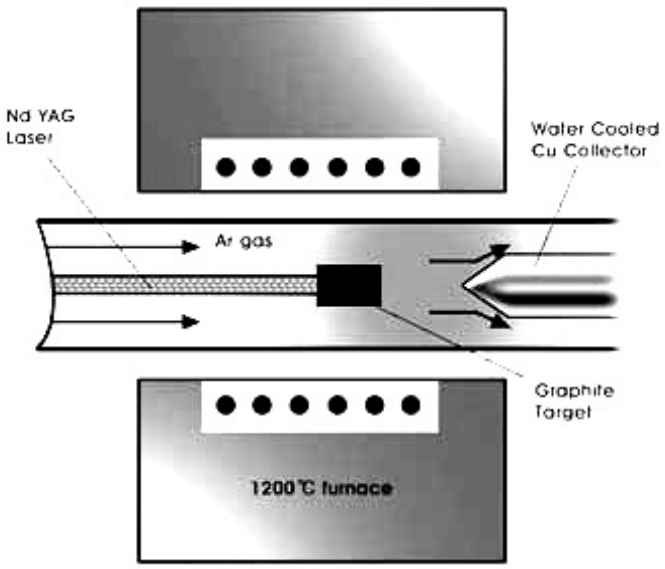

Figure 1.12: Experimental set-up for a laser vaporisation apparatus [1.6]

1.4.3 Chemical Vapour Deposition

Chemical vapour deposition (CVD) involves transforming a carbon source into a gaseous state and using an energy source such as plasma or a resistively heated coil to transfer energy to the gaseous carbon molecules, eventually decomposing it into carbon radicals. These radicals then diffuse, with the aid of an inert gas, toward a heat-treated substrate coated with a transition metal catalyst (e.g. Ni) where it will bind to form CNTs, provided the ideal deposition parameters are maintained. Sputtering or CVD is used to deposit the catalyst onto the substrate, after which it is annealed or chemically etched to induce catalyst particle nucleation (nano-islands), which acts as the source of nanotube growth. However, an alternative to a deposited film of catalyst is to employ the catalyst in the gas phase during the deposition, as was done by Dillon *et al*. [1.31].

CVD has been identified to hold more promise (than arc-discharge and laser vaporisation) as an up-scale technique for the mass production of CNTs. This is attributed to its simplicity, low cost and synthesis temperatures, as well as the high yield of CNTs attainable. However, difficulties in the control of deposition conditions as well as the high concentration of impurities in the resulting soot of the TCVD have made this technique not very suitable for practical applications. Furthermore the use of lasers, high voltages and high furnace temperatures during LACVD, PECVD and MCVD has made these techniques expensive to operate and would not seem very practical at an industrial level. Other CVD set-ups including alcohol catalytic CVD, have also been reported, but these methods have not yet been fully studied and therefore can't be considered for mass CNT production.

Dillon *et al*. [1.31] have reported CNT synthesis temperatures of 600 ºC for HWCVD, which is very attractive since the other synthesis techniques usually produce CNTs at temperatures of 700 ºC and greater. In a follow up study they have recognised the resulting MWCNTs produced by their HWCVD system as suitable candidates for hydrogen storage, which could be used for developing a vehicular hydrogen storage system and holds great promise as a renewable

energy storage device [1.32]. Furthermore, it was also reported that the MWCNT arrays grown on nickel films by the mentioned HWCVD system could replace the gold black coatings currently used in pyro-electric detectors to accurately measure laser power [1.31].

Iaia *et al*. [1.33] have recently reported the production of highly crystalline and pure SWCNTs via HWCVD, which is a remarkable achievement since the laser-vaporisation and arc-discharge techniques were previously thought to be the only methods for producing pure CNTs. Therefore, based on the above findings it can be seen that the HWCVD technique holds the most promise as an up-scalable technique for the mass production of CNTs.

1.5 Growth Mechanism of Carbon Nanotubes

Two specific growth mechanisms have been suggested and accepted by scientists for CNTs produced via catalytic decomposition (i.e. CVD prepared CNTs). These two mechanisms are base (extrusion or root) growth and tip growth, schematically illustrated in Figure 1.13. However, to date there is no accepted growth mechanism for CNTs produced via laser vaporisation and arc-discharge.

During root growth there is an initial formation of a C_2 molecule from the C_nH_m gas molecule, on the surface of the metal particle. Subsequently, more C_2 attaches to the advancing metal particle, whose vertex (tip) remains 'clean'. The attaching C_2 molecules attach to each other to form graphitic structures, and eventually CNTs. The other growth mechanism suggested, stems from the high solubility of carbon at high temperatures in transition metals and is referred to as tip-growth, also shown in Figure 1.13. Instead of the formation of a C_2 molecule on the surface, the carbon molecules diffuse through the metal particle, after which filament growth occurs and again the advancing 'face' of the particle remains clean during the filament formation [1.5, 1.6].

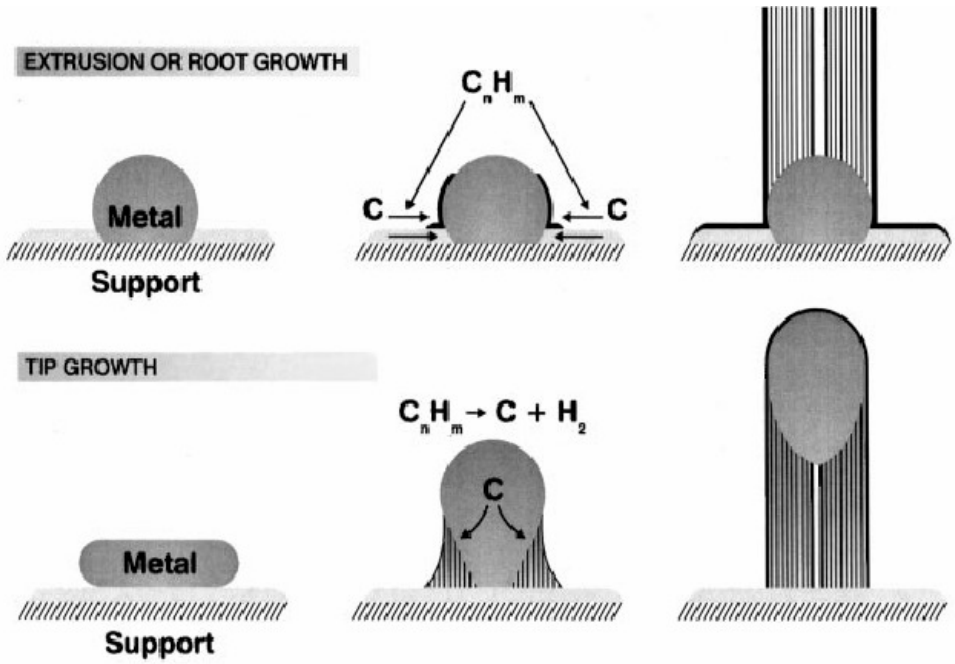

Figure 1.13: Growth mechanisms of CNTs synthesised by CVD [1.6]

1.6 Aims and Outline

Presently researchers worldwide are unable to predict the growth of CNTs produced via laser ablation and arc-discharge. Furthermore, the growth of CNTs synthesised via CVD is also not fully understood. This stems from the inability to accurately control the deposition parameters for the growth of CNTs. Due to its repeatable and controllable nature, HWCVD has shown most promise in resolving this predicament. In addition, due to its gas phase nature, it has also been identified as an industrially applied technique for the mass production of CNTs. The aim of this study will be to construct a HWCVD system and optimize it for the synthesis of CNTs of high structural perfection and micro-sized lengths. This will be achieved by studying the effect of the following deposition parameters on the resulting CNT morphology and structure:

- Furnace temperature, T_{fur}
- Deposition pressure, P_{dep}
- Substrate-to-filament distance, $d_{s\text{-}f}$, as well as the
- Methane/Hydrogen dilution, f_{CH4}, defined as:

$$f_{CH4} = \frac{\Phi_{CH4}}{\Phi_{CH4} + \Phi_{H2}} \quad (1.9)$$

where Φ_{CH4} and Φ_{CH4} are the methane and hydrogen gas flow rates, respectively.

The outline of this thesis is as follows:

In Chapter One a general background to CNTs was given. The chapter highlighted the current state of CNT research around the world. Topics such as the discovery of CNTs, the different CNT structures, as well as the CNT properties, synthesis and growth mechanisms were discussed.

Chapter Two will provide a description of the hot-wire chemical vapour deposition set-up and its operation. Moreover, the geometry of the system will be described including its operating filament and gas supply system. Calibration of the filament temperature against the filament current will be presented along with analysis of the results observed in the calibration curves. Concluding this chapter will be a detailed description of the procedure needed to successfully deposit CNTs with the above set-up.

Chapter Three will discuss all the analysis techniques that will be used in this study to investigate the CNT morphology and structure. Detailed theoretical background, upon which each technique is based, will be given. Furthermore, each technique will also have a 'Characterisation' section, in which the information that has been gathered from the technique regarding CNTs is explained in detail.

Chapter Four will report on the effect of the deposition parameters on the morphology of the carbon nanotubes deposited via the HWCVD technique, whereas Chapter Five investigates the effect of the deposition parameters on the structural properties of the carbon nanotubes.

A final chapter will summarize the findings of Chapters Four and Five and provide details on possible future studies.

References

[1.1] H. W. Kroto, J. R. Heath, S. C. O'Brien, R. F. Curl and R. E. Smalley, Nature, **318** (1985) 162

[1.2] A. Kratschmer, L. D. Lamb, K. Fostiropoulos, D. R. Huffman, Nature, **347** (1990) 354

[1.3] P. M. Ajayan, T. W. Ebbesen, Reports on Progress in Physics, **60** (2003) 1025

[1.4] S. Iijima, Nature, **354** (1991) 56

[1.5] P. J. F. Harris, '*Carbon Nanotubes and Related Structures: New Material for the 21st Century* ', Cambridge University Press, Cambridge, (1999)

[1.6] M. A. J. Veld, M. Daenen, R. D. De Fouw, B. Hamers, P. G. A. Janssen and R. Schouteden, '*The Wondrous World of Carbon Nanotubes: A Review of Current Carbon Nanotubes Technologies*', Eindhoven University of Technology, Eindhoven, (2003)

[1.7] T. Belin and F. Epron, Materials Science and Engineering B, **119** (2005) 105

[1.8] M. S. Dresselhaus, G. Dresselhaus and P. C. Eklund, '*Science of fullerenes and carbon nanotubes*', Academic Press, San Diego, (1996)

[1.9] M.S. Dresselhaus, G. Dresselhaus and R. Saito, Carbon, **33** (1995) 883

[1.10] R. A. Jishi, M. S. Dresselhaus and G. Dresselhaus, Physics Review B, **47** (1993) 671

[1.11] X. F. Zhang, X. B. Zhang, G. Van Tendeloo, S. Amelinckx, M. Op de Beeck and J. Van Landuyt, Journal of Crystal Growth, **130** (1993) 368

[1.12] D. Reznik, C. H. Olk, D. A. Neumann and J. R. D. Copley, Physics Review B, **52** (1995) 116

[1.13] R. Saito, M. Fujita, G. Dresselhaus and M. S. Dresselhaus, Physics Review B, **46** (1992) 1804

[1.14] N. Hamada, S. Sawada and A. Oshiyama, Physics Review Letters, **68** (1992) 1579

[1.15] R. Saito, G. Dresselhaus and M. S. Dresselhaus, Journal of Applied Physics, **73** (1993) 494

[1.16] J.-C. Charlier and J.-P. Michenaud, Physics Review Letters, **70** (1993) 1858

[1.17] P. Lambin. L. Phillippe, J.-C. Charlier and J.-P. Michenaud, Computational Materials Science, **2** (1994) 350

[1.18] W. A. de Heer, J.-M. Bonard, T. Stockli, A. Chatelain, L. Forro and D. Ugarte, Zeitschrift Fur Physik D, **40** (1997) 418

[1.19] H. S. Uh and S. S. Park, Thin Solid Films, **504** (2006) 50

[1.20] N. Minami, S. Kazaoui, R. Jacquemin, H. Yamawaki, K. Aoki, H.Kataura and Y. Achiba, Synthetic Metals, **116** (2001) 405

[1.21] H. Kataura, Y. Kumazawa, Y. Maniwa, I. Umezu, S. Suzuki, Y. Ohtsuka, Y. Achiba, Synthetic Metals, **103** (1999) 2555

[1.22] J. Zhao, X. Chen and J. R. H. Xie, Analytica Chimica Acta, **568** (2006) 161

[1.23] A. V. Ellis and B. Ingram, Journal of Magnetism and Magnetic Materials, **302** (2006) 378

[1.24] C. Ghao, W. Li, H. Morimoto, Y. Nagaoka and T. Maekawa, Journal of Physical Chemistry B, **110** (2006) 7213

[1.25] M. M. J. Treacy, T. W. Ebbesen and J. M Gibson, Nature, **381** (1996) 678

[1.26] G. Overney, W. Zhong and D. Tomanek, Zeitschrift fur Physik D, **27** (1993) 93

[1.27] J. P. Lu, Physics Review Letters, **79** (1997) 1297

[1.28] E. Hernandez, C. Goze, P. Bernier and A. Rubio, Physics Review Letters, **80** (1998) 4502

[1.29] M.-F. Yu, B. S. Files, S. Arepalli and R. S. Ruoff, Physics Review Letters, **84** (2000) 5552

[1.30] T. Guo, P. Nikolaev, A. G. Rinzler, D. Tomanek, D. T. Colbert and R. E. Smalley, Journal of Physical Chemistry, **99** (1995) 694

[1.31] A. C. Dillon, A. H. Mahan, R. Deshpande, J. L. Alleman, J. L. Blackburn, P. A. Parillia, M. J. Heben, C. Engtrakul, K. E. H. Gilbert, K. M. Jones, R. To, S.-H. Lee and J. H. Lehman, Thin Solid Films, **501** (2006) 216

[1.32] R. Deshpande, A. C. Dillon, A. H. Mahan, J. Alleman, S. Mitra, Thin Solid Films, **501** (2006) 224

[1.33] A. Iaia, L. Marty, C. Naud, V. Bouchiat, A. Loiseau, E. Di Muoio, T. Fournier, A. M. Bonnot, Thin Solid Films, **501** (2006) 221

CHAPTER TWO

Hot-Wire Chemical Vapour Deposition

2.1 Introduction

Since its introduction in 1979 [2.1], hot-wire chemical vapour deposition (HWCVD) has been mainly used for the deposition of various allotropes of silicon and silicon alloys. However, the technique's versatility has resulted in its employment for the synthesis of carbon structures such as graphite, diamond, polymers, amorphous carbon and carbon nanotubes (CNTs). Dillon *et al*. [2.2] have recently shown that the HWCVD technique can be used to deposit CNTs at low temperatures as compared to other CVD techniques, e.g. thermal CVD. Furthermore, it has also been shown that, compared to the other CVD techniques, HWCVD allows for controlled growth of CNTs with small diameters and high crystallinity [2.3].

During the HWCVD process a precursor gas, usually diluted in hydrogen gas decomposes over a heated filament into reactive radicals and atomic hydrogen. The atomic hydrogen has been shown to act as an etching agent promoting the growth of the structures (species) needed to grow the desired material. The material then grows on a heated substrate that acts as a support. Due to the nature of the process, various parameters will play a role in the growth of the desired material, including the gas mixture pressure and ratio, the system geometry, the temperature of the substrate as well as the properties of the filament, i.e. its temperature, filament-to-substrate distance and the type of filament material [2.4].

In this chapter the design of a HWCVD system used for the deposition of CNTs will be described, including its gas supply system. Furthermore, the chapter will also look at the tungsten filament-current calibration in different gas ambients,

as well as an investigation into the variation in the results of the calibration curves. The chapter concludes by describing the procedure that was followed for the deposition of CNTs.

2.2 The Hot-Wire Chemical Vapour Deposition System

The hot-wire chemical vapour deposition (HWCVD) system under investigation was designed and built at the Council for Scientific and Industrial Research (CSIR) and is an ultra-compact, versatile and experimental system for the deposition of carbon nanotubes, other nano-materials as well as thin film semiconducting material.

The system consists of a 62 cm long quartz tube with an inner and outer diameter of 26 and 30 mm, respectively. The tube is enclosed by a 28 cm long cylindrical furnace, which serves to heat the substrate and is capable of reaching temperatures in excess of 1000 °C, as measured by a K-type thermocouple. This system is capable of reaching base pressures of 10^{-3} Torr when pumped down with an Edwards E2M8 rotary vane pump. A RIBER® regulating valve connected at one end of the tube controls the deposition pressure, whereas an air-inlet valve (also connected at this end of the tube) allows air into the reactor, in order to break vacuum. Two pressure gauges, G1 and G2, are used to measure the base and deposition pressure, respectively. G1 is a RIBER® penning gauge capable of measuring pressure between 10^{-3} and 10^{3} Torr and is therefore employed to measure the base pressure of the system. However, it is difficult to accurately measure the deposition pressure of around 10^{2} Torr with G1. For this reason G2, which can accurately measure pressure between 1 and 10^{3} Torr, is used to measure the deposition pressure.

An alternating current (AC) power supply with a maximum power output of 1.25 kW (giving a maximum current of 50 A) is fed to a 35 cm long coiled tungsten filament with a 0.5 mm diameter, with the aim of heating and dissociating the carbon precursor gas. One end of the filament is fixed to a an electrode

supported on a stainless steel rod with a 4 mm diameter, whilst the other end is connected to a flexible electrode that slides free in the longitudinal direction along the stainless steel rod. Electric wiring to the electrodes is enclosed by ceramic rods that extend 34 cm into the opposite end (to the RIBER® regulating valve) of the quartz tube. Also connected at this end of the tube is the gas inlet, through which the reactant and purging gases are fed to the system. In Figure 2.1 a schematic representation as well as an actual picture (without the furnace) of the system is shown.

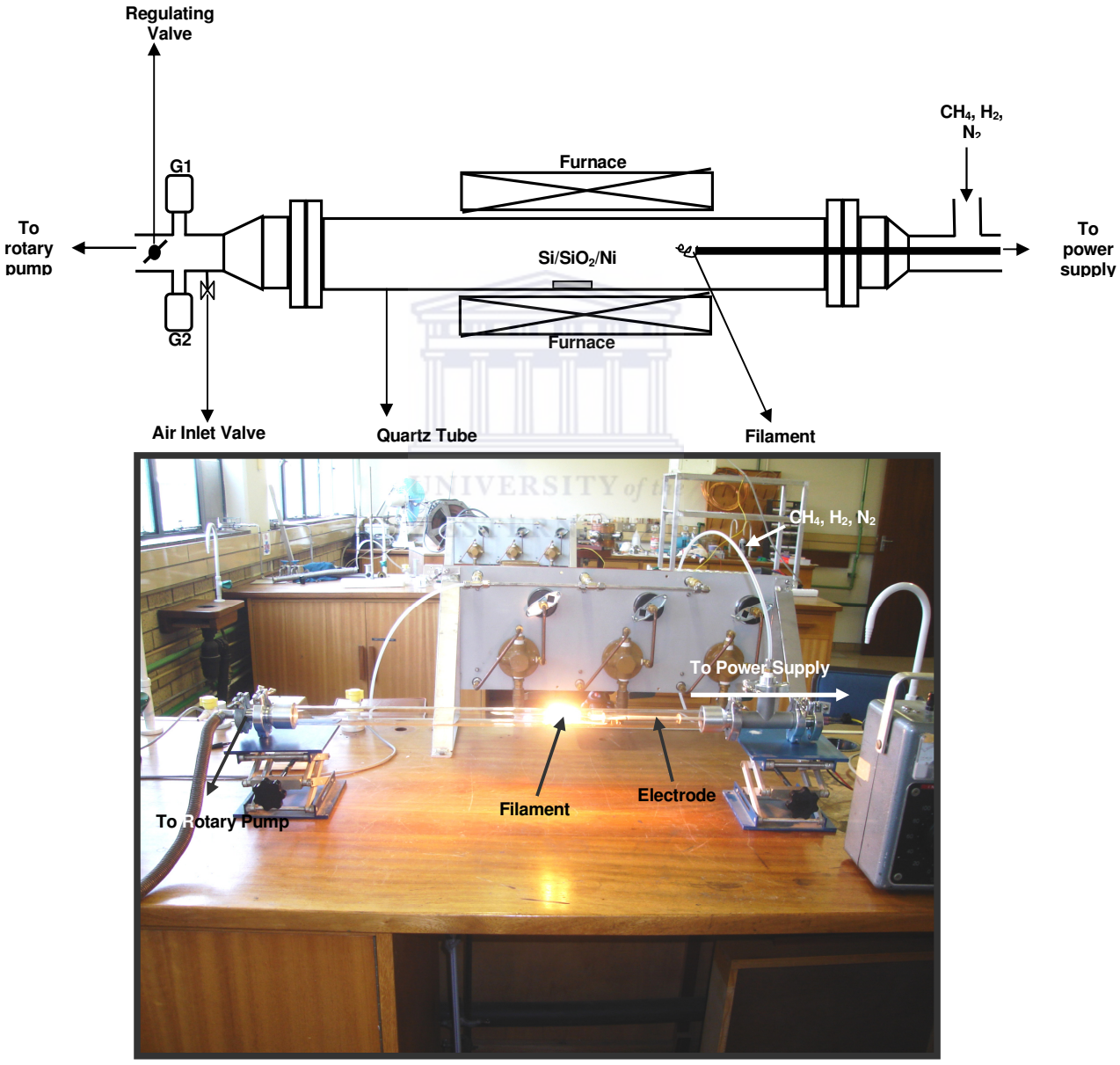

Figure 2.1: Schematic representation and the HWCVD system built at the CSIR in operation (without the furnace)

2.3 Gas Supply System

Three different gases can be supplied to the HWCVD system, namely the purging gas nitrogen (N_2) and the reaction gases, methane (CH_4) and hydrogen (H_2). These gases are supplied and monitored by a gas supply system consisting of gas lines, mass flow meters, exhaust, manual and regulating valves, as well as non-return valves.

The regulating valve connected to each gas cylinder controls the pressure at which the gas exits the cylinder into the gas line. A Hattersley® manual valve opens and closes entry of the gas towards the ABB® mass flow meters, which regulate the flow of the gas through the HWCVD system. A second regulating valve controls the pressure (gas inlet pressure) at which the gas is pumped through to the mass flow meters. Non-return valves add to the safety features of the gas supply system by preventing backward motion of the gas towards the gas lines. This backward motion will increase the pressure in the gas supply lines and can cause an explosion. The exhaust, located at an elevated position, allows the gas to exit the laboratory into safe surroundings.

For the deposition of carbon nanotubes, mixtures of methane and hydrogen gas are supplied to the HWCVD system. These mixtures are monitored by adjusting the scale readings on each of the mass flow meters. After each deposition the system is flushed with a steady flow of nitrogen gas, whose flow is also controlled by its mass flow meter scale reading. Figure 2.2 gives a schematic representation of the gas supply system, whereas Figure 2.3 shows the gas control unit, which consists of the manual valves, mass flow meters, the second set of regulating valves as well as the non-return valves.

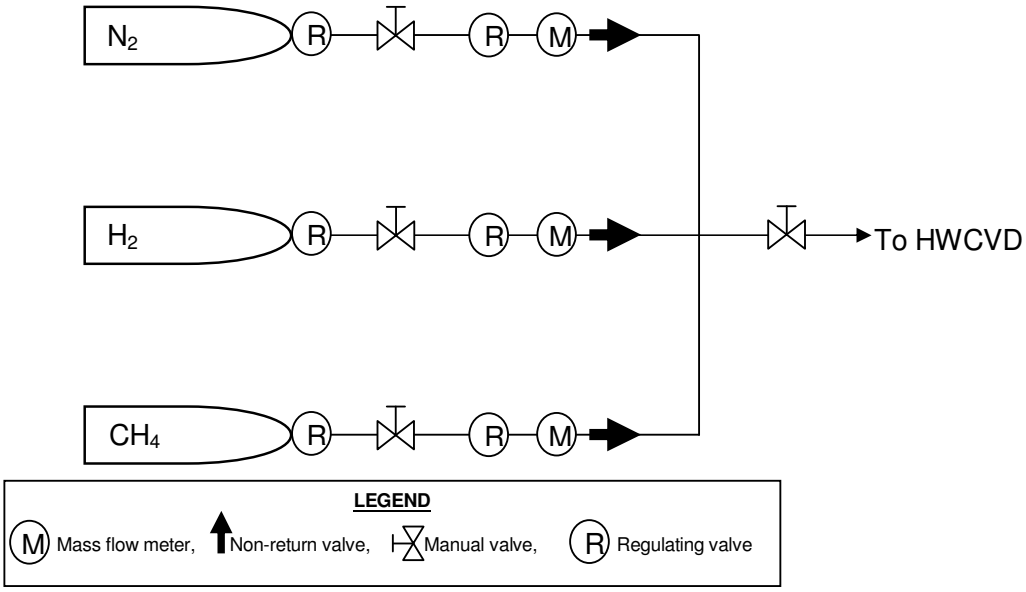

Figure 2.2: Schematic representation of the gas supply system

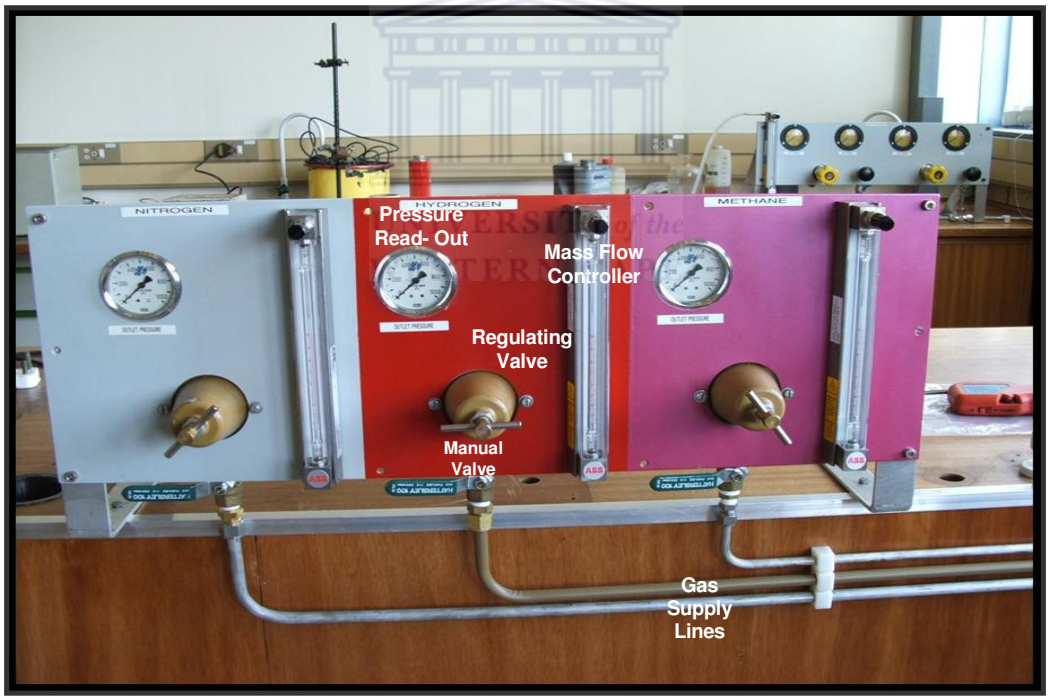

Figure 2.3: Gas control unit. Not shown is the non-return valve, which is located at the back-end of this unit.

In Figure 2.4, calibration of the gas flow rate, in cubic centimeter per minute (cm^3/min), against the mass flow meter reading is given for the three different gases at the different gas inlet pressures. The gas inlet pressure, gas density, gas temperature as well as the mass flow meter type are all factors playing a major role in the calibration of the gas flow rate against the mass flow meter scale reading.

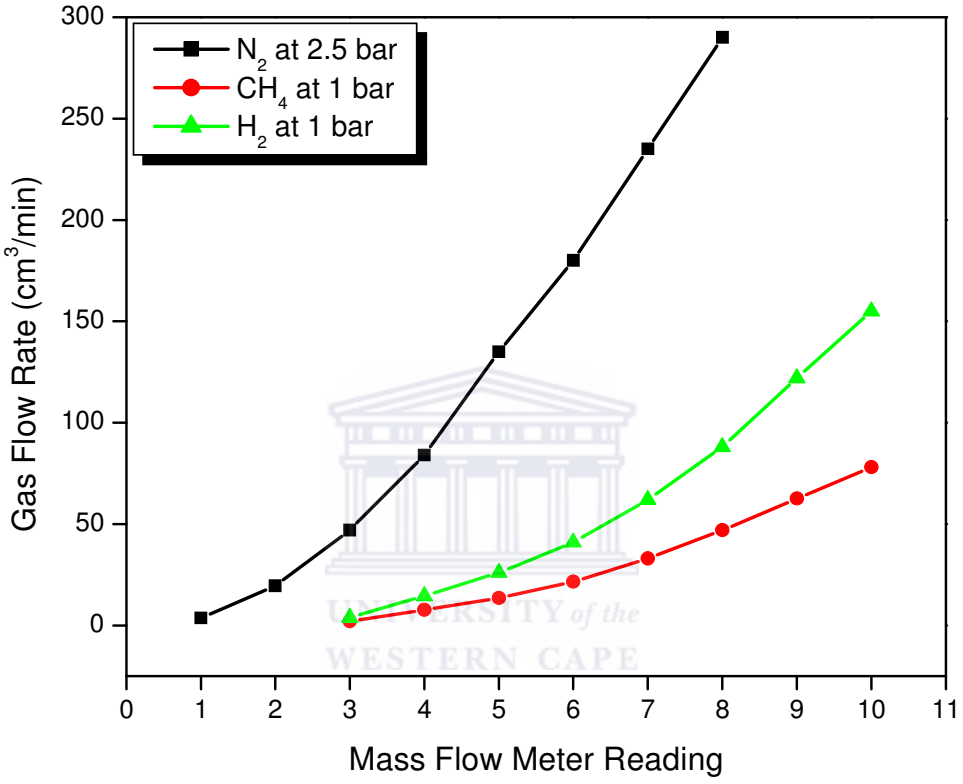

Figure 2.4: Gas calibration for CH_4, H_2 and N_2 gas

2.4 The Tungsten Filament

2.4.1 Temperature – Current Calibration

The tungsten filament plays an important role in the HWCVD process as it acts as a catalyst for the dissociation of the methane gas molecule into reactive

carbon radicals, which in turn, then act as the carbon source in the nanotube growth process. At the root of this catalytic process is the filament temperature, T_{fil} which determines the rate at which the methane molecules dissociate into radicals. In the HWCVD system described in chapter 2.2, T_{fil} is controlled by passing an alternating current through the tungsten filament. Calibration of T_{fil} against the filament current, I_{fil} was performed using a Minolta LAND TS-154 high temperature infrared pyrometer. The calibration experiments were performed in vacuum at 10^{-3} Torr, as well as in nitrogen, hydrogen and methane gas ambients at 10^{2} Torr each, as shown in Figure 2.5.

From Figure 2.5 it can be seen that T_{fil} increases linearly with I_{fil} when operated in the different atmospheres. Figure 2.5 also shows that there is no appreciable change in T_{fil} when the filament is operated in N_2 as compared to operation in vacuum. This is ascribed to the presence of residual N_2 in the reactor after the initial purging of the system; therefore when the experiments are performed in vacuum of 10^{-3} Torr, the presence of the N_2 actually results in the experiments being performed in a N_2 ambient, hence the similarity in the red and black lines in Figure 2.5.

However, when the experiments were conducted in CH_4 and H_2 ambients, a definite cooling effect is noticed by the decrease in measured filament temperature over a given current range. Furthermore, when operated in a H_2 atmosphere it can also be seen that the gradient of the calibration curve remains similar to that of the filament operated in vacuum, suggesting minimal change in the properties of the filament after operation in H_2. On the other hand, a definite change in the gradient of the calibration curve is noticed after operation of the filament in a CH_4 atmosphere, suggesting a change in the properties of the filament.

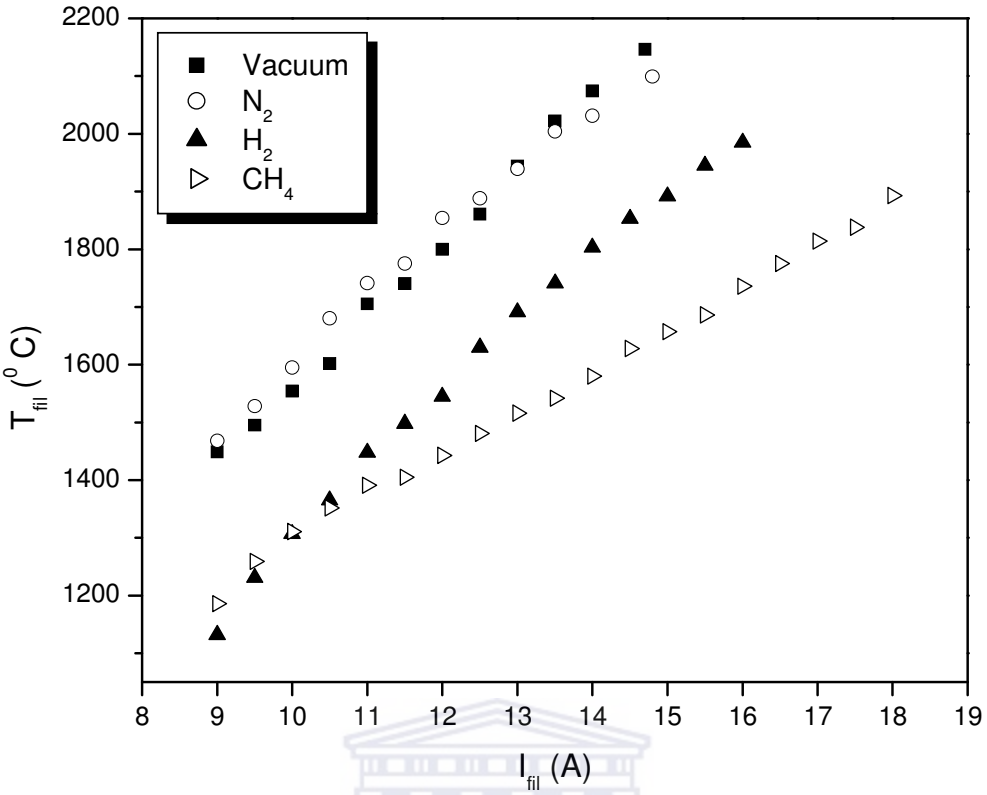

Figure 2.5: Calibration of the tungsten filament temperature against the applied current

2.4.2 Filament Analysis

Figure 2.6 compares the morphology of a tungsten filament before and after it was operated in a methane/hydrogen dilution of 0.08 for 10 minutes at a filament current of 18 A. The SEM micrograph of Figure 2.6 (b) clearly shows the formation of a layer on the filament surface after its exposure to the gas mixture.

The Energy Dispersive Spectroscopy (EDS) spectra shown in Figure 2.7 clearly show that there is an increase in the carbon and decrease in tungsten concentrations on the surface of the filament after its operation in the methane/hydrogen gas mixture. This not only indicates that the layer formed on this filament's surface contains carbon, but also that the tungsten filament

indeed dissociates the methane molecule, as predicted by literature. The EDS technique will be discussed in Chapter 3.2.7 under the heading '*Characteristic X-rays and Energy Dispersive Spectroscopy*'.

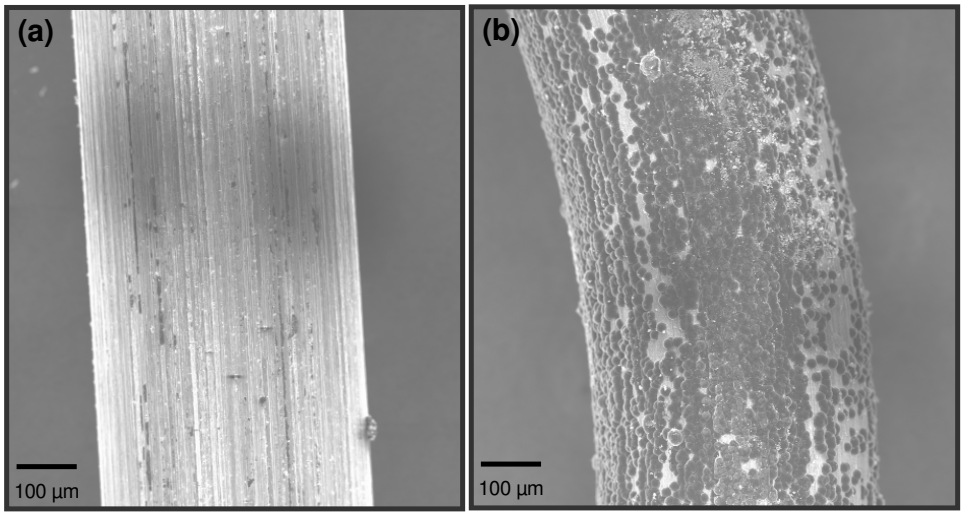

Figure 2.6: SEM micrographs of the tungsten filament (a) before CH_4/H_2 treatment and (b) after CH_4/H_2 treatment

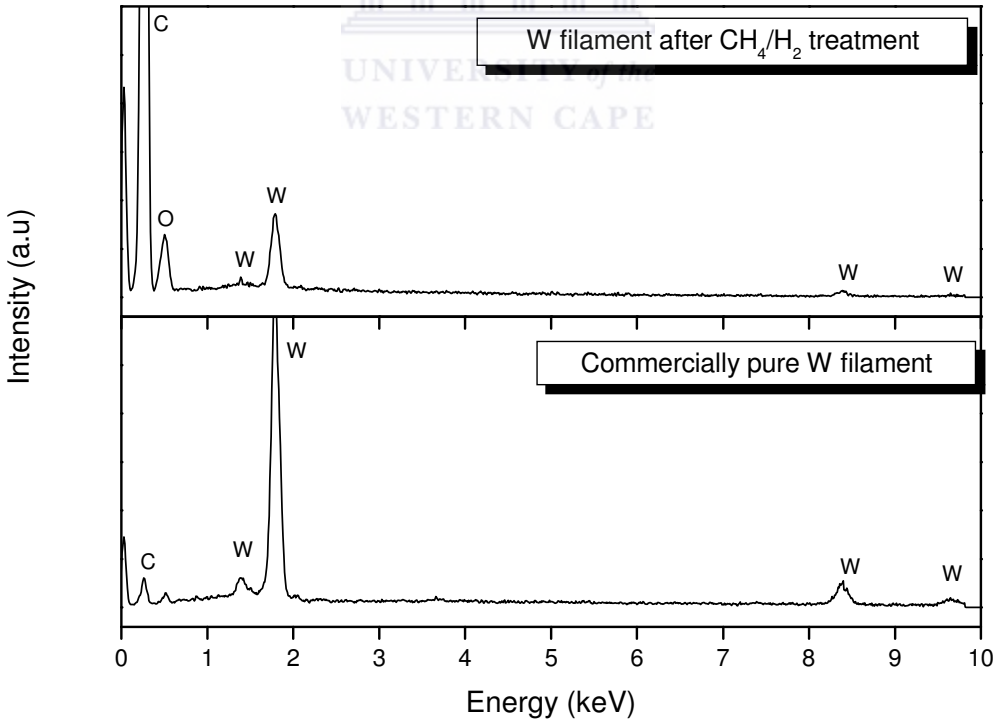

Figure 2.7: EDS analysis of the filament before and after exposure to CH_4/H_2 for 10 minutes

Figure 2.8 gives the binary phase diagram of the W-C system, as determined by Kurlov *et al*. [2.5]. According to their calculations there exists only two tungsten carbide phases, namely WC and W_2C. Only one form of the higher WC phase (also denoted by δ-WC) exists, whereas the W_2C phase has three forms, namely the low-temperature (β''), intermediate (β') and high-temperature (β), which is also designated by α-, β-, and γ-W_2C, respectively.

During deposition, the tungsten filament typically reaches operating temperatures between 1600 and 2300 ºC, thus the binary phase diagram of Figure 2.8 predicts the presence of the δ-WC phase as well as the low (β'') and intermediate temperature (β') forms of the W_2C at these temperatures.

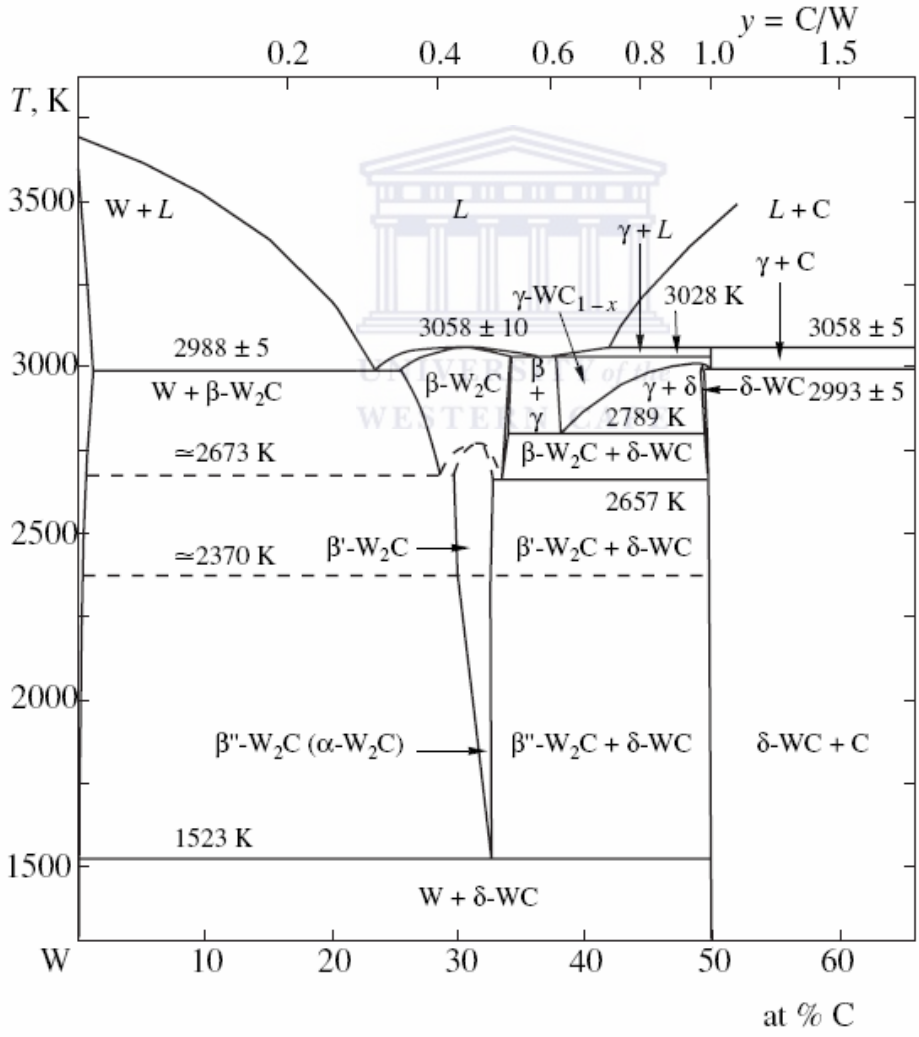

Figure 2.8: Binary phase diagram of the W-C system [2.3]

The X-Ray Diffraction (XRD) spectra, shown in Figure 2.9 compare the crystal structure of the tungsten filament shown in Figure 2.6. The diffraction peaks in Figure 2.9 were identified using the diffraction pattern database maintained by the Joint Committee for Powder Diffraction Studies (JCPDS) [2.6]. Although the JCPDS cards did not allow one to distinguish between the different forms of the W_2C phase, the results clearly show the presence of the WC and W_2C phases (as predicted by the binary phase diagram of Figure 2.9) on the surface of the tungsten filament after it was exposed to the methane/hydrogen gas mixture. The XRD technique will be discussed in Chapter 3.3 entitled '*X-ray Diffraction*'.

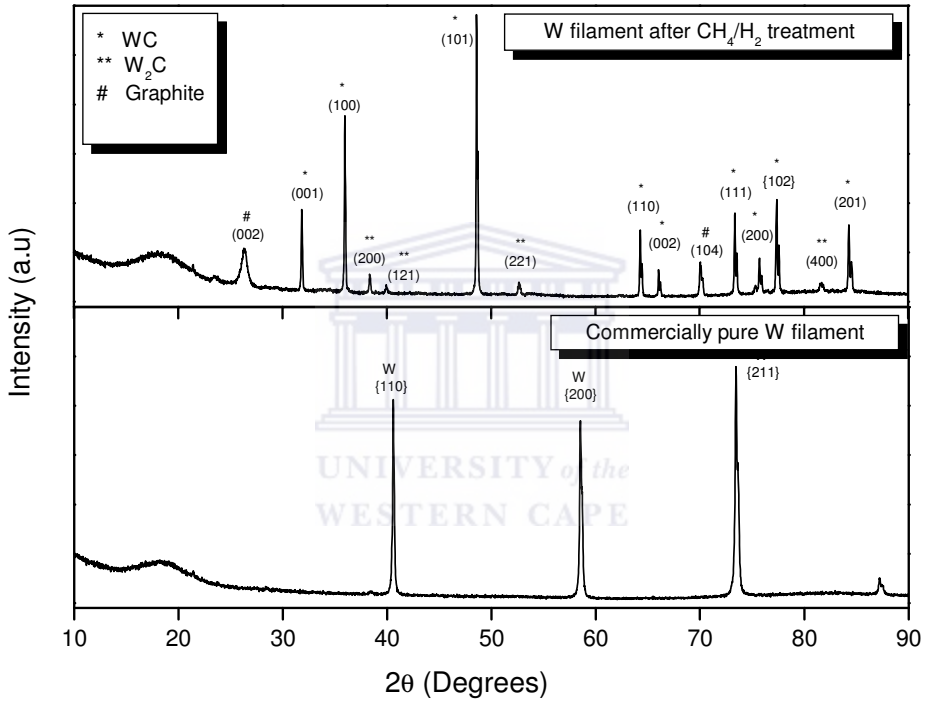

Figure 2.9: XRD spectra of the tungsten filament before and after use in a methane/hydrogen atmosphere

Kromka *et al*. [2.7] investigated the change in the tungsten filament properties after exposure to a methane/hydrogen atmosphere. They found that the formation of the tungsten carbide surface layer not only increases the wire's resistance, but it also enlarges the filament's radiative surface. Therefore, when the filament is operated in a methane/hydrogen atmosphere, an increase in power supply to the filament is required in order to achieve the same temperature as when operated in vacuum.

In conclusion, based on the XRD results of Figure 2.9 and the study performed by Kromka *et al*., the drop in filament temperature, accompanied by the change in the gradient of the calibration curve observed in Figure 2.5 can thus be attributed to the formation of a tungsten carbide layer (comprising of WC and W_2C phases) on the filament surface after exposure of the filament to the methane/hydrogen gas mixture.

2.5 Experimental Procedure

2.5.1 Substrate Preparation

In this study single-side polished, mono-crystalline silicon (Si) wafers, orientated in the <100> direction were used as substrates for the deposition of CNTs. The Si wafers are coated with a 50 nm thick SiO_2 layer. Silicon was specifically used as it is found to be stable at high temperatures. The SiO_2/Si wafers were cut into 1 x 1 cm^2 squares, after which they were ultrasonically cleaned in acetone, to rid their surfaces of impurities. This was followed by washing of the SiO_2/Si squares with de-ionized water to remove all traces of acetone.

2.5.2 Nickel Deposition

Carbon nanotube growth requires the presence of a transition metal catalyst, more specifically the formation of transition metal nano-islands. Studies [2.4, 2.8, 2.9] suggests that the diameter distribution of the CNTs largely depend on the size and shape of these nano-islands, therefore it is deemed very important to treat and have control over the transition metal nano-islands. Various techniques can be employed to form these nano-islands, including sol-gel, metalorganic chemical vapor deposition (MOCVD) and physical deposition (i.e. sputtering or evaporation) [2.8].

In this study, nickel (Ni) was used as the transition metal catalyst for CNT growth. A 10 nm thick thin film of Ni was resistively evaporated onto the Si/SiO_2 substrates. This thickness has been shown to be adequate for the formation of the nano-islands, whilst the SiO_2 layer has been shown to act as a diffusion barrier, preventing Si_xNi_y phase formation between the Si substrate and the Ni layer during the nanotube growth process. The formation of these phases can prevent nano-island formation, which in turn will prevent CNT growth [2.9].

A base pressure of 10^{-6} Torr was maintained before deposition, whereas during deposition the pressure rose to 10^{-5} Torr inside the Bell-jar vacuum system. The temperature inside the system was measured at 40 ºC during deposition and the deposition rate was recorded at 1 Å/s, as monitored by an Inficon® crystal monitor.

2.5.3 Carbon Nanotube Deposition

Before each deposition a new tungsten filament is prepared by coiling a 35 cm long piece of wire and connecting it between the two electrodes. The $Ni/SiO_2/Si$ substrate is placed inside the tube reactor system so that it is exactly in the middle of the cylindrical furnace (see Figure 2.1). The filament, along with its heating system (electrodes supported on the stainless steel rod) is then inserted in the quartz tube, after which the system is sealed and allowed to reach the desired base pressure. After attaining the base pressure, the filament is heated to remove any impurities on the filament surface, caused by handling and exposure to air.

The furnace is then set to the required temperature. The methane/hydrogen dilution ratio is controlled by opening the Hattersley® manual valves and adjusting the scale reading on each of the ABB® mass flow meters. The deposition pressure is then obtained by adjusting the RIBER® regulating valve. After achieving sTable pressure conditions, the filament is slowly heated up to its maximum current output at which the pyrolytic dissociation of methane and hydrogen starts over the surface of the filament. This is also the starting point for the deposition time, which is set for ten minutes. After ten minutes the

filament is turned off and the Hattersley® manual valves shut. The furnace is set to zero and the RIBER® regulating valve opened to remove the methane and hydrogen gases from the system. After each deposition a steady flow of nitrogen gas is let into the system, in order to further remove any traces of the methane and hydrogen gases. The HWCVD system is then allowed to cool down to about 100 ºC, where after the sample is removed.

References

[2.1] H. Wiesmann, A. K. Ghosh, T. McMahon and M. Strongin, Journal of Applied Physics, **50** (1979) 3752

[2.2] A. C. Dillon, A. H. Mahan, R. Deshpande, J. L. Alleman, J. L. Blackburn, P. A. Parillia, M. J. Heben, C. Engtrakul, K. E. H. Gilbert, K. M. Jones, R. To, S.-H. Lee and J. H. Lehman, Thin Solid Films, **501** (2006) 216

[2.3] R. Deshpande, A. C. Dillon, A. H. Mahan, J. Alleman, S. Mitra, Thin Solid Films, **501** (2006) 224

[2.4] J.-M. Bonard, Thin Solid Films, **501** (2006) 8

[2.5] A. S. Kurlov and A. I. Gusev, Inorganic Materials, **42** (2006) 21

[2.6] Joint Committee for Powder Diffraction Studies, Card No's: 89-2371, 89-2727, 89-4900, 75-1621

[2.7] A. Kromka, J. Janik, A. Satka and J. Pavlov, Acta Physica Slovaca, **51** (2001) 359

[2.8] A.-C. Dupuis, Progress in Materials Science, **50** (2005) 929

[2.9] K. H. Park, J. H. Yim, S. Lee and K. H. Koh, Thin Solid Films, **501** (2006) 233

CHAPTER THREE

Analytical Techniques

3.1 Introduction

The study of carbon nanotubes requires accurate and well-understood techniques. Table 3.1 gives an overview of the experimental techniques needed for the study of carbon nanotube morphology, structure and properties.

Table 3.1: Analytic techniques required for the study of CNTs

Technique	Information Gathered
Scanning Electron Microscopy (SEM)	Morphology
Energy Dispersive Spectroscopy (EDS)	Elemental Composition
Transmission Electron Microscopy (TEM)	Internal Structure of the CNTs
Raman Spectroscopy	Structure Identification (MWCNTs or SWCNTs) Structural Perfection (Impurity content)
X-Ray Diffraction (XRD)	Degree of Crystallinity and Structural Perfection of the CNTs

3.2 Scanning Electron Microscopy

3.2.1 Introduction

In modern times the scanning electron microscope (SEM) has been utilized in a diverse field of study, stretching from biomedical science to the semiconductor industry. The characteristic three-dimensional appearance of the images formed during SEM gives useful information of the surface morphology and topography of the sample up to the nanometer scale.

In a SEM, electrons are thermionically emitted from a cathode or a field-emitter, within an electron gun, situated at the top of its electron-optical column. The emitted electrons form an electron cloud, which is then focussed by carefully designed and placed electromagnetic lenses, coils and apertures into a fine probe that systematically scans over the specimen surface, to produce an image. The electrons are accelerated by high voltages towards a specimen-containing anode.

Two condenser lenses, situated below the electron gun focuses the emerging beam into a much smaller diameter size, which is then further aligned and focused by apertures and coils within the column until it reaches the final (or objective) lens near the specimen chamber. The final lens further demagnifies the beam into a small spot, about 0.1-1 µm in diameter and moves it up and down in space until it reaches the specimen surface. Apart from its focusing capabilities, the objective lens also determines the intensity of the beam upon striking the specimen and hence controls the image brightness. Figure 3.1 is a schematic representation of the electron-optical column of a SEM.

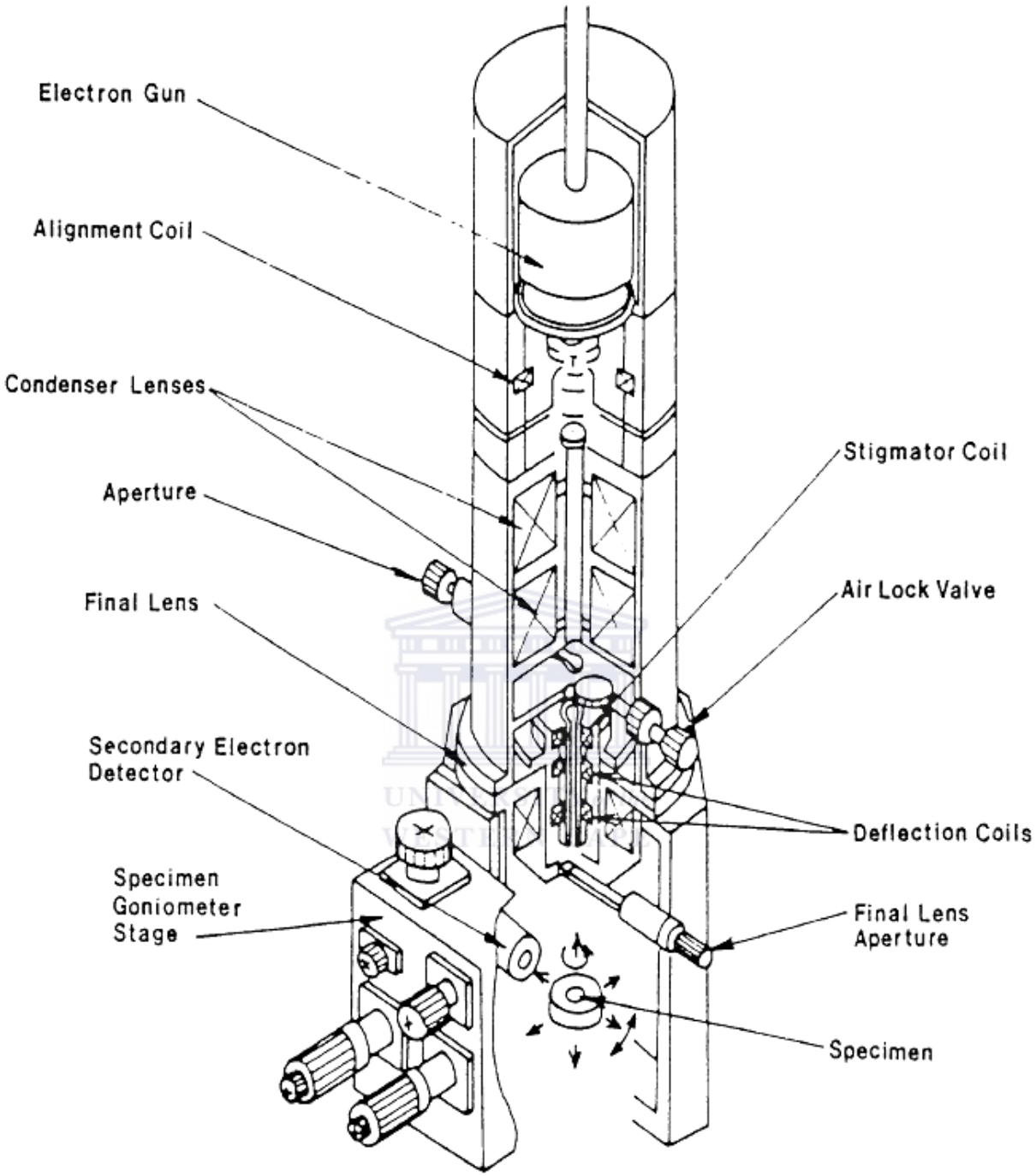

Figure 3.1: Schematic representation of the components comprising the SEM column [3.1]

3.2.2 Resolution

A very important factor when performing microscopy (perhaps even more important than magnification) is the apparatus's resolution. Resolution can be described as that distance at which two objects are observed as two separate entities. Obtaining great magnifications without sufficient resolution is not a desired result when operating the SEM, since no valuable information will be gathered from such images. Mathematically, the limit of resolution, i.e. the smallest separation distance at which two objects are resolved, is described by Abbe's equation [3.1].

$$d = \frac{0.612\lambda}{n\sin\alpha} \qquad (3.1)$$

where d = limit of resolution
λ = wavelength of the energy source (beam)
n = refractive index of the medium through which the energy source travels, and
α = aperture angle.

As can be observed from equation (3.1) various factors determine the degree of resolution attainable within a SEM. The influence of these on the resolution factors will be discussed in the sections below.

3.2.3 Influence of the Working Distance on Depth of Field and Resolution

Depth of field (DOF) refers to that part of the specimen that appears in focus in the final image. The working distance, which is defined as the distance between the final condenser lens pole piece and the uppermost part of the specimen (see Figure 3.1), directly influences the depth of field observed for a particular sample. A short working distance results in the sample being scanned with a wider angle (aperture solid angle, α) of electrons, thus resulting in an image with low depth of field, whereas when the sample is scanned at a longer working distance the aperture angle decreases, resulting in a greater DOF, as shown in Figure 3.2.

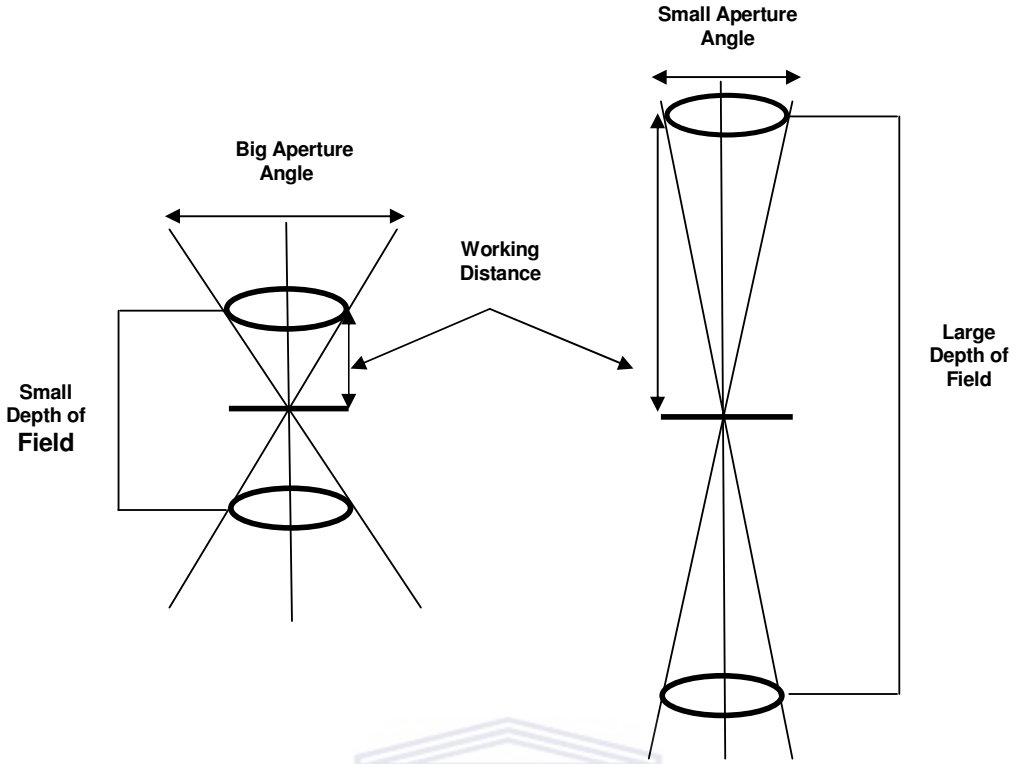

Figure 3.2: Influence of the working distance on the depth of field observed for the specimen

A change in working distance will also influence the spherical aberration of the imaging system, thus affecting the resolution of the final image. Spherical aberration is a consequence of the geometry of the electromagnetic lenses; occurring when electrons which are closer to the beam axis will refract less than those passing through the periphery of the electron beam, thus creating more than one focal point and therefore resulting in an enlarged, non-focused spot, as shown in Figure 3.3. As the working distance decreases, however, the spherical aberration effects become less, resulting in a smaller, more focused beam spot; yielding a better resolved final image.

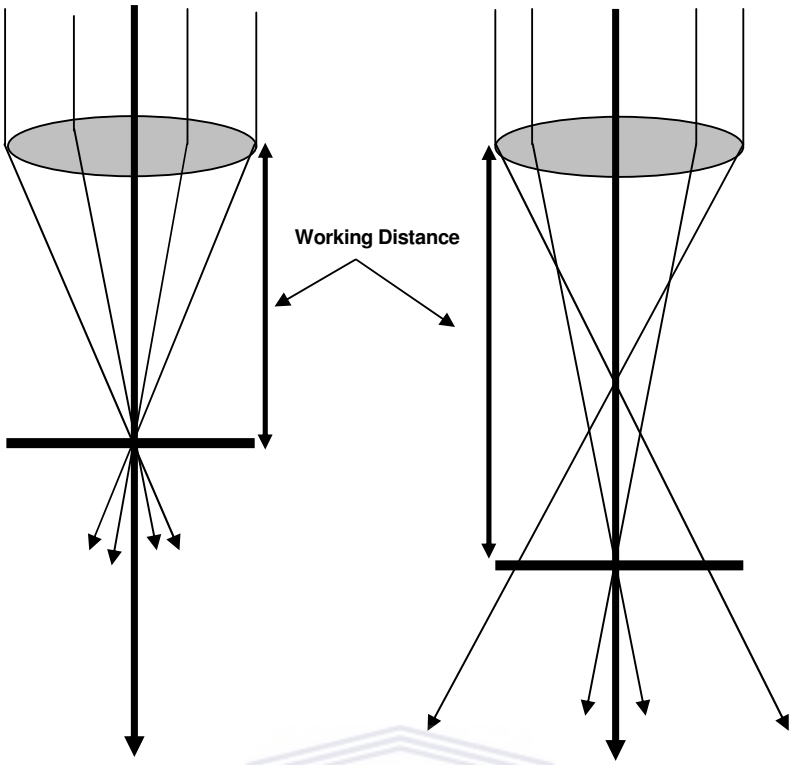

Figure 3.3: Effect of working distance on the amount of spherical aberration and resolution of the final image

3.2.4 Electron Beam – Specimen Interaction

Upon interaction of the primary beam electrons with the specimen sample, several signals get detected within the SEM, providing valuable information about the sample's surface morphology and the specimen's composition. Signals including the secondary, backscattered and transmitted electrons as well as the specimen current all provide information about the surface features of the specimen whereas characteristic x-rays, cathodoluminescence and Auger electron signals give information regarding the composition of the specimen. Table 3.2 summarizes these different signals as well as the information it offers, whereas Figure 3.4 gives a schematic illustration of the signals generated.

Table 3.2: Signal generation within the SEM and information gathered [3.1]

Event	Between	Signal	Resolution	Use
Elastic scattering	Beam electrons / specimen nuclei or electrons	Backscattered electrons	> 1 micron 1000 nm	Atomic number contrast Topographical contrast
Inelastic scattering	Beam electrons or backscattered electrons / specimen electrons	Secondary electrons	10 nm or better	Surface structure
Recombination	Free electrons generated/ positive holes	Cathodoluminescence	< 80 nm	Impurity concentration
		Characteristic x-rays	Measured in eV's, an integral of peak width of a given line	Elemental composition
		Auger electrons	Measured in eV's, an integral of peak width of a given line	Surface composition
Transmission	Electrons through specimen	Transmitted electrons	5 nm or better	Internal ultra-structure
Energy transfer	Specimen/ground	Specimen current	Poorer than 2° electron image	Atomic number contrast
Inelastic scattering	Beam electrons or backscattered electrons / specimen nuclei	Continuum x-rays		Not a useful signal

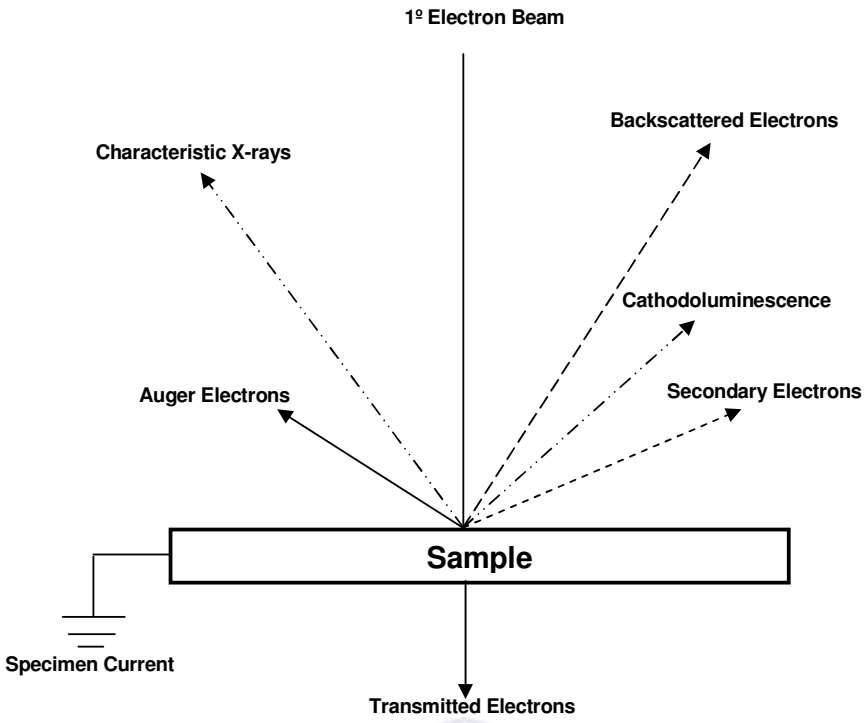

Figure 3.4: Schematic illustration of the signals generated during the primary electron beam – specimen interaction

3.2.5 Secondary Electrons and Image Formation Within the SEM

When the electron beam interacts with the specimen an 'interaction volume' is created in which the electrons undergo various scattering events. During these interactions secondary products such as secondary electrons, backscattered electrons, x-rays, heat and light forms. Image formation of the surface of a specimen depends mainly on the production of secondary electrons. Secondary electrons are low-energy electrons and thus will be absorbed by the sample when they are produced deep within the interaction volume; only those close to the surface usually have sufficient energy to escape as shown in Figure 3.5, therefore it is noted that the secondary electron image provides a surface profile of the specimen.

The secondary electron image is the most common type of image used by modern SEMs and offers greater resolution compared to the other scanning signals. Structures down to 10 nm and better can be resolved by the secondary

electron signal. The secondary electron detector, surrounded by a positively charged Faraday cup captures the electrons, whose energy is then converted into photons by means of a scintillator. These photons are then reflected down a 'light pipe' where they are amplified into an electronic signal by a photocathode and photomultiplier. This signal is subsequently used to control the brightness of the image in proportion to the initial number of photons produced and allows for the distinction in contrast of the sample surface.

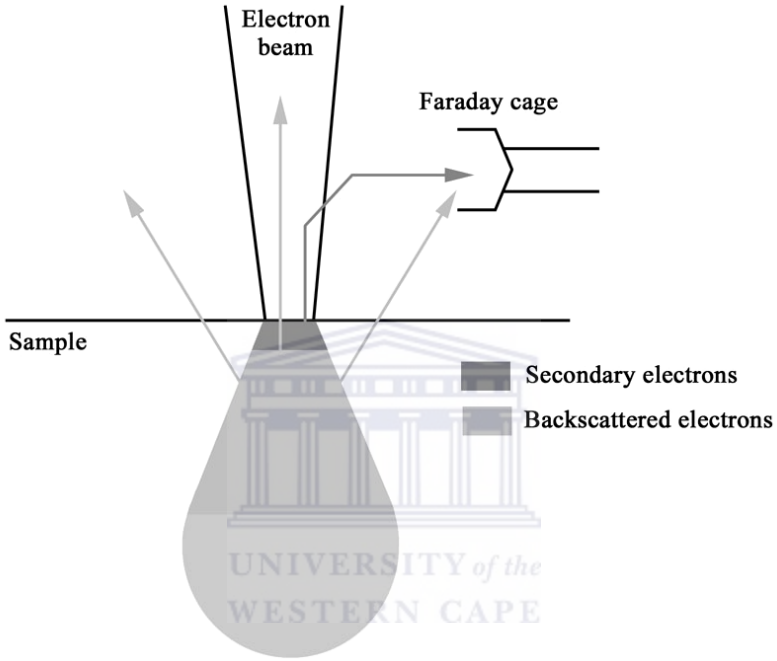

Figure 3.5: Interaction volume between the electron beam and the specimen [3.1]

3.2.6 Influence of Accelerating Voltage on the Resolution

The accelerating voltage is the voltage that is applied to the filament. The applied voltage creates a current through the filament, causing it emit electrons. Accelerating voltages often used in SEM work varies between 5 kV and 20 kV and in general, an increase in accelerating voltage will decrease the amount of spherical aberration of the system thereby enhancing its resolution. However, varying the accelerating voltage will also influence the electron beam–specimen interaction. If a higher accelerating voltage is used the interaction volume

between the beam and the specimen will increase due to the more energetic electrons in the beam.

The resolution of the system is also directly dependent on the area from which secondary electrons are emitted and normally this area is determined by the initial beam spot size. However, by increasing the accelerating voltage, backscattered electrons, which get emitted from a larger area of the sample, will interact with the specimen on their way out, thus producing secondary electrons further away from the original beam spot size (Figure 3.5), which then also decrease the image resolution.

3.2.7 Characteristic X-rays and Energy Dispersive Spectroscopy (EDS)

Consider the schematic representation of an atom in Figure 3.6. The energy levels surrounding the nucleus of the atom are termed 'shells'. These shells are labelled K, L, M, … corresponding to the principle quantum number, n = 1, 2, 3. Upon interaction of the electron beam with this atom, it may dislodge one of the inner electrons, e.g. the atom in shell K. When this happens the atom is in an excited state. To return to its normal, ground state, an electron from one of the outer shells (e.g. L or M) needs to fill the vacancy left behind in the K shell. The difference in energy undertaken by the outer shell electron is a discrete amount, characteristic of the atom and is emitted as x-rays.

When an electron from the L shell fills the K shell vacancy, the resulting x-ray is termed K_{α}, whereas when an M shell electron fills the vacancy K_{β} x-rays are emitted. The same nomenclature applies when an electron from an outer shell (e.g. L) is knocked out.

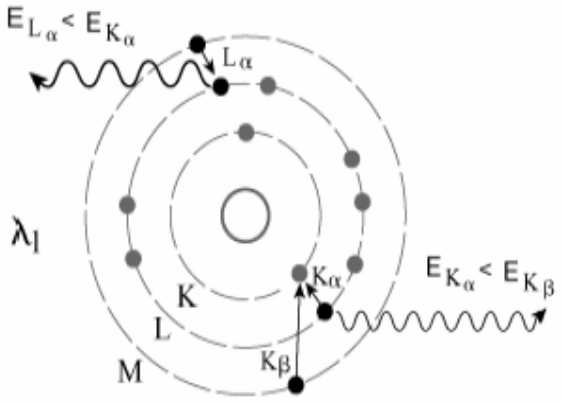

Figure 3.6: Characteristic x-ray emission by an atom [3.1]

The phenomenon pictured in Figure 3.6 forms the basis for energy dispersive spectroscopy (EDS). The technique employs energy dispersion, which is the separation of x-rays according to their energy. This separation of energy is accomplished with the help of a semiconductor detector. When an x-ray strikes a semiconductor crystal, electrons in the crystal absorb a given amount of energy and are thus excited. The greater the x-ray energy, the greater the amount of electrons excited. The absorbed energy is then converted to an electronic signal, which is emitted and amplified. The strength of the current from the crystal is proportional to the x-ray energy. The amplified electrical pulses from the semiconductor are converted to digital form and fed into a multi-channel analyzer (MCA). The MCA sorts these signals and, in effect, counts the number of x-rays at each energy level that strikes the crystal. This information is then plotted as a spectrum. Figure 3.7 shows a typical EDS spectrum for a tungsten filament and compares it to that of a filament operated in a methane/hydrogen atmosphere (as discussed in Chapter 2).

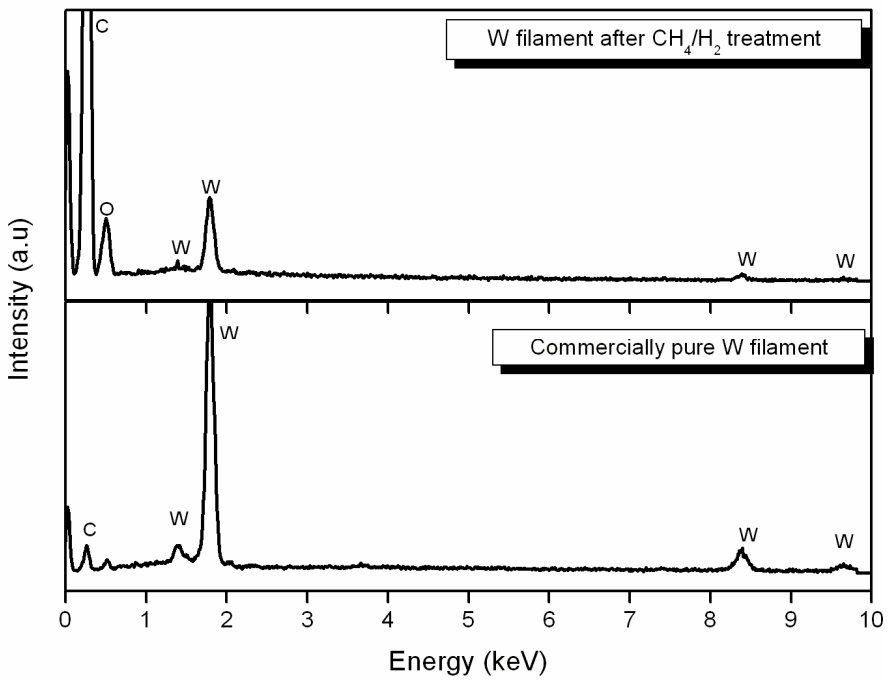

Figure 3.7: Typical EDS spectrum of a commercially pure tungsten filament compared to that of a filament operated in methane/hydrogen gas atmosphere

3.2.8 Sample Preparation

In order to obtain an image of a non-conductive specimen with the SEM, it must first be covered with an electrically conductive coating. This coating increases the sample's electrical conductivity, reduces the thermal damage caused by the beam to the sample, increases secondary and backscattered electron emission as well as the sample's mechanical stability.

Upon interaction of the primary beam with the sample there is a build up of charge, which must be dissipated in some way. For conductive specimen this is not a problem as the charge is conducted through the specimen and eventually is grounded by contact with the specimen stage. However, if the specimen is non-conductive, the charge builds up and causes 'charging'. Charging results in the deflection of the electron beam and some secondary electrons, periodic bursts of secondary electrons and increased emission of secondary electrons from cracks and defects within the sample, which all serve to degrade the final

image of the specimen. Furthermore, because the coating helps to swiftly transfer the electrons of the beam away from the scanned region, it also avoids the build up of excessive heat, which can damage the sample. The coating of non-conductive specimen also serves to increase the number of secondary electrons produced. This is so since specimen of higher atomic number more readily produces secondary electrons, thereby contributing to an overall improved image. In conclusion, conductive coatings also help to improve the sample's mechanical stability, which is especially of interest for samples which are beam sensitive, as the coating actually holds the sample together.

3.3 X-Ray Diffraction

3.3.1 Introduction

X-rays are electromagnetic radiation similar to light, but with much smaller wavelength and are produced when a fast moving electron is rapidly slowed down. Diffraction is a phenomenon that occurs when waves interfere with a structure whose repeat distance is about the same as that of the incident wavelength. Upon interaction constructive and destructive interference patterns result due to the scattering of the incoming wave fronts by the structure. The wavelength range of x-rays is about the same as that of the interatomic spacing found in three-dimensional crystalline structures, meaning that x-rays can be diffracted by these crystalline structures with each atom in the crystalline structure serving as a scattering center for the incoming wave fronts. This phenomenon is known as x-ray diffraction (XRD) and can be used as a tool for the investigation of the fine, crystalline structure of matter. In this study, XRD will be used to investigate the interlayer spacing in MWCNTs, identification of the various phases in the deposited material and the degree of crystallinity and impurities of the resulting CNTs.

3.3.2 Theory of X – Ray Diffraction

3.3.2.1 Crystal Structure and Bravais Lattices

The atoms found in materials can be either randomly distributed, thus making the material amorphous or they can be arranged in a periodic pattern in three dimensions, resulting in the material being crystalline. When thinking about the atomic arrangement within a crystal, it is best to imagine the atoms as a set of imaginary points with a fixed relation in space. Figure 3.8 illustrates the above concept, referred to as a point lattice and is defined as an array of points in space, so arranged that each point have identical surroundings.

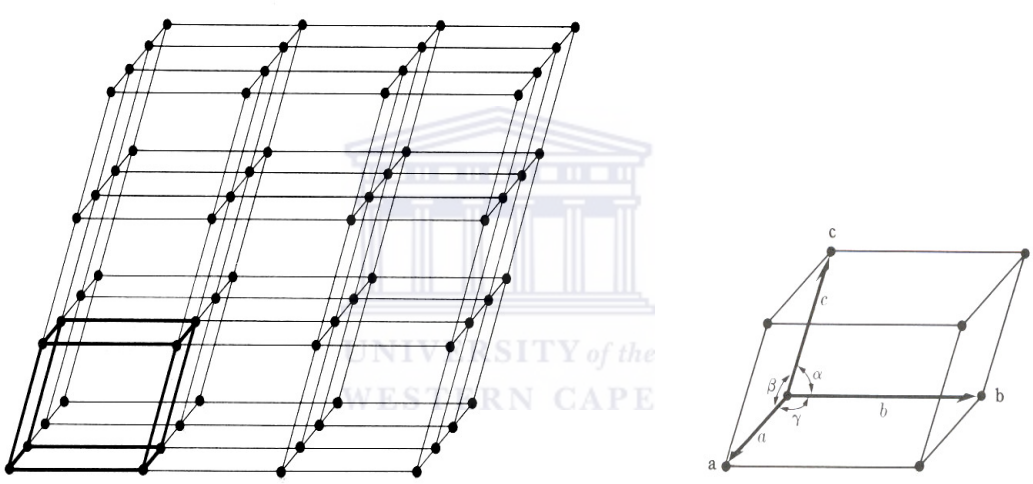

Figure 3.8: Illustration of a point lattice with its unit cell [3.2]

By drawing three vectors $\vec{a}$, $\vec{b}$ and $\vec{c}$ from the corner of any lattice point, one generates a point lattice unit cell. These vectors, known as the crystallographic axes of the unit cell can also be described in terms of their lengths (a, b and c) and the angle between them (α, β and γ), known as the lattice constants or lattice parameters as shown in Figure 3.8. Not only do the crystallographic axes define the unit cell, but it also defines the whole point lattice, which can be produced by repeated action of the vectors. Depending on the relationship between the lattice parameters (i.e. a, b, c, α, β and γ) one can distinguish between fourteen different point or Bravais lattices, as described in Table 3.3.

The direction of any vector within the Bravais lattice is given as a linear combination of the three crystallographic axes as:

$$\vec{x} = u\vec{a} + v\vec{b} + w\vec{c} \qquad (3.2)$$

where $\vec{a}, \vec{b}, \vec{c}$ = any vector in the Bravais lattice

u, v, w = coordinates of any point on the vector

In short, equation (3.2) can be written as [u v w] as shown in Figure 3.9. Furthermore, directions related by symmetry are known as directions of a form, and are represented by angular brackets, e.g. the four body diagonals of a cube, [111], $[\bar{1}\,11]$, $[1\,\bar{1}\,1]$ and $[11\,\bar{1}]$ are represented by <111> where the negative directions are indicated by a barred index. Furthermore, [u v w] are always converted to a set of smallest integers, e.g. [2 2 4] and $[\frac{1}{2}\,\frac{1}{2}1]$ represents the same direction, with [1 1 2] the preferred notation. Collectively, all of these vectors form the reciprocal space of the lattice, or reciprocal lattice.

Given any Bravais lattice, a lattice plane is defined as any plane containing at least three non-collinear lattice points. A family of lattice planes is a set of parallel planes, which together contain all the points of the three-dimensional Bravais lattice. For cubic systems, there is an intrinsic relationship between the family of lattice planes and the vectors in the reciprocal lattice, which provides a convenient way of specifying the orientation of the lattice planes in space.

Table 3.3: Description of the fourteen Bravais lattices [3.2]

System	Axial lengths and angles	Bravais lattice	Lattice symbol
Cubic	Three equal axis at right angles $a = b = c, \alpha = \beta = \gamma = 90^{\circ}$	Simple Body-centered Face-centered	P I F
Tetragonal	Three angles at right angles, two equal $a = b \neq c, \alpha = \beta = \gamma = 90^{\circ}$	Simple Body-centered	P I
Orthorhombic	Three unequal axes at right angles $a \neq b \neq c, \alpha = \beta = \gamma = 90^{\circ}$	Simple Body-centered Base-centered Face-centered	P I C F
Rhombohedral	Three equal axes, equally inclined $a = b = c, \alpha = \beta = \gamma \neq 90^{\circ}$	Simple	R
Hexagonal	Two equal co-planar axes at 120 º, third axis at right angles $a = b \neq c, \alpha = \beta = 90^{\circ}, \gamma = 120^{\circ}$	Simple	P
Monoclinic	Three unequal axes, one pair not at right angles $a \neq b \neq c, \alpha = \gamma = 90^{\circ} \neq \beta$	Simple Base-centered	P C
Triclinic	Three unequal axes, unequally inclined and none at right angles $a \neq b \neq c, \alpha \neq \beta \neq \gamma \neq 90^{\circ}$	Simple	P

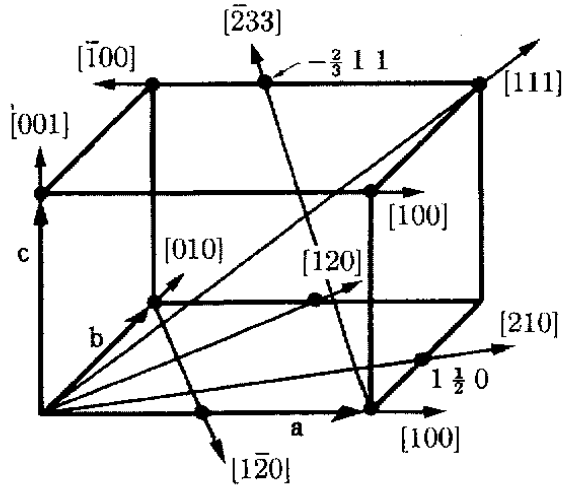

Figure 3.9: Indices for directions for a general unit cell [3.2]

Generally for cubic systems, the orientation of a plane is given by the vector normal to it and is denoted by Miller indices, h k l, contained in round brackets, e.g. (h k l). In Figure 3.10 the vector $\vec{n} = \frac{\vec{a}_1}{h} + \frac{\vec{a}_2}{k} + \frac{\vec{a}_3}{l}$ is normal to the plane (h k l) that intercepts the unit cell at $\frac{\vec{a}_1}{h}, \frac{\vec{a}_2}{k}$ and $\frac{\vec{a}_3}{l}$, where $\vec{a}_1$, $\vec{a}_2$ and $\vec{a}_3$ are the crystallographic axes. Similar to lattice vectors, planes related by symmetry are called planes of a form and is denoted by {h k l}.

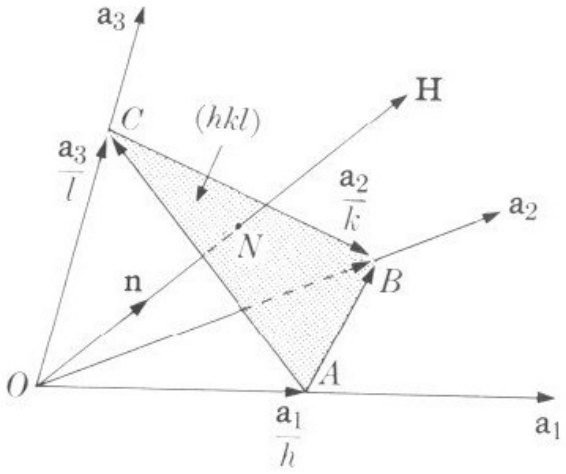

Figure 3.10: Relationship between the reciprocal lattice vector and the crystal plane (h k l) [3.2]

3.3.2.2 Bragg's Law for Diffraction

In Figure 3.11, a monochromatic beam of parallel x-rays, O and O', strikes a stack of planes (h k l) spaced a distance d apart at an angle θ. Each plane consists of a series of equally spaced atoms, each of which is capable of scattering the incident radiation. The scattered rays P and P', resulting from the interaction of the incident beam with the atoms of the parallel planes, will recombine to form a diffracted beam if and only if their path difference is an integer multiple of wavelengths, i.e.

$$CA + AD = d\sin\theta + d\sin\theta = n\lambda \tag{3.3}$$

where
- n = integer multiple (order of diffraction)
- λ = wavelength of the radiation
- d = interplanar spacing
- θ = incident angle (Bragg angle)

Equation (3.3) can be simplified to give

$$2d\sin\theta = n\lambda \tag{3.4}$$

which is known as Bragg's law and gives the angle θ, at which a set of planes (h k l) of spacing d constructively reflects x-rays of wavelength λ in the n^{th} order.

3.3.2.3 Atomic and Structure Factors

A quantity f, called the atomic scattering (or form) factor, is used to describe the 'efficiency' with which a given atom scatters an incident x-ray beam in a given direction and is defined by

$$f = \frac{\text{amplitude of the wave scattered by an atom}}{\text{amplitude of the wave scattered by one electron}} \tag{3.5}$$

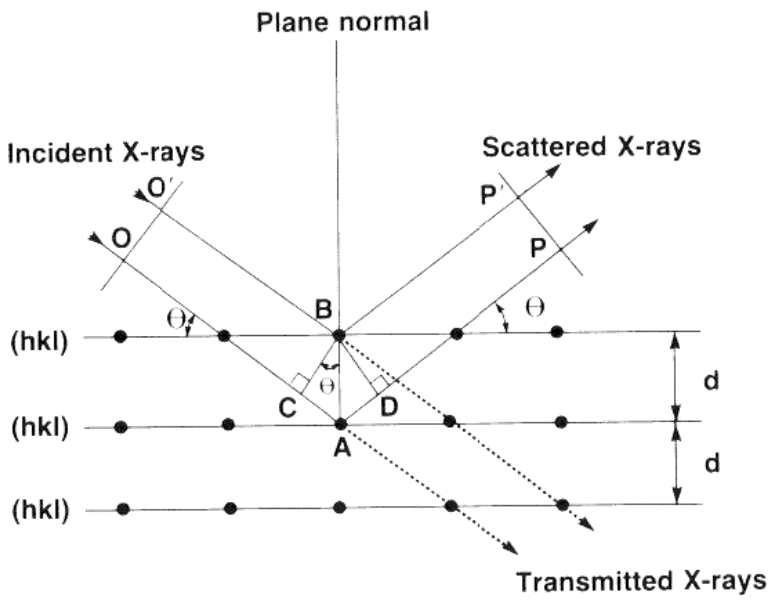

Figure 3.11: Conditions for Bragg's law [3.3]

The scattering of the incident wave by an atom depends on the arrangement of the electrons within the atom, however when scattering by the unit cell of the crystal is considered, the scattering process depends on the atomic arrangement within the cell. The wave diffracted by a unit cell containing 1, 2, 3,…, N atoms each with fractional coordinates u_1 v_1 w_1, u_2 v_2 w_2, u_3 v_3 w_3,…, u_N v_N w_N and atomic scattering factors f_1, f_2, f_3,…, f_N is called the structure factor, F_{hkl} and is defined by:

$$F_{hkl} = \sum_{1}^{N} f_n e^{2\pi i(hu_n + kv_n + lw_n)} \qquad (3.6)$$

with the summation extending over all N atoms of the unit cell. The absolute value of F_{hkl} gives the amplitude of the resultant wave in terms of the amplitude of the wave scattered by a single electron. The intensity of the beam diffracted by all the atoms within the unit cell is proportional to $|F_{hkl}|^2$. Furthermore, the structure factor is independent of the relationship between the lattice parameters and thus only depends on the number and position of the atoms within the unit cell of the Bravais lattice, i.e. only depends on whether the unit cell is primitive, body-centered, etc.

3.3.3 Instrumentation

The apparatus with which x-ray diffraction is performed is called an x-ray diffractometer as shown in Figure 3.12 and consists of three basic parts:

- An x-ray source (S and T in Figure 3.12)
- The diffractometer circle and
- A detector system (G and E).

In Figure 3.12 the detector (G) is placed on the circumference of a circle centered at the specimen stage, C. The specimen is supported on a Table H, which can rotate about an axis, O, perpendicular to this page. X-rays diverge from the source at S and are diffracted by the specimen at C to form a convergent diffracted beam, which focuses at the slit F before entering the detector at G, supported on a carriage, E. The carriage also rotates about the axis O and has an angular position 2θ. The supports H and E are mechanically locked in a θ-2θ relationship. A and B are special slits that define and collimate the incident and diffracted beams. A filter is placed in the diffracted beam-path to suppress the K_β radiation and to decrease the background radiation originating in the specimen.

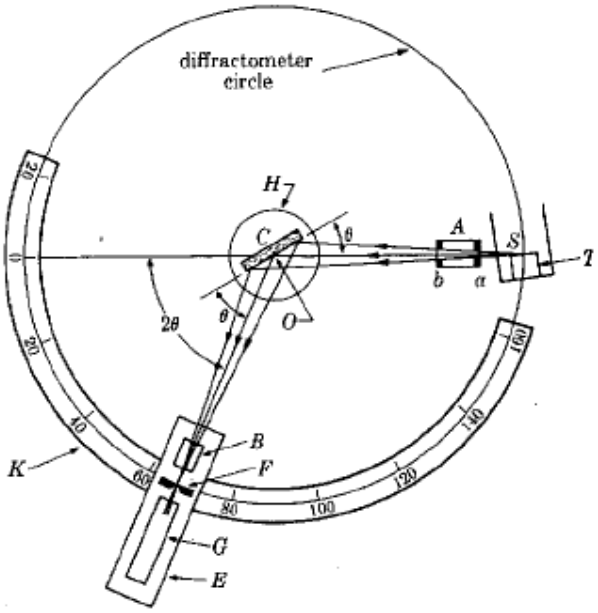

Figure 3.12: X-ray diffractometer [3.2]

3.3.4 Characterization

The x-ray diffraction technique is used to obtain information on the interlayer spacing in MWCNTs and the impurities of CNT samples. Diameter and chiralities distribution can also be determined. Therefore, the XRD technique can be employed for a statistical characterisation of CNTs [3.4].

Figure 3.13 shows a typical XRD spectrum of MWCNTs. Due to their close relationship with graphite, the main features of the XRD pattern of CNTs are close to that of graphite. The (0 0 2) peak present is termed the 'graphite peak' and is indicative of the graphitic nature of CNTs. A measure of the interlayer spacing of MWCNTs can be obtained from this peak's position and using Bragg's law. The family of (h k 0) peaks represent the honeycomb lattice of a single graphene sheet.

The intensity and width of the (0 0 2) peak are directly related to the number of layers, variations in interlayer spacing, the lattice distortions as well as to the CNT orientation compared to the incident XRD beam. Furthermore, the asymmetric shape of the (h k 0) peaks presents the curvature of the nanotubes, whereas the family of (h k l) reflections only appear in XRD patterns with a regular stacking of layers (i.e. as in MWCNTs) [3.4]. Cao *et al*. [3.5] showed that no (0 0 2) peaks could be measured by XRD when the CNTs are aligned parallel to the incident beam. In this case the beam is scattered inside the tube and hence the beam is not collected. Therefore, the intensity of the (0 0 2) peak decreases monotonically as the CNTs are better aligned.

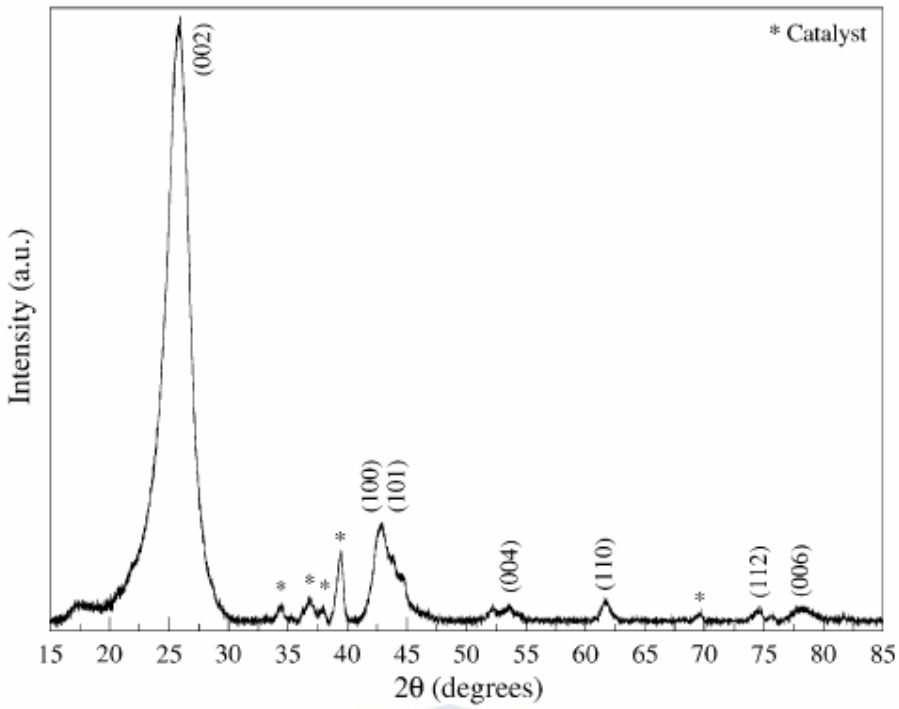

Figure 3.13: X-ray diffraction spectrum of MWCNTs [3.4]

3.4 Raman Spectroscopy

3.4.1 Introduction

Raman spectroscopy is the study of the chemical structure and physical form of a molecule, identification of substances from characteristic spectral patterns and quantitative determination of the amount of a substance in a sample. The underlying process of Raman spectroscopy is Raman scattering, during which monochromatic radiation, used to irradiate the sample, is scattered from the molecule, one vibrational unit of energy different from the incident beam. This unit of energy, which is characteristic of the scattering molecule then gets detected and measured thus allowing for the identification of the vibrations of a molecule. In this study Raman spectroscopy will be employed to determine the different carbon nanotube structures (SWCNTs or MWCNTs), the chirality of the tubes (zigzag or armchair, if the tubes are single walled) and the electronic properties of the nanotubes, i.e. metallic or semi-conducting.

3.4.2 Theory of Raman Spectroscopy

3.4.2.1 Scattering of a Light Wave by a Molecule

When light interacts with matter, one of two processes can occur, namely scattering or absorption. Scattered radiation is released when the light wave, which can be considered as an oscillating dipole, transfers its energy to the molecule, subsequently distorting (polarising) the electrons around the nuclei of the molecule causing it to go to a higher energy state. This interaction can be considered as the formation of a 'complex' between the light energy and the electrons in which the nuclei of the molecule do not have enough time to move appreciably. This complex is not stable, resulting in the light being released almost immediately as scattered radiation [3.6]. This process differs from light absorption in the following ways:

- The additional light energy does not promote an electron to a higher energy state of the molecule; instead all states of the molecule are involved to different extents and are mixed to form states of the distorted 'complex'.
- The lifetime of the excited state is very short compared to most absorption processes and the radiation is scattered as a sphere and is not lost by energy transfer within the molecule or emitted at a lower energy.

Two types of scattering exist. The most intense form is Rayleigh scattering, which occurs when the electron cloud relaxes without any nuclear movement. This process is essentially elastic since no appreciable change in energy of the molecule is observed. On the other hand, Raman scattering, which is a much rarer event as compared to Rayleigh scattering, occurs when the light and the electrons interact and the nuclei begin to move at the same time. Since the nuclei are much heavier than the electrons, there is an appreciable change in energy of the molecule to a lower or higher energy, depending on whether the electron was initially in the ground state or in a vibrationally excited state. When the molecule is initially in the ground state the process is known as Stokes scattering, whereas when the molecule starts off in an excited state, anti-Stokes scattering occurs. Figure 3.14 shows these two scattering processes compared to Rayleigh scattering.

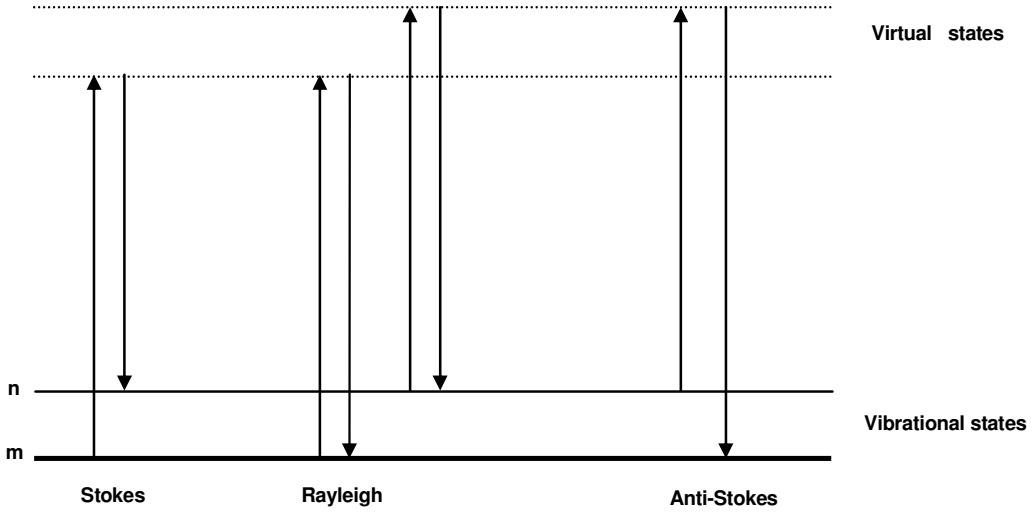

Figure 3.14: Diagram of the Rayleigh and Raman scattering processes [3.6]

Rayleigh scattering will be the most intense process since most photons (one quantum of light energy) scatter in this manner. Usually Raman scattering is only recorded on the low-energy side to give Stokes scattering, since this signal is much more intense than the anti-Stokes scattering signal. This is because at room temperature not a lot of molecules are in the excited state, n in Figure 3.14.

3.4.2.2 Hooke's Law

Hooke's law gives the relationship between the frequency, mass of the atoms involved in the vibration and the bond strength for a diatomic molecule:

$$v = \frac{1}{2\pi c}\sqrt{\frac{K}{\mu}} \tag{3.7}$$

where v is the frequency, c is the speed of light, K is force constant of the bond between atoms A and B, and μ the reduced mass of A and B with masses M_A and M_B. μ is given by

$$\mu = \frac{M_A M_B}{M_A + M_B} \tag{3.8}$$

Hookes's law allows easy approximations of the order of energies of specific vibrations; the lighter the atoms, the higher the frequency will be and vice versa. The force constant, K is a measure of the bond strength, thus the stronger the bond the higher the measured frequency.

3.4.2.3 Selection Rules for Raman Scattering

Provided there is no change in electronic energy, the energy of a molecule can be divided into a number of degrees of freedom. Three of these are taken up to describe the translation of the molecule in space and a further three to describe rotational movement. However, for linear molecules (i.e. two atoms bonded at an angle of 180 ºC) only two types of rotation are possible; the molecule can either rotate around the axis or about it. Hence, for a molecule consisting of N atoms the number of vibrational degrees of freedom will be 3N – 6, and 3N – 5 for linear molecules.

For example, a diatomic molecule such as oxygen only has one vibration, which is a stretch of the O-O bond. This stretch will change the polarizability of the molecule. Intense Raman scattering occurs from vibrations which cause a change in the polarizability of the electron cloud of the molecule [3.6]. The change in polarizability causes the movement of the nuclei, which creates Stokes and anti-Stokes scattering. Figure 3.15 shows the vibrational modes for a triatomic molecule, H_2O. Generally the symmetrical stretch causes large polarization changes and hence strong Raman scattering, whereas the asymmetric stretches cause dipole changes, which leads to intense infrared absorption.

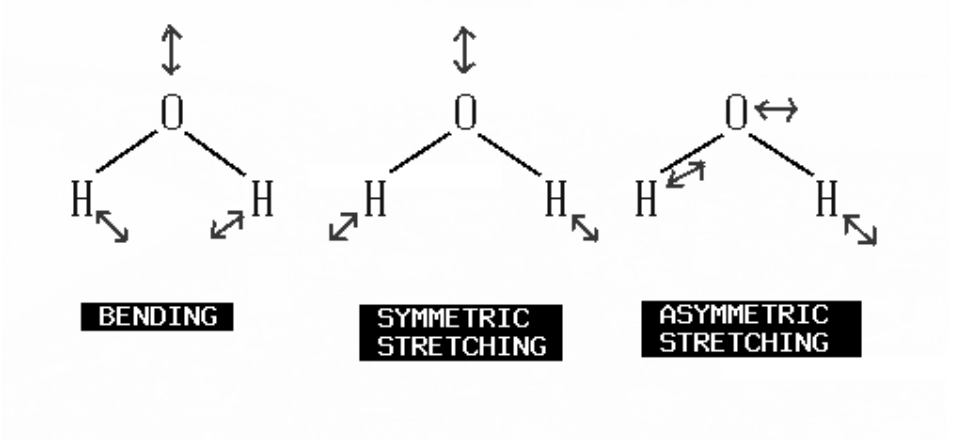

Figure 3.15: Symmetrical and asymmetrical stretches, as well as the deformation (bending) vibration of the H_2O molecule [3.6]

Mathematically the change in polarizability involves the change of a dipole, μ in the Cartesian directions x, y, z. This is given by [3.6]

$$\mu = \alpha E \tag{3.9}$$

where α is the polarizability of the electron cloud of the molecule and E the electric field of the incident photon. Usually α is labelled according to its components, e.g. α_{xx} where the first subscript refers to the direction of the polarizability of the molecule and the second x refers to the polarization of the incident light. Therefore $\mu_x = \alpha_{xx}E_x + \alpha_{xy}E_y + \alpha_{xz}E_z$. Similar expressions exist for μ_y and μ_z.

Finally the intensity of the beam scattered during Raman scattering is defined by equation (3.10):

$$I = KI\alpha^2\omega^4 \tag{3.10}$$

where K consists of constants such as the speed of light, I is the laser power, α the polarizability of the electrons in the molecule and ω the frequency of the incident radiation. Therefore, one has control over two of the parameters in equation (3.10) namely the laser power and the frequency of the incident radiation.

3.4.3 Experimental Set-up

Figure 3.16 shows a typical set-up for Raman spectroscopy. A monochromatic visible laser is used as the excitation source. The laser is passed through a pinhole, measured by a spectrometer and then collected as an expanded parallel beam. This is done in order to fill the optics of the microscope. The radiation is then deflected by mirrors towards the notch filter, which reflects the light into the microscope. After interaction of the light with the sample the scattered radiation is collected from the microscope back through the same optics. The scattered radiation then passes through the notch filter at an angle that allows transmission of the scattered radiation. This radiation is then passed through a grating and onto the charge coupled device (CCD) detector, as shown in Figure 3.16.

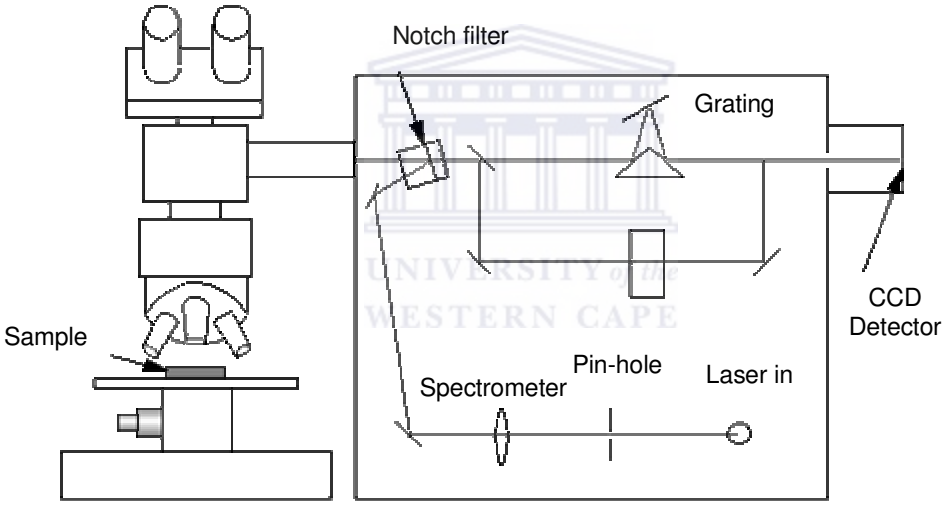

Figure 3.16: Typical set-up for Raman spectroscopy [3.6]

3.4.4 Characterization

3.4.4.1 The Radial Breathing Mode

Figure 3.17 shows a typical spectrum for single-wall carbon nanotubes. The radial breathing mode (RBM) peak shown in the Figure corresponds to the coherent vibration of the carbon atoms in the radial direction, as if the tube were

breathing. These features are unique to CNTs and occur with frequencies, ω_{RBM} between 100 and 500 cm $^{-1}$. This frequency range corresponds to a tube diameter distribution between 0.5 and 2.2 nm for isolated SWCNTs as given by [3.7]

$$\omega_{RBM} = \frac{A}{d_t} + B \qquad (3.11)$$

where the A and B parameters are determined experimentally and d_t is the diameter of the tube. For isolated SWCNTs on a SiO_2 substrate A = 248 cm $^{-1}$ nm and B = 0. Hence, it can be seen that the RBM is not only for identification of SWCNTs but an approximation for the diameter distribution of the tubes can also be obtained.

3.4.4.2 The G-Band

The G-band of CNTs is related to the tangential mode vibrations of the carbon atoms and for SWCNTs this band is composed of several peaks. The G-band frequency can be used for diameter characterisation and to distinguish between metallic and semiconducting SWCNTs.

The G-band frequency for SWCNTs consists of two main components; one peaked at 1590 cm $^{-1}$ (G^+) and one around 1570 cm $^{-1}$ (G^-) as shown in Figure 3.18. The G^+ feature is associated with carbon atom vibrations along the nanotube axis and its frequency ω_{G+} is sensitive to charge transfer from dopant additions to SWCNTs. SWCNT and its line shape is highly sensitive to whether the nanotube is semiconducting or metallic, as shown in Figure 3.18.

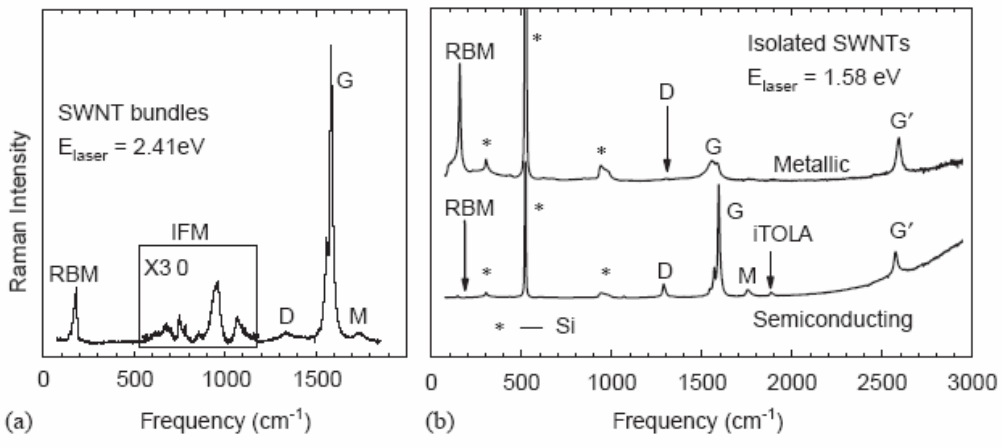

Figure 3.17: Raman spectral features of a SWCNT [3.7]

The G^- feature, in contrast, is associated with the vibrations of carbon atoms along the circumferential direction of the Raman measurements taken from a single CNT show that the frequency ω_{G+} is essentially independent of d_t or chiral angle θ, whereas ω_{G-} is dependent on d_t and whether the SWCNT is semiconducting or metallic [3.7]. For semiconducting SWCNTs the G band has the characteristic shape shown in Figure 3.18 (a) whereas when the tube is metallic the band splits into two peaks as shown in the insert of Figure 3.18 (b)

3.4.4.3 The D and G' Bands

Second order spectral features are also observed in Raman spectra of SWCNTs with the D and G' bands usually the two strongest features. The D band with ω_D ~ 1350 cm^{-1} stems from the disorder-induced mode in graphite. This band's second harmonic is the G' band which occurs at ~ $2\omega_D$. In CNTs both the d and G' bands are sensitive to the SWCNT diameter and chirality. Hence, measurement of the D and G' at single nanotube level provides unique information on the chirality and diameter dependence of ω_D and $\omega_{G'}$.

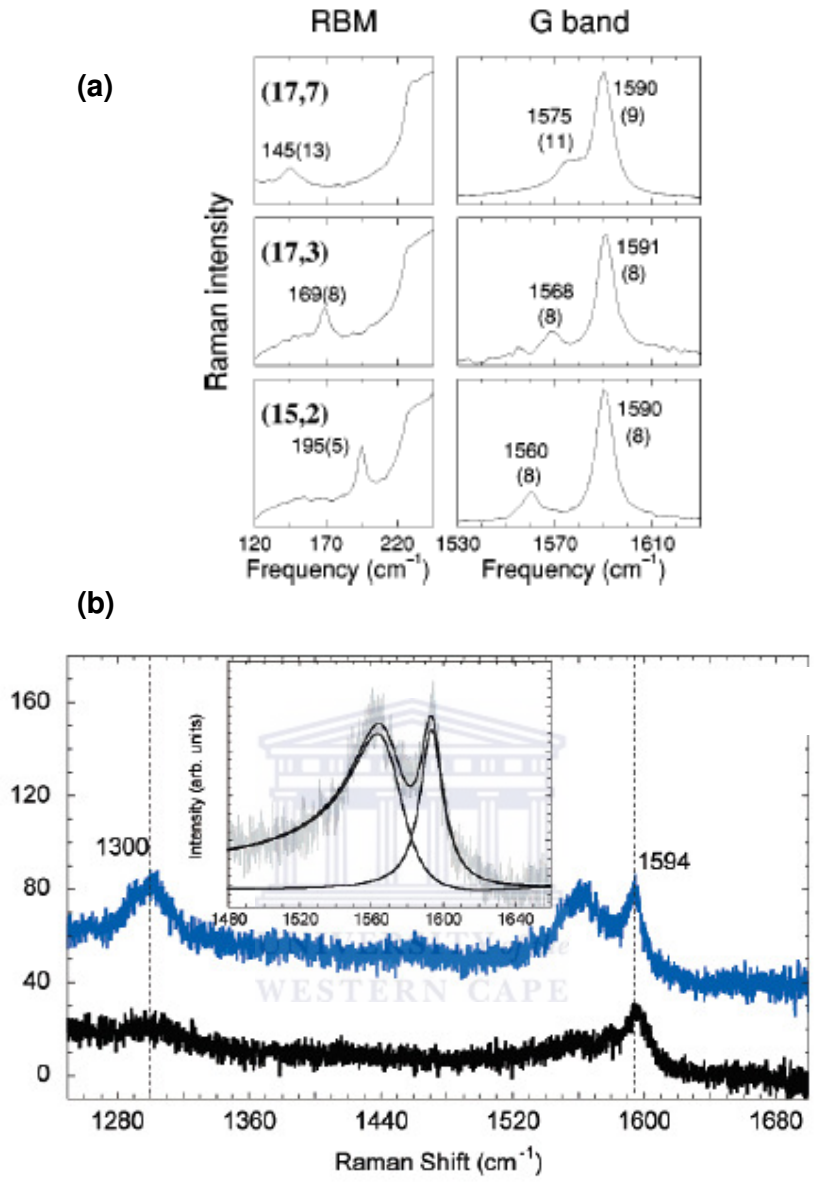

Figure 3.18: Line shape of the G band [3.7, 3.8]

3.4.4.4 Multi-Wall Carbon Nanotubes

MWCNTs usually have large outer diameters and contain an ensemble of CNTs with diameters ranging from small to very large. These factors results in the non-identification of certain characteristics that were evident in the Raman spectra of SWCNTs, e.g. the RBM mode associated with a small diameter SWCNTs tube is too weak to be observed in a Raman spectrum for MWCNTs. Furthermore, the splitting of the G-band in MWCNTs is small in intensity and

smeared out due to the effect of the diameter distribution within the individual MWCNT and because of the variation between different tubes in an group of MWCNTs in typical experimental samples. Hence, the G band predominantly exhibits a weakly asymmetric line shape, appearing close to the graphite frequency of 1582 cm^{-1}. Finally, in the case of the MWCNT Raman spectra, the D band is attributed to the vibration of the interlayers of the tube as well as instead of the defects in the graphite structure of the nanotube and other carbonaceous material. Figure 3.19 shows a typical Raman spectrum of a multi-wall carbon nanotube that will be investigated in this study.

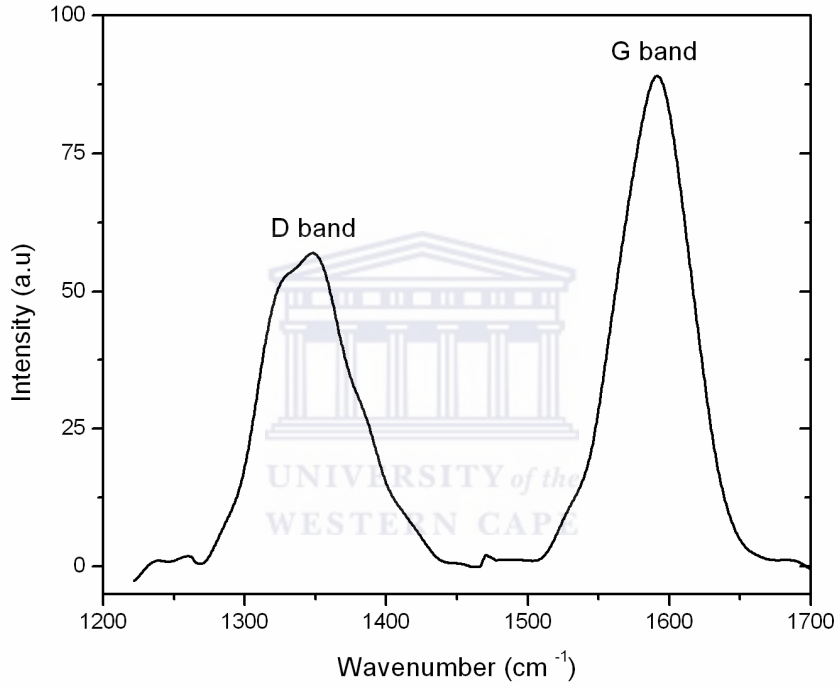

Figure 3.19: Characteristic Raman spectrum for a MWCNT

References

[3.1] P. J. Goodhew and F. J. Humphreys, Electron Microscopy and Analysis, 2nd Edition, Taylor & Francis, London (1988)

[3.2] B. D. Cullity, in Elements of X-ray diffraction, Addison-Wesley Publishing Company, Reading, Massachusetts (1978)

[3.3] F. Shimura, in '*Semiconductor silicon crystal technology*", Academic Press Inc., San Diego (1989)

[3.4] T. Belin and F. Epron, Materials Science and Engineering B, **119** (2005) 105

[3.5] A. Cao, C. Xu, J. Liang, D.Wu and B.Wei, Chemical Physics Letters, **344** (2001) 13

[3.6] E. Smith and G. Dent, '*Modern Raman Spectroscopy: A practical approach*', Wiley and Sons Ltd., Great Britain (2005)

[3.7] M. S. Dresselhaus, G. Dresselhaus, R. Saito and A. Jorio, Physics Reports, **409** (2005) 47

[3.8] M. Shim, T. Ozel, A. Gaur and C. Wang, Journal of American Chemical Society, **128** (2006) 7522

CHAPTER FOUR

Morphology

4.1 Introduction

The gas phase nature of the chemical vapour deposition (CVD) techniques results in mass production of carbon nanotubes (CNTs). Furthermore, unlike the laser ablation and arc-discharge techniques, the CVD method has also been successfully employed for the growth of well-aligned CNTs [4.1].

During hot-wire chemical vapour deposition (HWCVD), when compared to the other CVD techniques, the filament acts as the catalyst for the pyrolytic dissociation of hydrocarbon gas, subsequently giving rise to different species of material needed in the CNT growth process. The influence of the deposition parameters during HWCVD growth of CNTs with specific properties is still under investigation worldwide and a generally agreed upon theory is lacking [4.2]. These deposition parameters include the system geometry, total pressure inside the reactor, substrate temperature, substrate-to-filament distance and the methane/hydrogen dilution. Therefore, each HWCVD reactor system requires an empirical optimization of the deposition parameters in order to predict the structural properties of the resulting CNT material, i.e. the density, alignment, length and diameter.

Apart from the deposition parameters, the catalyst also plays an important role in the CNT growth process. The influence of the catalytic metallic clusters (nano-islands) on the CNT morphology has been extensively studied, as discussed in Chapter 2.5.2. However, Makris *et al*. [4.1] argue that although correlations between the CNTs and nano-island dimensions have been found, most of the features of CNTs seem to be strongly dependent on the deposition parameters. In this chapter the effect of the catalyst preparation and deposition parameters on the CNT morphology will be investigated.

4.2 Experiment

The procedure that was followed for the cleaning of the Si/SiO_2 substrates used in this study, the deposition of the nickel (Ni) catalyst for CNT growth, as well as the CNT deposition were described in Chapter 2.5. For the study of the Ni nano-island morphology, the Si/SiO_2/Ni samples were annealed at temperatures between 400 and 700 ºC in 50 ºC increments for 20 minutes at a nitrogen (N_2) gas flow rate of 230 cm^3/min.

The parameters that were investigated during the growth of the CNTs are summarized in Table 4.1. The furnace temperature, T_{fur} was increased in 100 ºC increments, the deposition pressure, P_{dep} in 50 Torr increments and the substrate-to-filament distance, d_{s-f} in 1 cm increments. Changing the scale reading on the mass flow meters of the gases varied the methane/hydrogen dilution, f_{CH4}, defined in equation 1.9. The start-off deposition parameters were as follow: T_{fur} = 500 ºC, P_{dep} = 100 Torr, f_{CH4} = 0.08 and d_{s-f} = 5 cm. These conditions were chosen based on previous successful CNT synthesis by our group using the Ni catalyst, and are to be considered the standard conditions, unless otherwise stated.

A LEO 1525 field emission scanning electron microscope (FESEM) was used for the study of the morphology of the Ni nano-islands and the resulting CNTs (National Metrology Laboratories, SA). The system was operated at beam energy between 3 and 10 kV and is equipped with a semiconductor detector that allows for energy dispersive spectroscopy (EDS) analysis. A Hitachi H800 transmission electron microscopy (TEM) operated at voltages between 150 and 200 kV was used to investigate the internal structure of the CNTs (Physics Department, University of the Western Cape).

Table 4.1: Deposition parameters for the growth of carbon nanotubes

Series	T_{sub} (°C)	ρ_{dep} (Torr)	f_{CH4} (cm^3/min)	d_{s-f} (cm)
A	300 - 900	100	0.08	5
B	500	50 - 400	0.08	5
C	500	100	0.08 – 1	5
D	500	100	0.08	5 - 10

4.3 Results and Discussion

4.3.1 Nickel Catalyst Morphology

Figure 4.1 shows selected SEM micrographs of the surface morphology of the Ni films after annealing at the conditions stated in section 4.2. It can be seen that at 400 ºC no agglomeration of the Ni atoms occurs, whereas between 500 and 600 ºC the Ni film gradually changes into clusters of diameter between 10 and 100 nm, i.e. nano-islands. At 700 ºC it can be seen that the Ni layer completely flakes from the substrate. The formation of the nano-islands is attributed to the surface tension at the interface between the Ni film and the Si/SiO_2 substrate, as well as the compressive stress due to the mismatch of the thermal expansion coefficients of the Si/SiO_2 substrate and the Ni film [4.2, 4.3].

Hence, it can be concluded that at 400 ºC, the temperature is too low for sufficient compression of the Ni film, whereas at 700 ºC the temperature is so high that the Ni film undergoes a 'thermal shock' resulting in the flaking of the Ni film rather than agglomeration into nano-islands.

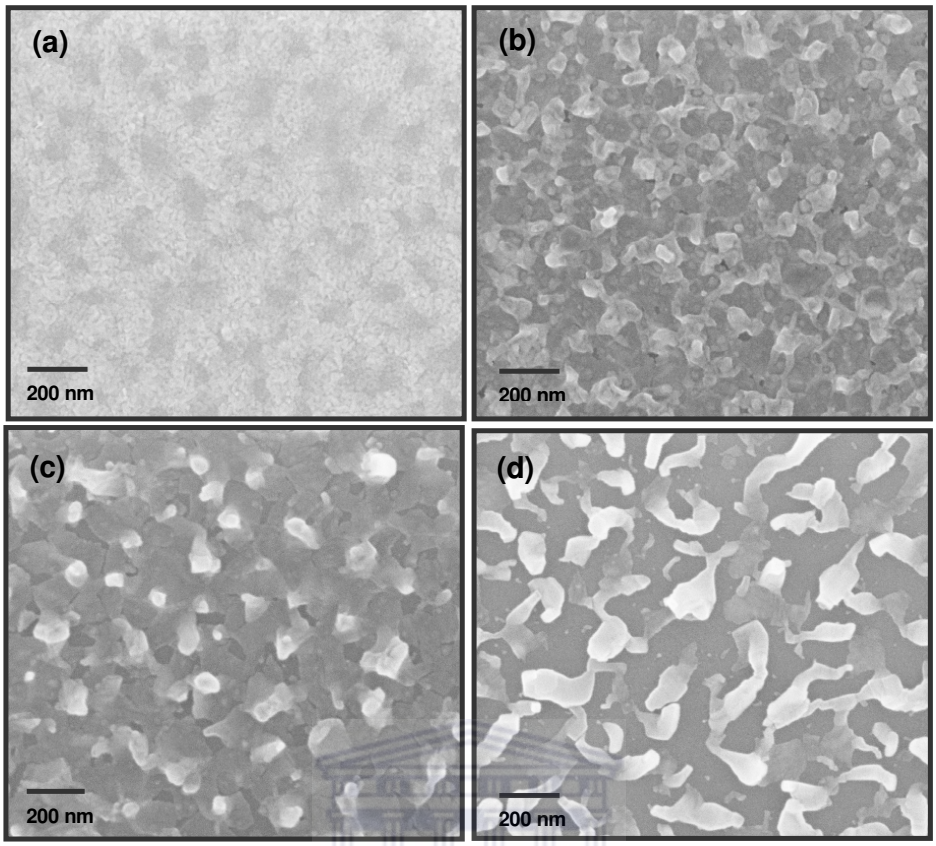

Figure 4.1: Morphology of the Si/SiO_2/Ni samples annealed at (a) 400 ºC, (b) 500 ºC, (c) 600 ºC and (d) 700 ºC for 20 minutes

4.3.2 Carbon Nanotube Morphology

4.3.2.1 Effect of the Furnace Temperature on the Carbon Nanotube Morphology

The effect of the furnace temperature (T_{fur}) on the carbon nanotube morphology will be investigated in this section (Series A). Figure 4.2 shows the SEM micrographs of fiber-like structures synthesized at the standard deposition conditions. At these conditions it can be seen that very dense volumes of entangled fibers are grown. It is also apparent that some of these fibers grow up to tens of micrometers long, as indicated by the arrows in Figure 4.2 (a). At a closer view (Figure 4.2 (b)) these fibers appear to originate from a cluster of material, which consists of carbon material as well as Ni agglomerates. From

Figure 4.2 (b) the diameter range of the resulting structures can be estimated to be between 20 and 100 nm, suggesting that these structures are multi-wall carbon nanotubes (MWCNTs). The diameter range of these MWCNTs coincides with the diameter range of the Ni nano-islands of Figure 4.1 (b) and (c), as reported by various other groups [4.2 – 4.4]. SEM micrographs taken at various spots on the sample yielded similar structures, suggesting that a homogenous deposit is obtained.

Figure 4.2 (b) also shows a deformation (buckling) in the MWCNT; shown by the arrow. This phenomenon is attributed to the stresses acting on the graphitic tube during the growth process of the CNT [4.5, 4.6]. Furthermore, it can be seen that carbon-containing nano-material resides on the outer walls of most of the nanotubes. These phenomena contribute to the defect density of the synthesized CNT material and will be discussed in the following chapter.

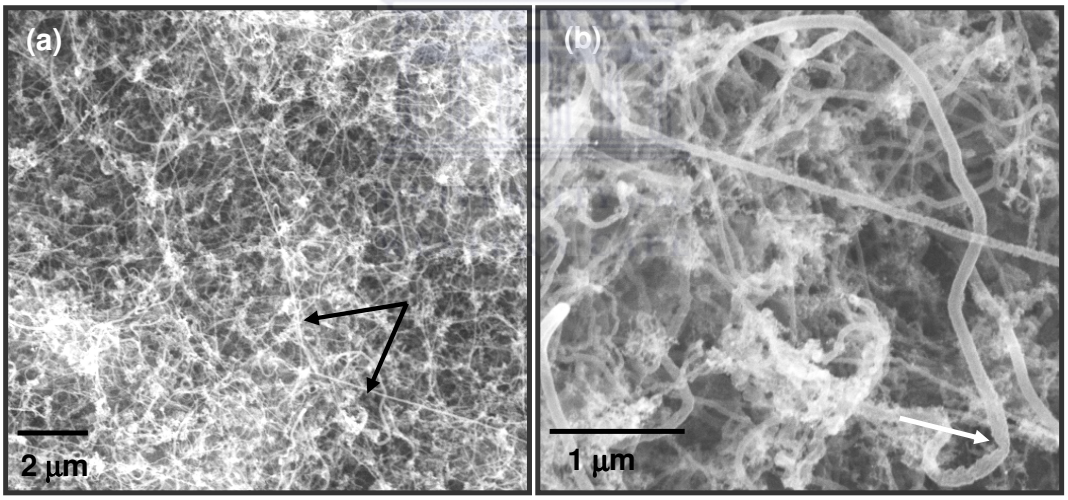

Figure 4.2: SEM micrographs of CNTs grown at the standard deposition parameters

The TEM micrographs shown in Figure 4.3 were used to investigate the internal structure of the CNTs grown at the standard conditions. Figure 4.3 confirms that MWCNTs with a diameter range of roughly 20 - 100 nm were grown at the standard deposition parameters. Furthermore, the TEM images also show the presence of the Ni clusters at the tips of the CNTs (as indicated by the arrows)

suggesting that the CNTs formed via the tip-growth mechanism. Figure 4.3 (b) also reveals how some of these Ni catalyst particles reside inside the tube walls, thereby further adding to the CNT's defect density.

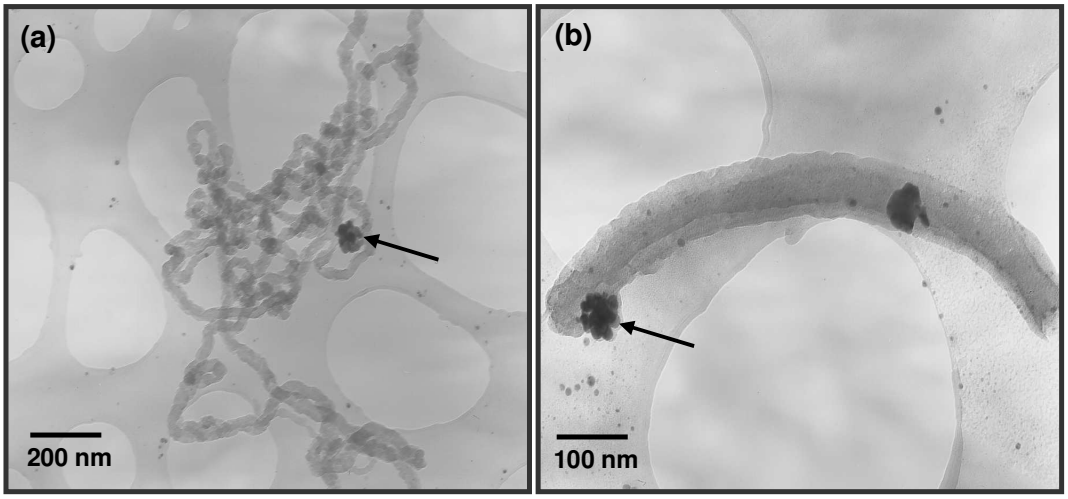

Figure 4.3: TEM micrographs of CNTs grown at the standard deposition parameters

The SEM micrographs shown in Figure 4.4 are that of spaghetti-like CNTs grown at 600 °C. The diameter range of the tubes appears similar to that of the MWCNTs grown at the standard deposition conditions, which suggests that MWCNTs are synthesized at these conditions as well. However, in comparison to the CNTs grown at 500 °C, it is noted from Figure 4.4 that there is a decrease in tube length. Furthermore, the purity of the deposited material is similar to that of the CNTs grown at 500 °C, with substantial amounts of non-CNT material present, as well as local carbonaceous nano-material on the tube walls.

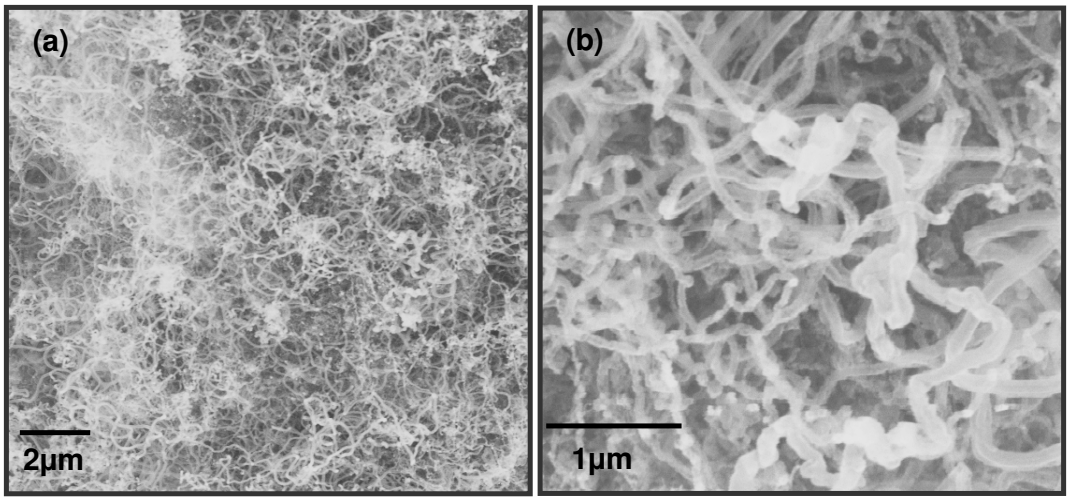

Figure 4.4: SEM micrographs of MWCNTs grown at a furnace temperature of 600 °C

The SEM micrographs shown in Figure 4.5 confirm that no carbon nanotube structures were formed at temperatures of 400 and 700 °C, respectively. Instead, at 400 °C, dense carbon material was formed, whereas at 700 °C it is observed that only nickel or carbon clusters remained after the sample was removed from the quartz tube. The absence of CNTs at these conditions is a result of the insufficient Ni nano-island formation, in accordance with reported results [4.4].

In conclusion, this section investigated the effect of the furnace temperature, T_{fur}, on the resulting CNT morphology. It was shown that T_{fur} directly controls the formation of Ni nano-islands, whose morphology, in turn, determined the growth of CNTs. Temperatures at and below 400 °C yielded no Ni nano-islands, subsequently resulting in no CNT formation. Temperatures at and above 700 °C resulted in the Ni layer flaking off the Si/SiO_2 substrate, which also results in no CNT formation.

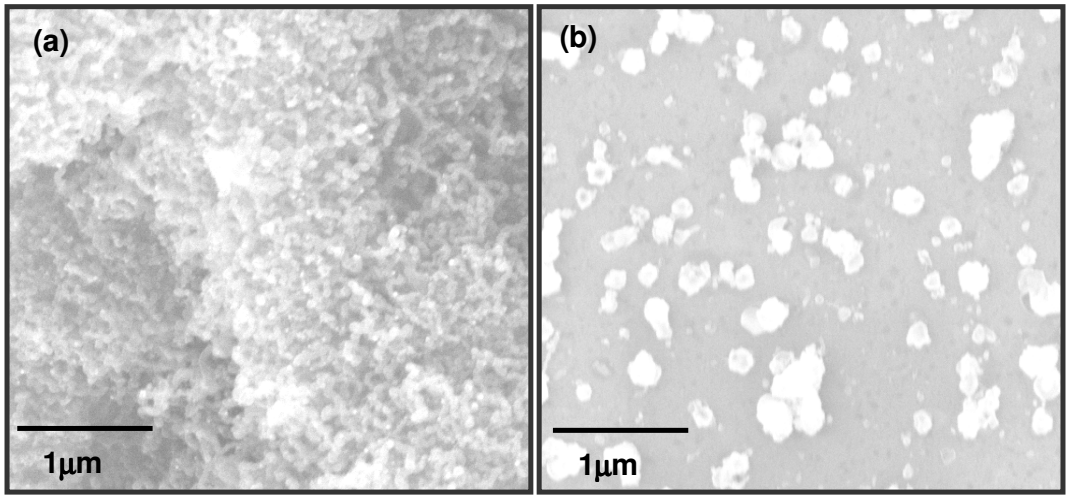

Figure 4.5: SEM micrographs of structures formed at: (a) 400 °C and (b) 700 °C

SEM and TEM micrographs indicated that CNTs containing impurities and defects were formed between 500 and 600 °C with a diameter range corresponding to that of the Ni nano-islands, in agreement with previously reported results [4.2 – 4.4]. The CNT material synthesized at 500 and 600 °C had similar amounts of impurities, defects densities and diameter range. However, the CNTs grown at 500 °C appeared to be greater in length. This difference in length is explained below.

CNT growth occurs by the diffusion-driven precipitation of carbon from the supersaturated catalyst particles [4.2]. Thus at 500 °C the diffusion rate of the carbon molecules into the Ni clusters to form CNTs is at an optimum value, which promotes the growth of long strands of nanotubes. Furthermore, it is also reasoned that at 500 °C minimal amounts of stress act on the graphitic tube during the growth process. This prevents the formation of buckling and folding effects of the CNT walls, which can hinder the growth of the CNTs. Therefore it is concluded that 500 °C appears to be the optimum furnace temperature for the synthesis of MWCNTs with lengths in the micrometer range.

4.3.2.2 Effect of the Deposition Pressure on the Carbon Nanotube Morphology

In the previous section it was shown that CNTs were successfully grown at furnace temperatures of 500 and 600 °C, respectively with 500 °C the most favourable temperature for the growth of CNTs with lengths up to 50 µm. In this section the focus will be on the influence of the deposition pressure (P_{dep}) on the CNT morphology (series B).

The SEM micrographs shown in Figure 4.6 are that of CNT structures grown at deposition pressures of 150 and 200 Torr, respectively, with all other parameters fixed at the standard deposition conditions. From Figure 4.6 (a) it is observed that long strands of MWCNTs with a diameter range between 10 and 100 nm are synthesized at 150 Torr, whereas the CNTs grown at 200 Torr have a greater diameter range. In comparison to the CNTs grown at the standard deposition parameters, it is noticed that the CNTs grown between 150 and 200 Torr contain less impurities and defects. The entanglement of the tubes also appears greater than was the case in Figure 4.2, implying that the CNT length is also greater between this pressure range.

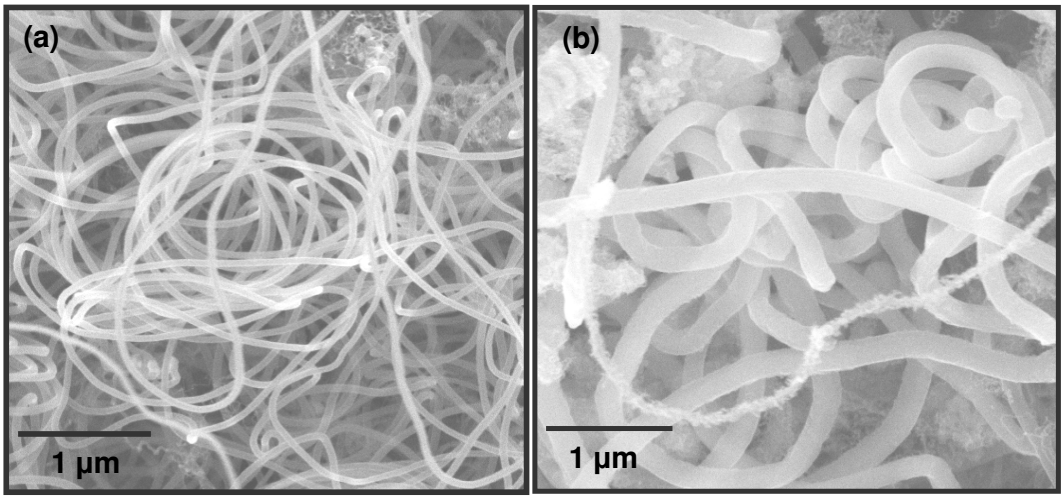

Figure 4.6: SEM micrographs of CNTs grown at (a) 150 Torr and (b) 200 Torr

Figure 4.6 also shows the presence of small agglomerates at the tip of the CNTs. Energy dispersive analysis (EDS) performed on a selected area of Figure 4.6 (a) confirmed the presence of small amounts of Ni (see Figure 4.7). Hence it can be concluded that the agglomerates at the tip of the CNTs are indeed Ni nano-islands, which confirms that the CNTs are formed via the tip-growth method.

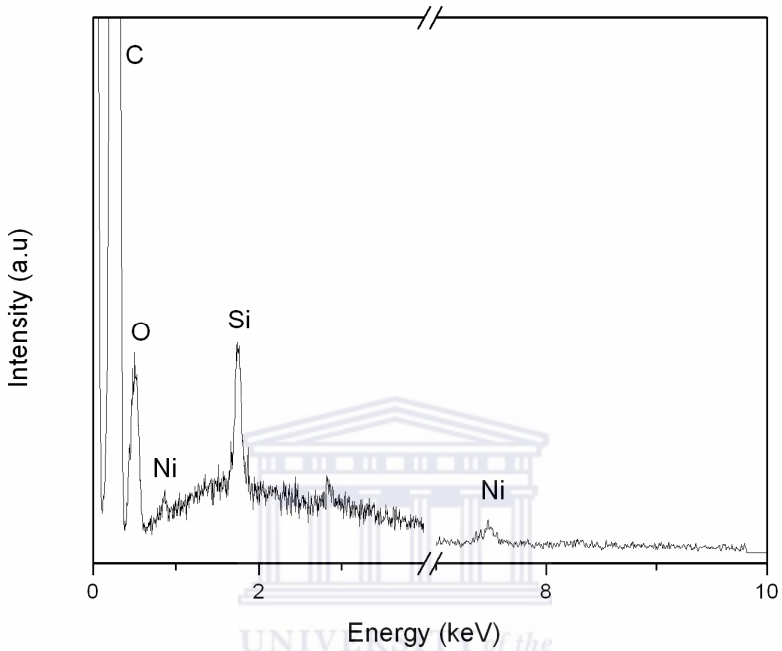

Figure 4.7: EDS spectrum of an area in Figure 4.6 (a) that contains CNTs

The SEM micrographs shown in Figure 4.8 were taken of structures grown at 50 and 400 Torr, respectively. It cannot be said with certainty whether the structures in Figure 4.8 (a) are indeed CNTs. However, the Ni clusters situated at the tips of these structures indicate that these might still be CNTs. Raman spectroscopy, which will be discussed in the next chapter, will resolve this argument. In contrast, the SEM micrograph of Figure 4.8 (b) clearly shows that MWCNTs, with a diameter range between 20 and 100 nm are grown at a deposition pressure of 400 Torr. However, these CNTs appear to contain greater amounts of impurities and defects, compared to the CNTs grown between 100 and 200 Torr. Furthermore, it can also be seen that these

MWCNTs are shorter in length than that of the CNTs grown between 100 and 200 Torr.

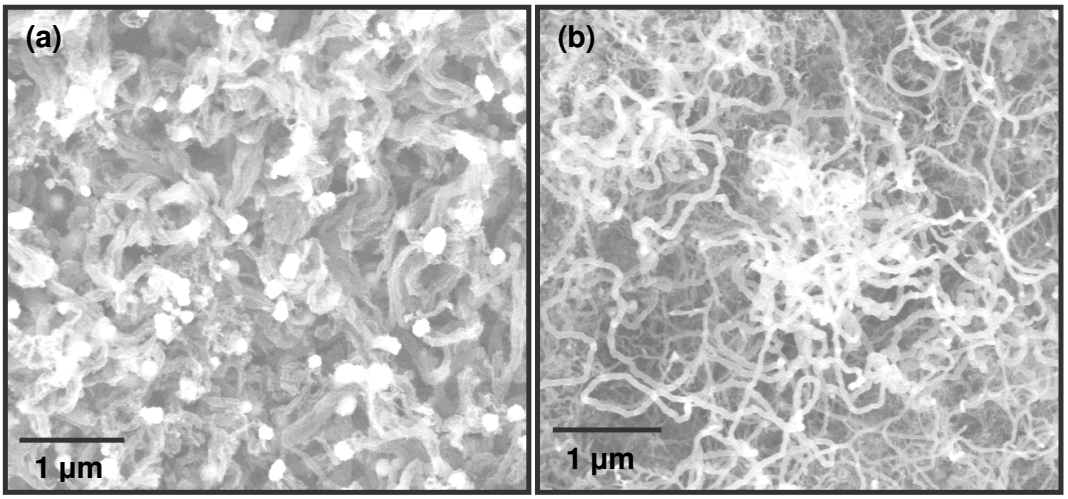

Figure 4.8: SEM micrographs of structures synthesized at (a) 50 and (b) 400 Torr

The results of Figures 4.6 and 4.8 clearly show that deposition pressures between 150 and 200 Torr are ideal for the growth of MWCNTs with minimal defects and impurities in the deposited material, as well as lengths in excess of 20 µm. The effect of the deposition pressure on the resulting CNT morphology is explained in the following manner.

During the growth process of the CNTs the methane molecules decompose over the tungsten filament into reactant carbon and hydrogen radicals, as well as other species such as carbon and hydrogen ions. The carbon then dissolves into the Ni nano-islands, after which it diffuses either on the catalyst surface or through the bulk of the Ni particle upon saturation. Hence, when the concentration of methane is too high, i.e. more carbon is supplied than is needed; the decomposition rate of the carbon source is higher than the precipitation rate of the carbon, which results in an oversupply of carbon in the form of amorphous and/or crystalline carbon [4.7].

In this study the deposition pressure determines the concentration of the carbon feed gas, i.e. methane. At high deposition pressure, there is an oversupply of carbon, resulting in the formation of more carbonaceous nano-material (see Figure 4.8 (b)), in accordance with the argument developed above. Furthermore, at low deposition pressures not enough methane is supplied for ideal precipitation of the carbon on the Ni nano-islands. Hence, the CNT growth rate is hampered, often resulting in non-CNT structures (see Figure 4.8 (a)). In between these two extremes there is an optimum supply of methane gas (pressure) that complements the precipitation of the carbon atoms on the Ni particles. In this study this pressure range is found to be between 150 and 200 Torr, since CNTs of long length and minimal impurities are form between these pressures.

4.3.2.3 Effect of the Methane/Hydrogen Dilution on the Carbon Nanotube Morphology

In this section the effect of the methane/hydrogen dilution, f_{CH4} on the resulting CNT morphology will be studied. This parameter is of importance since it has been shown that the hydrogen plays a major role in the growth process of CNTs [4.8 – 4.10].

Figure 4.9 shows SEM micrographs of densely grown CNT structures, formed at f_{CH4} = 0.16 and 0.67, respectively. From Figure 4.9 it can be estimated these CNTs are multi-walled with a diameter range between 10 and 100 nm and length noticeably shorter than that of the CNTs grown at the standard conditions. Figure 4.9 (a) shows that a considerable amount of impurities, including amorphous carbon material, is inhabited within the deposited material.

In contrast, the MWCNTs grown at f_{CH4} = 0.67 (Figure 4.9 (b)), shows a remarkable decrease in the aforementioned impurities. More interestingly, coiled nano-structures are observed at this dilution ratio, as indicated by the arrow. The structures indicated by the arrow in Figure 4.9 (b) are not very common and only a few groups have previously reported its synthesis [4.11,

4.12]. These three-dimensional (3D) spring-like structures are called carbon microcoils (CMCs) and are found in single (SHCMCs), as well as double-helix form (DHCMCs). The micro in the name refers to the micrometer-sized lengths that these structures can attain during its growth process; CMCs are synthesized via the HWCVD technique in a similar process to that of CNTs. As a result of their unique spring-like form, these CMCs possess many potential applications, including tactile sensors, electronic or electromagnetic nano-devices, of special interest in a micro-electromechanical system [4.12]. These interesting structures will be a subject of further study by our research group.

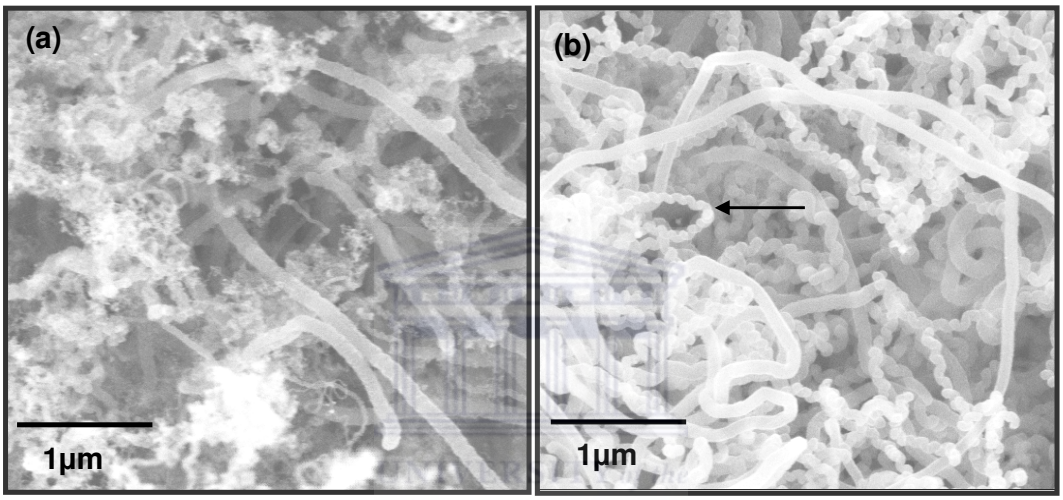

Figure 4.9: SEM micrographs of CNTs grown at a methane/hydrogen gas mixture ratio of (a) 0.16 and (b) 0.67

Figure 4.10 shows the SEM micrograph of very dense and entangled CNTs grown with pure methane gas, i.e. $f_{CH4} = 1$. It can be seen from Figure 4.10 that these CNTs are of similar length but have superior diameters to that of the CNTs grown at the conditions of Figure 4.9. However, it is noticeable that the deposited material of Figure 4.10 contains more impurities and carbonaceous nano-material than that of Figure 4.9 (b). Therefore, based on the SEM micrographs of Figures 4.9 and 4.10 it appears that the hydrogen concentration in the feed gas plays an important role in the CNT growth process.

Chen *et al*. [4.10] states that hydrogen prevents the deactivation of the catalyst and enhances thermal stability of the synthesized CNTs as well as the degree of graphitization of the CNTs, subsequently leading to the formation of impurity-rid CNTs.

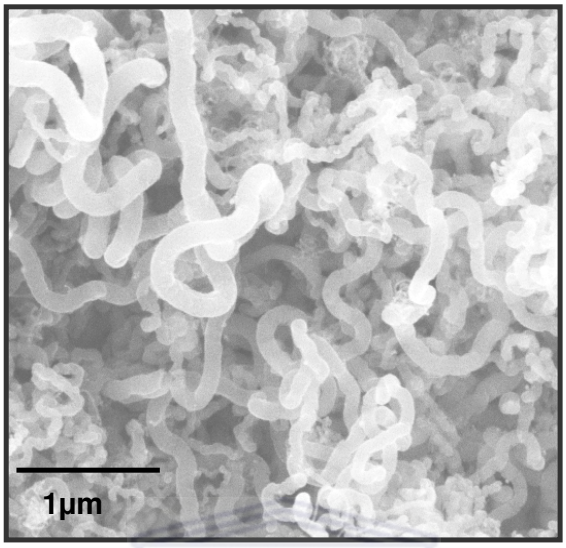

Figure 4.10: SEM micrograph of MWCNTs grown with only methane in the feedstock gas

However, the SEM micrograph of Figure 4.9 shows that a high concentration of hydrogen in the feed gas leads to CNTs containing high levels of impurities. Similarly Figure 4.10 shows that low purity CNTs are grown with pure methane as the feed gas. In contrast, a low concentration of hydrogen in the feed gas leads to the synthesis of CNTs and CMCs with minimal impurities and micrometer-sized lengths. This suggests that a high concentration of hydrogen gas ineffectively prevents the deactivation of the Ni nano-islands, whereas in the absence hydrogen the Ni nano-islands deactivate, thus hampering the formation of the CNT structures; hence the increased impurities in the deposited material. Therefore it can be concluded that a methane/hydrogen dilution of 0.67 contains optimum amounts of hydrogen, which effectively prevents the deactivation of the Ni nano-islands and promotes the growth of CNTs of low impurity and micrometer-sized lengths.

4.3.2.4 Effect of the Substrate-to-Filament Distance on the Carbon Nanotube Morphology

The distance between the c-Si substrate and the tungsten filament, d_{s-f} is an important parameter to consider in the synthesis of CNTs via HWCVD for it determines the eventual species of material that will react with the Ni nano-islands to form CNTs. In this section, the effect of this parameter on the CNT morphology will be the topic of discussion.

Figure 4.11 shows SEM micrographs CNTs grown at d_{s-f} = 10 cm. Figure 4.11 (a) shows the presence of cracks in the deposited material, which is ascribed to poor adhesion of the deposited material to the SiO_2/Si substrate [4.13]. Emerging from these cracks are CNTs aligned in a mat-like structure, up to 20 µm long, as can be seen from Figure 4.11 (b) and (c). Furthermore, judging from the diameter range, it can be concluded that these CNTs are multi-walled. Figure 4.11 (a) also shows that these aligned CNTs are covered with an amorphous carbon as identified by Porro *et al*. [4.14]. At substrate-to-filament distances less than 10 cm randomly orientated CNTs were grown; e.g. Figure 4.12 shows an SEM micrograph of entangled CNTs grown at d_{s-f} = 9 cm.

The alignment of the MWCNTs is attributed to the strong interaction of Van der Waals forces acting between closely grown CNTs. The closely grown CNTs on the other hand, are a result of densely populated Ni nano-islands on the substrate surface [4.10]. In the previous section it was stated that the hydrogen prevents the deactivation of the Ni nano-islands and also acts as an etching agent for nanometer-sized catalyst particles. At 10 cm, as compared to shorter distances, the probability for secondary reactions to occur between radicals increases as a result of the longer path that each radical has to travel to the substrate. Hence, it is proposed that from these secondary reactions, favourable hydrogen species form, which eventually promotes densely situated Ni nano-islands. Therefore, during the growth process, the graphitic tubes grow on these densely populated Ni nano-islands and are aligned by the interaction of strong Van der Waals forces between the tubes.

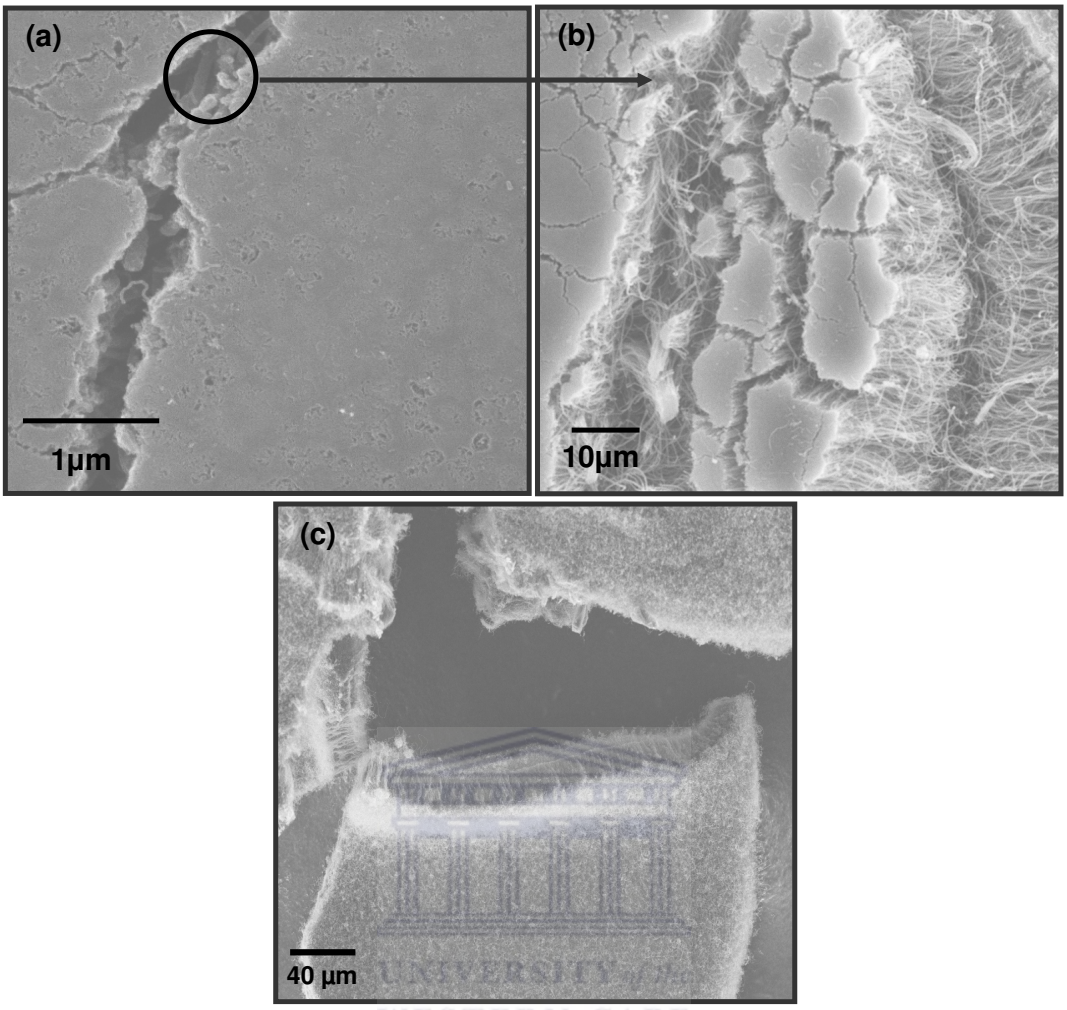

Figure 4.11: SEM micrographs of aligned MWCNTs grown at $d_{s\text{-}f}$ = 10 cm

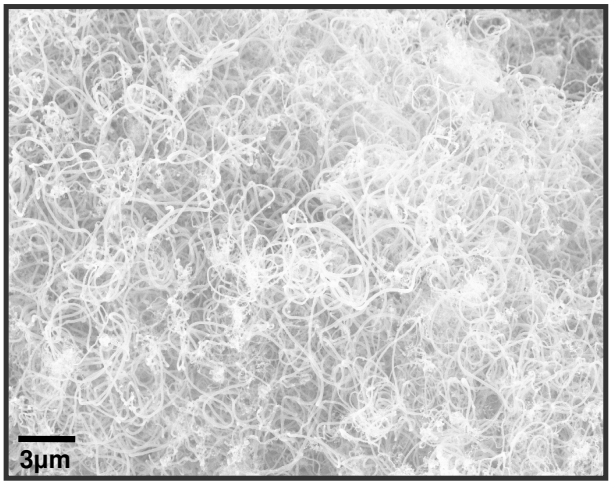

Figure 4.12: Entangled MWCNTs grown at $d_{s\text{-}f}$ = 9 cm

In summary, in this section it was shown that entangled MWCNTs formed at substrate-to-filament distances less than 10 cm. However the SEM micrographs of Figure 4.11 show that mat-like aligned MWCNTs covered by an amorphous carbon layer were grown at a substrate-to-filament distance of 10 cm. Furthermore, it was shown that the deposited material cracked as a result of poor adhesion. The alignment of the CNTs was attributed to the densely populated Ni nano-islands forming at 10 cm, which result in dense CNT growth. The tubes are then aligned by the interaction of Van der Waals forces acting between the CNTs. The density of the particles at 10 cm was ascribed to the formation of favourable hydrogen species from secondary reactions, which etches the Ni particles into closely packed nano-islands.

4.4 Summary

In this chapter the effect of the Ni catalyst preparation and deposition parameters on the carbon nanotube morphology were investigated. The results presented showed that multi-wall carbon nanotubes were formed with the underlying HWCVD system.

Nickel films, of 10 nm thickness, were deposited onto Si/SiO_2 substrates via resistive evaporation, after which it was annealed at temperatures between 400 and 700 ºC, for 20 minutes in a nitrogen gas atmosphere in order to form Ni nano-islands. The SEM micrographs shown in Figure 4.1 reveal that Ni nano-islands only formed at annealing temperatures of 500 and 600 ºC, respectively. In contrast, the samples annealed at 400 and 700 ºC did not produce nano-islands; instead at 400 ºC the Ni film remained intact, whereas at an annealing temperature of 700 ºC the Ni film underwent thermal shock and flaked from the substrate surface. The formation of the nano-islands was attributed to the surface tension at the interface between the Ni film and the Si/SiO_2 substrate, as well as the compressive stress due to the mismatch of the thermal expansion coefficients of the Si/SiO_2 substrate and the Ni film [4.2, 4.3]. Consequently, it was concluded that at 400 ºC, the temperature is insufficient

for adequate compression of the Ni film, whereas at 700 ºC the temperature is so high that the Ni film undergoes a 'thermal shock' resulting in the flaking of the Ni film rather than agglomeration into nano-islands.

The SEM micrographs of Figure 4.2 and 4.4 showed that entangled MWCNTs formed between furnace temperatures of 500 and 600 ºC, respectively. In contrast, the micrographs of Figure 4.5 showed that no CNTs formed at 400 and 700 ºC, respectively, thereby confirming that Ni nano-islands are needed for the growth of CNTs. In addition, the diameter range of these MWCNTs was similar to that of the Ni nano-islands, in agreement with reported results [4.2 – 4.4]. The TEM micrographs of Figure 4.3 showed the presence of Ni nano-particles within as well as at the tips of the CNTs, confirming that the CNTs formed via the tip-growth method. The micron-sized lengths of the MWCNTs in addition to the low impurity levels of the deposited material synthesized at 500 ºC resulted in this temperature being identified as the optimum deposition temperature. These favourable attributes of the CNTs grown at 500 ºC were argued to be a result of an optimum carbon diffusion rate as well as minimal amounts of stresses acting on the graphitic tube during the growth process.

The results of Figure 4.6 showed that deposition pressures between 150 and 200 Torr are ideal for the growth of MWCNTs with minimal defects and impurities, as well as lengths in excess of 20 µm. On the contrary, at deposition pressures of 50 and 400 Torr (see Figure 4.8) CNT structures containing increased amounts of impurities as well as defects are synthesized. The structures grown at a deposition pressure of 50 Torr could not be identified as CNTs; hence Raman spectroscopy will be employed to clarify this issue. Furthermore, the EDS spectrum of Figure 4.7 confirmed that the nano-particles observed at the tips of the MWCNTs in Figure 4.6, are indeed Ni nano-islands. This led to the conclusion that the MWCNTs formed via the tip-growth method during the growth process. The results of Figures 4.6 – 4.8 showed that at high deposition pressure, there is an oversupply of carbon, resulting in the formation of more carbonaceous nano-material (see Figure 4.8 (b)), whereas at low deposition pressures not enough methane is supplied for ideal precipitation of

the carbon on the Ni nano-islands. Hence the conclusion that at deposition pressures between 150 and 200 Torr, optimum amounts of methane gas are supplied to the system which complements the precipitation rate of the carbon atoms on the Ni nano-particles.

The SEM micrographs shown in Figures 4.9 and 4.10 illustrated that small concentrations of hydrogen gas are needed for the synthesis of CNTs with nominal impurities; see Figure 4.9 (b). These results demonstrated that a high concentration of hydrogen ineffectively prevents the deactivation of the Ni nano-islands, resulting in the formation of amorphous carbon and other impurities in the deposited material. In contrast, in the absence of hydrogen gas molecules the Ni nano-islands deactivated, thus hampering the formation of the CNT structures. However at f_{CH4} = 0.67 optimum amounts of hydrogen is supplied to effectively prevent Ni nano-island deactivation and also promote graphitic tube formation.

More interestingly, at a methane/hydrogen dilution of 0.67 it was shown that 3D spring-like structures, capable of growing lengths in the micrometer range, are formed. These structures, which pose many novel applications, are termed carbon microcoils. The CMCs are synthesized either in single or double-helix form via the HWCVD, thereby again illustrating the versatility of the technique. The synthesis and characterization of these structures will be a subject of further study by our research group.

Finally, the effect of the substrate-to-filament distance, d_{s-f} on the CNT morphology was studied in section 4.3.2.4. The results of this section showed that at d_{s-f} less than 10 cm entangled CNTs are formed (see Figure 4.12), similar to that grown at the other deposition parameters. However, at d_{s-f} = 10 cm, it was shown that MWCNTs, aligned in a mat-like structure are grown. These aligned CNTs, which hold great promise in field-emission devices, grew up to 20 µm in length and is covered by an amorphous carbon layer. The alignment of the CNTs was attributed to densely populated Ni nano-islands forming at 10 cm, which result in dense CNT growth. The tubes are then

aligned by the interaction of Van der Waals forces acting between the CNTs. The density of the particles at 10 cm was ascribed to the formation of favorable hydrogen species from secondary reactions, which etches the Ni particles into closely packed nano-islands.

References

[4.1] T. D. Makris, R. Giorgi, N. Lisi, L. Pilloni, E. Salernitano, F. Sarto and M. Alvisi, Diamond and Related Materials, **13** (2004) 305

[4.2] S. Honda, Y.-G. Baek, K.-Y. Lee, T. Ikuno, T. Kuzuoka, J.-T. Ryu, S. Ohkura, M. Katayama, K. Aoki, T. Hirao and K. Oura, Thin Solid Films, **464** (2004) 290

[4.3] Y. M. Shin, S. Y. Jeong, H. J. Jeong, S. J. Eum, C. W. Yang, C. Y. Park and Y. H. Lee, Journal of Crystal Growth, **271** (2004) 81

[4.4] Y. Y. Wei, G. Eres, V. I.Merkulov and D. H. Louwndes, Applied Physics Letters, **78** (2001) 1394

[4.5] P. J. F. Harris, '*Carbon Nanotubes and Related Structures: New Material for the 21st Century* ', Cambridge University Press, Cambridge, (1999)

[4.6] M. A. J. Veld, M. Daenen, R. D. De Fouw, B. Hamers, P. G. A. Janssen and R. Schouteden, 'The Wondrous World of Carbon Nanotubes: A Review of Current Carbon Nanotubes Technologies', Eindhoven University of Technology, Eindhoven, (2003)

[4.7] G. Y. Xiong, Y. Suda, D. Z. Wang, J. Y. Huang and Z. F. Ren, Nanotechnology, **16** (2005) 532

[4.8] M. R. Maschmann, P. B. Amama, A. Goyal, Z. Iqbal, R. Gat, T. S. Fisher, Carbon, **44** (2006) 10

[4.9] Y. J. Yoon and H. K. Baik, Diamond and Related Materials, **10** (2001) 1214

[4.10] C.-M. Chen, Y.-M. Dai, J. G. Huang and J.-M. Jehng, Carbon, **44** (2006) 1808

[4.11] S. Yang, X. Chen, T. Katsuno, Y. Nitta, M. Hasegawa and S. Motojima in '*Preparation of carbon microcoils by catalytic methane hot-wire CVD process*' 4th International Conference on Hot-Wire CVD (Cat-CVD) Process, (2006)

[4.12] X. Chen, S. Yang, I. Ozeki, T. Katsuno and S. Motojima in '*Preparation of single-helix carbon microcoils by catalytic CVD process*' 4th International Conference on Hot-Wire CVD (Cat-CVD) Process, (2006)

[4.13] L. T. T. Tuyen, P. N. Minh, E. Roduner, P. T. D. Chi, T. Ono, H. Miyashita, P. H. Khoi and M. Esashi, Chemical Physics Letters, **415** (2005) 333

[4.14] S. Porro, S. Musso, M. Giorcelli, A. Chiodoni and A. Tagliaferro, "*Optimization of a thermal-CVD system for CNT growth*", Physica E (2006)

CHAPTER FIVE

Structural Properties

5.1 Introduction

The remarkable properties of CNTs so often reported in literature are a direct result of their unique structure, i.e. diameter, chirality and length. Some of these properties include high electrical and thermal conductivity, high tensile strength and good field emission properties, amongst other. Because of these properties CNTs have been considered as components in various device applications stretching from the microelectronic to the biomedical industry [5.1].

However, presently researchers worldwide are unable to directly control the structural properties of CNTs and thus this remains a topic of intense research. At the heart of this dilemma is the inability to accurately control the deposition parameters for the growth of CNTs. Raman spectroscopy is a very powerful technique for gathering information regarding the CNT structure. Furthermore, x-ray diffraction (XRD) has proven to be a complementary technique to Raman spectroscopy in the study of the structure of the carbon nanotube. The XRD technique is often used to probe the degree of purity of the raw CNT samples, as well as identify the presence of the metal catalyst particles entrapped within and at the tips of the CNTs [5.2].

The SEM micrographs of chapter 4 showed that the material deposited via the HWCVD system contains a combination of CNTs, amorphous material, as well as other carbonaceous nano-structures (the latter collectively referred to as disorder), all of which contribute to the line-shape of the resulting Raman spectroscopy and XRD spectra. The aim of this chapter will be to investigate the effect of the deposition parameters on the structure of the resulting CNTs by means of Raman spectroscopy and XRD.

5.2 Experiment

In this study Raman spectroscopy and x-ray diffraction (XRD) were used to investigate the effect of the deposition parameters on the structural properties of the carbon nanotubes. The Raman measurements were performed with a Jobin-Yvon T64000 micro-spectrometer. The micro-spectrometer is operated in triple monochromator mode and is equipped with a 514.5 nm Ar^+ laser in reflective geometry. The laser is set at 1.24 mW at the source. The spectra were run between 1106 and 1700 cm^{-1} at a step size of 0.60 cm^{-1}. The XRD spectra were recorded with a Phillips PW 1830 x-ray powder diffractometer operating at 45 kV and 40 mA, respectively. Copper (Cu) $K\alpha_1$ radiation with a wavelength of 1.5406 Å was used as the x-ray source. The samples were run from 5° to 90°, at a step size of 0.02°, each timed for 5 seconds.

5.3 Results and Discussion

5.3.1 Effect of the Furnace Temperature on the Carbon Nanotube Structure

Raman spectroscopy analysis of crystalline graphite leads to a sharp vibration mode at 1580 cm^{-1} as a result of sp^2 hybridized carbon domains and is named the G-band; the peak at approximately 1350 cm^{-1} is considered to represent a more disordered structure and is labeled as the D (disordered) band [5.3]. For CNTs the G-band shifts between 1550 and 1605 cm^{-1} [5.4]. In this study the disorder refers to impurities such as amorphous carbon in the deposited material and structural defects, including vacancies, grain boundaries, interstitial carbons and buckling (folding) effects within the CNT structure. In chapter 3 it was shown that single-wall carbon nanotubes (SWCNTs) have unique features between 100 and 500 cm^{-1}, which are attributed to the 'radial breathing mode' (RBM) of the tubes and allow for the determination of the tube diameter.

However, the Raman spectra shown in Figure 5.1 of CNTs grown at furnace temperatures of 500 and 600 ºC show only the presence of the D and G-bands, suggesting that the synthesized tubes are multi-wall carbon nanotubes (MWCNTs). This is in accordance with the deductions made from the corresponding SEM micrographs of Figures 4.2 and 4.4. The relative intensity of the G to D-band (I_G/I_D) and the full-width at half maximum (FWHM) of the two bands are often used as an indication of the quality of the synthesized CNTs. The greater the I_G/I_D value and the narrower the FWHM of the respective bands, the greater the purity and quality of the CNTs. However, in this study it is proposed that the respective bands should be investigated in terms of its area, FWHM, intensity and peak position in order to obtain a greater understanding of the CNT structure. For this reason, each of the spectra in Figure 5.1 was fitted with a Gaussian line-shape; this data is summarized in Table 5.1.

The analysis of the respective bands in Figure 5.1 indicates that the increase in temperature results in an increase in the FWHM and area of the G-band. This suggests that the amount of MWCNTs with a lower degree of structural perfection increased with the increase in temperature. Furthermore, it is noted that the D-band FWHM decreases, but that the area and intensity increases with increasing temperature; this implies that the amount of disorder in the deposited material increased. Combining the analysis of the G and D-bands, it is concluded that the increase in temperature results in an increase in the structural imperfections in the MWCNT structure, as well as an increase in the amount of non-CNT structures in the deposited material.

The morphology study performed in chapter 4 suggested that 500 ºC is the optimum temperature for the deposition of MWCNTs of micrometer-sized lengths and minimal impurities. Combined with the analysis performed on the corresponding Raman spectra, it is concluded that 500 ºC is the optimum furnace temperature for the deposition of MWCNTs, not only of micrometer-sized lengths, but also of high structural perfection.

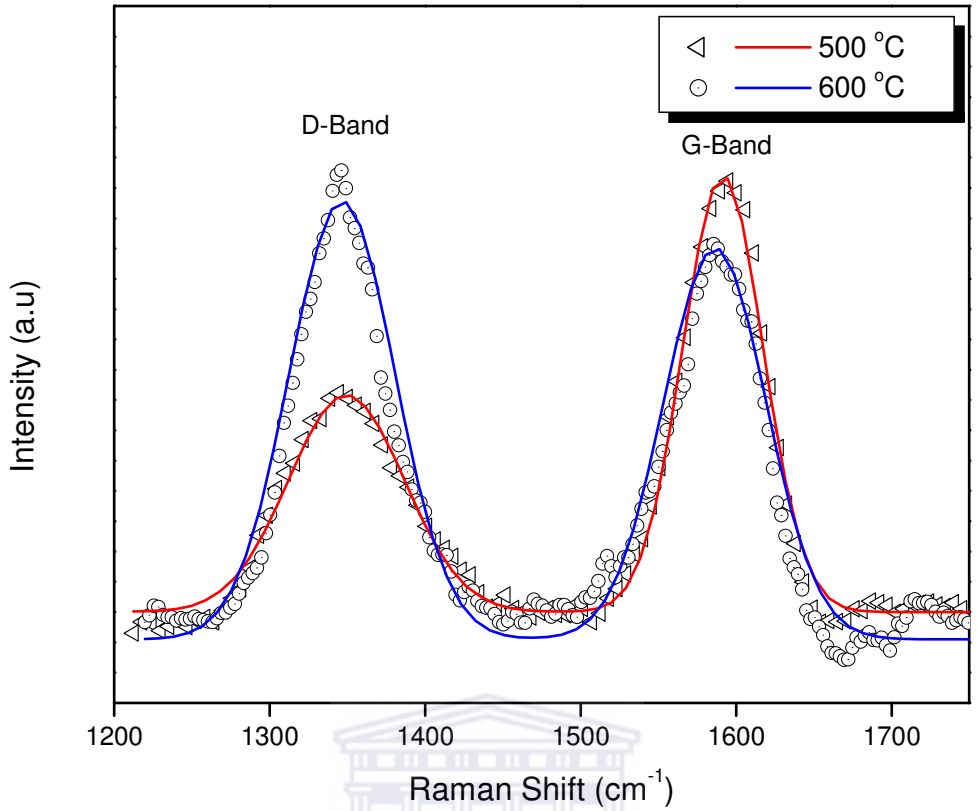

Figure 5.1: Raman spectra of MWCNTs synthesized at 500 and 600 ºC

Table 5.1: Gaussian line-shape data for the Raman spectra of Figure 5.1

	D-Band				G-Band			
Temperature (ºC)	**Area (a.u)**	**Position (cm^{-1})**	**FWHM (cm^{-1})**	**Intensity (a.u)**	**Area (a.u)**	**Position (cm^{-1})**	**FWHM (cm^{-1})**	**Intensity (a.u)**
500	6707	1343	75	72	9358	1594	52	149
600	12344	1346	68	148	10668	1586	66	140

By employing x-ray diffraction MWCNTs are identified by sturdy signals of the graphite (0 0 2) and (1 0 0) orientations at 2θ ~ 26.2 and 43.8º, respectively. Furthermore, the (0 0 2) peak appears asymmetric towards lower angles as a result of the decrease of the inter-wall distance with increasing diameter of the tubes [5.5].

Figure 5.2 (a) and (b) compares the XRD spectra of the CNTs synthesized at 500 and 600 ºC, respectively. The position of the (0 0 2) peak shifts from 25.78 to 26.29º as the temperature is increased from 500 to 600 ºC. Applying Bragg's law of equation 3.4 to this shift in peak position, it is found that the inter-wall spacing of the MWCNTs decreased from 0.345 to 0.339 nm with the increase in temperature. This also suggests that the tube diameter increased in accordance with [5.5]. Figure 5.2 also reveals an increase in the FWHM of the (0 0 2) peak accompanied by an increase in the peak intensity and area with the increase in temperature. This implies an increase in the amount of low crystalline MWCNTs at increased temperatures. This is in accordance with the deductions made from the corresponding Raman spectra and further supports the notion that a furnace temperature of 500 ºC is needed for the deposition of MWCNTs with minimal disorder.

In the previous chapter it was shown that the furnace temperature influences the rate at which the CNTs are formed during the HWCVD process. Following this line of argument it is further deduced that the higher temperature causes a change in the Ni nano-island phase as well as an increase in the atomic mobility of the Ni. Subsequently, this may induce an increase in the nano-island diameter, which then also results in an increase in the MWCNT diameter, as deduced from the XRD spectra of Figure 5.2. Furthermore, apart from the increase in diameter, the change in the nano-island phase also results in the nano-particles becoming 'liquid-like' which promotes the formation of nano-particles and other non-CNT material, i.e. increases the disorder in the deposited material, as observed from the Raman spectroscopy results. Results published by McCaldin *et al*. [5.6] support the arguments formulated above.

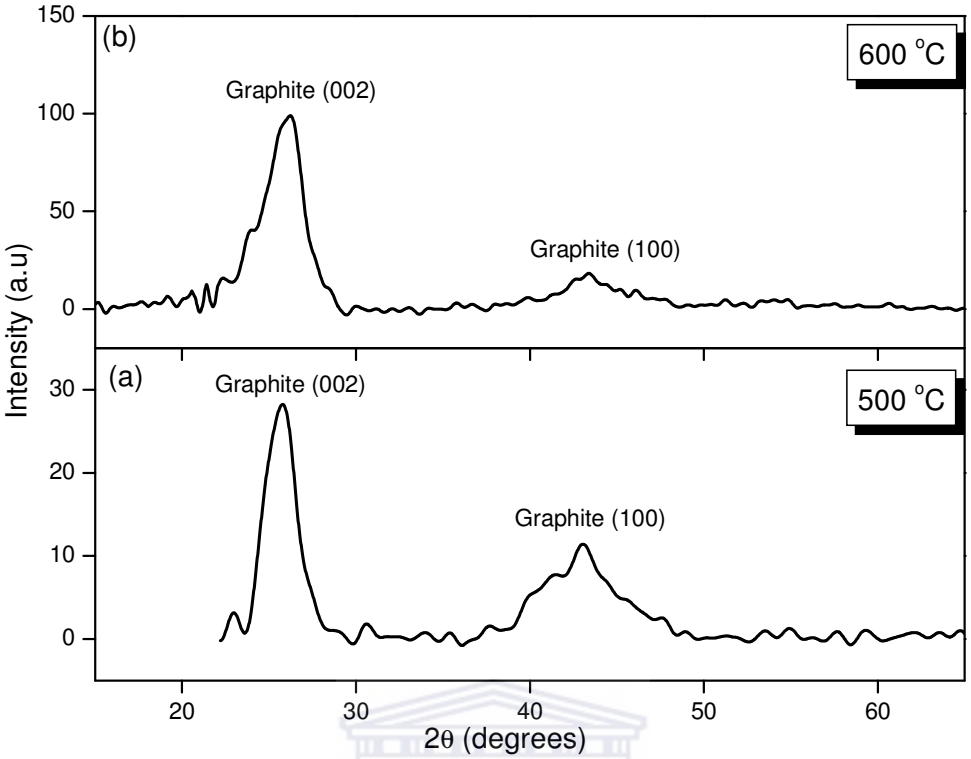

Figure 5.2: XRD spectra of CNTs grown at (a) 500 and (b) 600 ºC

5.3.2 Effect of the Deposition Pressure on the Carbon Nanotube Structure

Figure 5.3 shows Raman spectra fitted with a Gaussian line-shape of CNTs grown at deposition pressures ranging between 50 and 400 Torr. Once again no RBM frequencies were observed for the CNTs grown at any of these conditions, confirming that MWCNTs were synthesized. The data of the fitted Gaussian line-shape is summarized in Table 5.2.

In chapter 4 the SEM micrograph of the material synthesized at 50 Torr, could not clarify whether CNTs were formed. The corresponding Raman spectrum in Figure 5.3 shows that MWCNTs are indeed grown, however, the low signals of the G-band and the relatively strong D-band features (area, intensity and FWHM), suggest that the deposited material is very disordered.

The FWHM of the D-bands show that the distribution of impurities and defects in the deposited material are similar for the MWCNTs grown between 100 and 200 Torr, however there is a decrease in intensity and area of the D-bands. The corresponding FWHM of the G-bands indicates that the CNTs grown at 150 Torr are the least graphitic. Thus it is argued that the disorder in the tubes grown at 150 Torr is more structure-related, i.e. as a result of structural defects such as vacancies and buckling of the tube walls, which decrease the CNT's graphite structural perfection. On the other hand, the disorder in the CNT material grown at 100 and 200 Torr is caused by vibrations from non-CNT material, such as amorphous carbon.

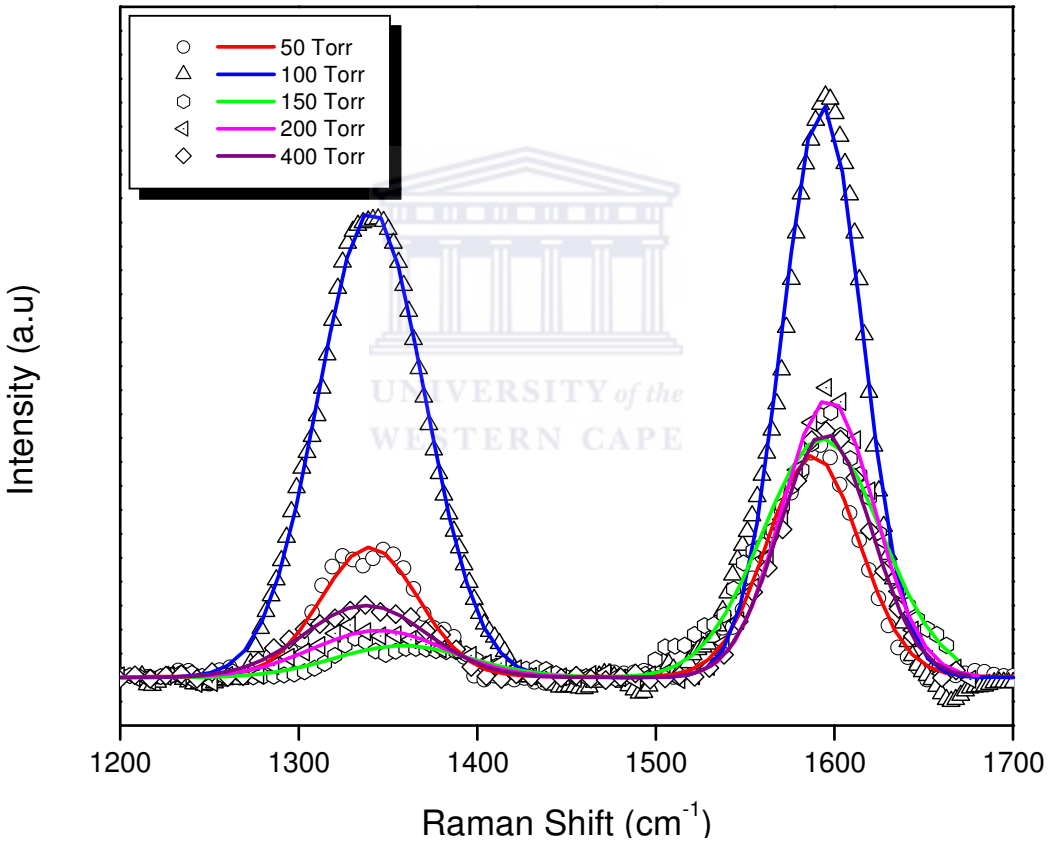

Figure 5.3: Raman spectra of CNTs grown at deposition pressures of 50, 100, 150, 200 and 400 Torr

Table 5.2: Gaussian line-shape data for the Raman spectra of Figure 5.3

	D-Band				G-Band			
Pressure (Torr)	**Area (a.u)**	**Position (cm^{-1})**	**FWHM (cm^{-1})**	**Intensity (a.u)**	**Area (a.u)**	**Position (cm^{-1})**	**FWHM (cm^{-1})**	**Intensity (a.u)**
50	3495	1340	53	53	5857	1592	52	98
100	6707	1343	75	193	9358	1594	52	243
150	1265	1350	75	19	8327	1595	67	112
200	1845	1345	75	20	7553	1597	52	122
400	2602	1338	69	31	6618	1595	52	103

Between deposition pressures of 200 and 400 Torr the G-bands show a decrease in area and intensity, however the FHWM remains similar. This suggests a decrease in the quantity of MWCNTs with the same degree of structural perfection. The corresponding D-bands show a definite increase in area and intensity, accompanied by a decrease in the FWHM, implying an increased amount of disorder in the deposited material. Since the MWCNTs did not lose its degree of structural perfection, it is reasoned that the increase in disorder, between 200 and 400 Torr, is a result of an increase in non-CNT material, such as amorphous carbon.

The XRD spectra shown in Figure 5.4 are that of CNTs grown at deposition pressures of 50, 100 and 400 Torr. Figure 5.4 (a) shows an absence of the graphite (0 0 2) and (1 0 0) peaks as well as the presence of two highly crystalline peaks at 2θ ~ 33º and 62º, respectively. These peaks could not be identified with the JCPDS cards available as either phases forming between the Ni and SiO_2/Si substrate or between the Ni and carbon species, and thus remains a subject of further study.

Since the Raman spectra of Figure 5.3 indicated that MWCNTs are indeed formed at a deposition pressure of 50 Torr, it is reasoned that the absence of the graphitic peaks in Figure 5.4 (a) might be as a result of the parallel alignment of the MWCNTs to the incident x-ray beam. The corresponding SEM micrograph of Figure 4.8 (a) did not show aligned MWCNTs forming at 50 Torr.

However, seeing that the incident electron beam was perpendicular to the surface substrate, it is reasoned that the micrograph shown in Figure 4.8 (a) might be that of the top-view of MWCNTs aligned parallel to the incident beam. These arguments are in accordance with published results by Cao *et al* [5.7].

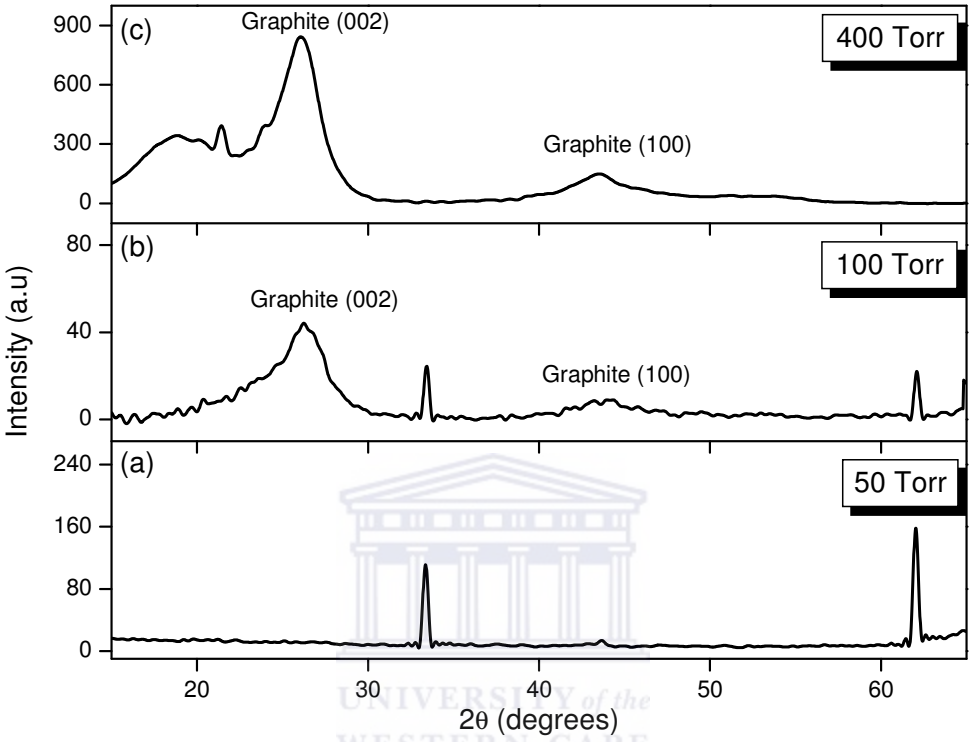

Figure 5.4: XRD spectra of CNT structures formed at deposition pressures of (a) 50, (b) 100 and (c) 400 Torr

The broad FWHM of the (0 0 2) peak in Figure 5.4 (b) as well as the lineshape of the graphite (1 0 0) peak suggest that the material is not highly crystalline. In the discussion of the Raman spectra of Figure 5.3, it was concluded that there is an increase in the defect density of the CNTs grown between 50 and 150 Torr, which ultimately decreases the CNTs' structural perfection. The XRD spectrum of Figure 5.4 (b) confirms the Raman spectroscopy results, by showing a decrease in the graphitic crystallinity of the CNTs grown between the 50 and 150 Torr pressure range.

From the analysis of the Raman spectra it follows that the amorphous carbon material in the sample increased between 150 and 400 Torr. The XRD spectrum of Figure 5.4 (c) shows the presence of a broad hump on the lower angle side of the graphite (0 0 2) peak. Boccaleri *et al*. [5.5] showed that this band results from glassy carbon phases in the deposited material, i.e. amorphous carbon. Hence, in agreement with the Raman analysis it is seen that the amorphous carbon material increases at 400 Torr.

Based on the Raman and XRD results it is concluded that a deposition pressure between 150 and 200 Torr is optimum, since the amount of defects as well as amorphous carbon material in the deposited material is at a minimum. The TEM analysis performed in Chapter four showed that the MWCNTs grew via the tip-growth method, i.e. the carbon molecules diffuse through the nano-island, after which tube growth occurs and the advancing 'face' of the nano-island remains clean during the growth process.

Therefore it is argued that between 150 and 200 Torr an optimum supply of methane gas is supplied to the system. This then results in a decomposition rate of the methane molecules that complements the rate at which the resulting carbon molecules then diffuse through the Ni nano-islands; subsequently leading to the formation of CNTs with minimal structural defects and low amorphous carbon material. In contrast, the high deposition pressures, i.e. 200 to 400 Torr, results in an oversupply of methane to the system, which in turn, results in a decomposition rate of the methane molecule that is higher than the diffusion rate of the carbon molecules through the Ni nano-island surface. This results in an oversupply of the carbon in the form of amorphous carbon. Furthermore, at low pressures the decomposition rate of the methane molecule is insufficient for the precipitation rate of the carbon molecules on the nano-island surface, resulting in the formation of defect-containing CNTs and other nano-structures.

5.3.3 Effect of the Methane/Hydrogen Dilution on the Carbon Nanotube Structure

The role of hydrogen in the growth process of carbon nanotubes via chemical vapour deposition (CVD) is still a topic of intense discussion, since many groups have previously reported varying, and often contradicting results [5.6, 5.8]. In this section the effect of the methane/hydrogen dilution (f_{CH4} defined in equation 1.9) on the structural properties of the CNTs will be investigated by means of Raman spectroscopy and x-ray diffraction. Figure 5.5 below shows Raman spectra (fitted by a Gaussian line-shape) of MWCNT structures grown at a methane/hydrogen dilution varying from 0.08 to 1, i.e. from a high to zero concentration of hydrogen in the feedstock gas composition.

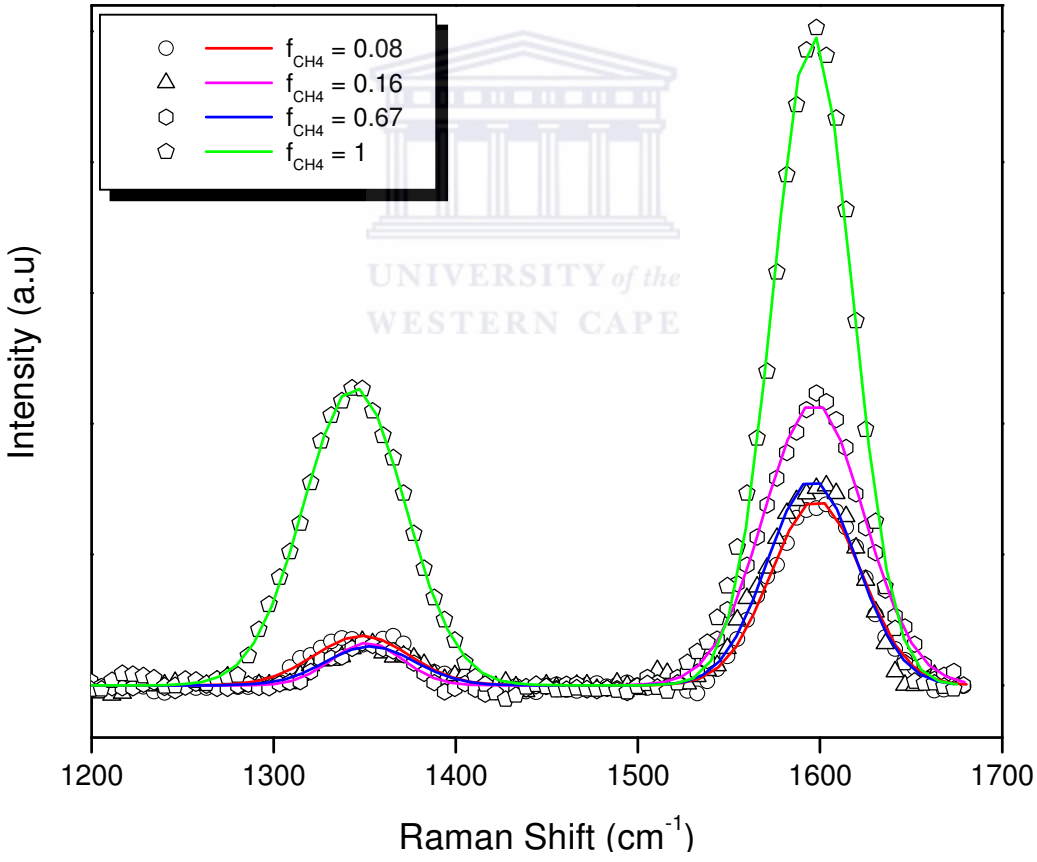

Figure 5.5: Raman spectra of CNTs grown at a methane/hydrogen dilution ranging from 0.08 to 1

Table 5.3: Gaussian line-shape data for the Raman spectra of Figure 5.5

	D-Band				G-Band			
f_{CH4}	Area (a.u)	Position (cm^{-1})	FWHM (cm^{-1})	Intensity (a.u)	Area (a.u)	Position (cm^{-1})	FWHM (cm^{-1})	Intensity (a.u)
0.08	1234	1348	52	19	4417	1598	50	71
0.16	912	1353	49	15	4826	1596	50	78
0.67	791	1351	39	16	7434	1597	55	108
1	7961	1344	56	114	13583	1596	44	249

The results of Figure 5.5 and Table 5.3 show no change in the FWHM of the G-band at f_{CH4} = 0.08 and 0.16, suggesting that the degree of structural perfection of the graphitic MWCNTs remains similar. However, the increase in intensity and area of the respective G-bands suggest that the amount of graphitic material, i.e. CNTs increased. Furthermore, the accompanying decrease in the corresponding D-band area, FWHM and intensity suggest that the amount of non-CNT structures (mostly amorphous carbon material) in the deposited material decreased.

At a methane/hydrogen dilution of 0.67 an increase in the G-band area, FWHM as well as intensity is observed. This suggests an increase in the quantity of MWCNTs with a lower degree of structural perfection. The corresponding SEM micrograph of Figure 4.9 (b) showed the presence of carbon microcoils (CMCs), which might well have contributed to the shape of the Raman spectrum of Figure 5.5. Moreover, the decrease in the D-band area and intensity indicate that the amount of disorder in the material decreased, which is in agreement with the SEM micrograph of Figure 4.9 (b).

The Raman spectrum of the CNT structures grown at f_{CH4} = 1, shows increased signals from the D and G-bands, suggesting that more material was synthesized at these conditions. Furthermore, the decrease in the G-band FWHM indicates that the graphitic structures (MWCNTs) became more ordered. However, the D-band also shows an increase in area, FWHM as well as intensity suggesting an increase in amorphous carbon material in the

deposit. A comparison of the relative ratios of the areas of the various D and G-bands (A_D/A_G), shows that the deposited material at f_{CH4} = 1 contains the greatest ratio of disordered material*.

Figure 5.6 shows the XRD spectra of the CNTs grown at f_{CH4} = 0.08, 0.16 and 1. The increased FWHM of the graphite (0 0 2) peak suggests that the crystallinity of the CNTs decreased with the decrease in the hydrogen concentration of the feedstock gas mixture. The broad band shown in the XRD spectrum of Figure 5.6 (b) at low 2θ angles is attributed to the amorphous carbon in the deposited material [5.5]. No amorphous carbon material is observed at f_{CH4} = 1, however, this can be ascribed to the spot analysis approach of the XRD technique. Furthermore, the graphite (0 0 2) peak position shifts from 25.78º to 26.15º with the decrease in hydrogen concentration, as a result of a decrease in inter-wall spacing of the MWCNTs. The inter-wall spacing decreased from 0.345 (f_{CH4} = 0.08) to 0.340 nm for the MWCNTs grown at f_{CH4} = 1. This also implies that the MWCNT diameter decreased [5.5] with the decrease in hydrogen, in agreement with the observations of the corresponding SEM micrograph of Figure 4.10.

In Chapter Four it was argued that a low concentration of hydrogen gas is needed for the synthesis of CNTs with minimal structural defects an amorphous carbon material in the deposited material. The Raman spectroscopy and XRD results of Figures 5.5 and 5.6 further support this argument by showing increased levels of structural defects (at f_{CH4} = 0.08 and 0.16) and amorphous carbon material at f_{CH4} = 1, respectively.

The hydrogen plays an important role in the morphology of the Ni nano-islands. In-situ studies showed that the shape of the catalyst particles change with variations in the gas environment of the deposition system [5.9]. Furthermore, it is reasoned that the hydrogen chemically binds to the surface of the metal nano-islands thereby weakening the metal-metal bond leading to an induced

* A_D/A_G (f_{CH4} = 0.08) = 0.28
A_D/A_G (f_{CH4} = 0.16) = 0.19
A_D/A_G (f_{CH4} = 0.67) = 0.11

mobility of the surface atoms of the nano-islands i.e. prevents the nano-islands' deactivation. This process is then more favorable for the formation of carbon fibers and less vulnerable to the formation of encapsulating nano-structures [5.8, 5.10]. Thus, it is concluded that a methane/hydrogen dilution of f_{CH4} = 0.67 optimally prevents the deactivation of the Ni nano-islands, thereby promoting the growth of CNT structures with minimal structural defects.

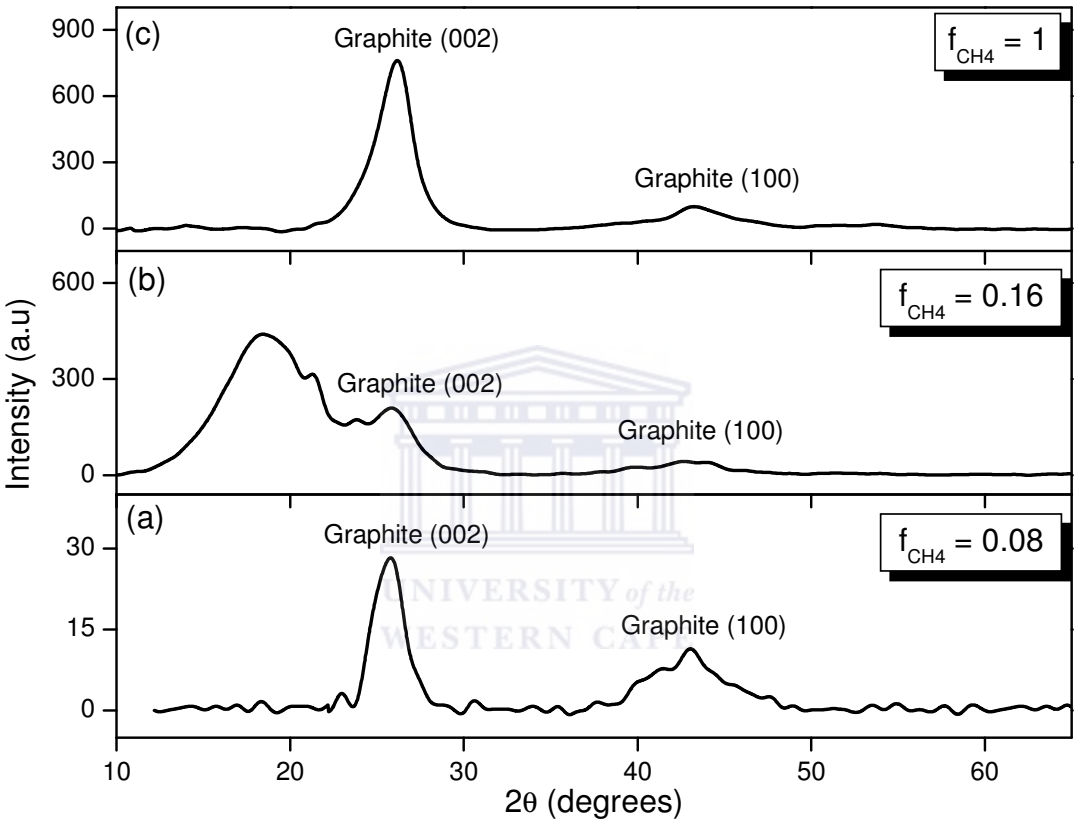

Figure 5.6: XRD spectra of CNTs grown at a methane/hydrogen dilution of (a) 0.08, (b) 0.16 and (c) 1, respectively

A_D/A_G (f_{CH4} = 1) = 0.59

5.3.4 Effect of the Substrate-to-Filament Distance on the Carbon Nanotube Structure

The effect of the substrate-to-filament distance (d_{s-f}) on the structural properties of carbon nanotubes, which is the topic of this section, is not often reported in literature. This is an important parameter to consider during the growth process of CNTs, since it determines the eventual species of material that will form after pyrolisis of the methane/hydrogen gas mixture by the hot filament. Figure 5.7 shows Raman spectra of MWCNTs grown at substrate-to-filament distances ranging between 6 and 10 cm. Each band in the spectrum was fitted with a Gaussian line-shape; the data of which is captured in Table 5.4.

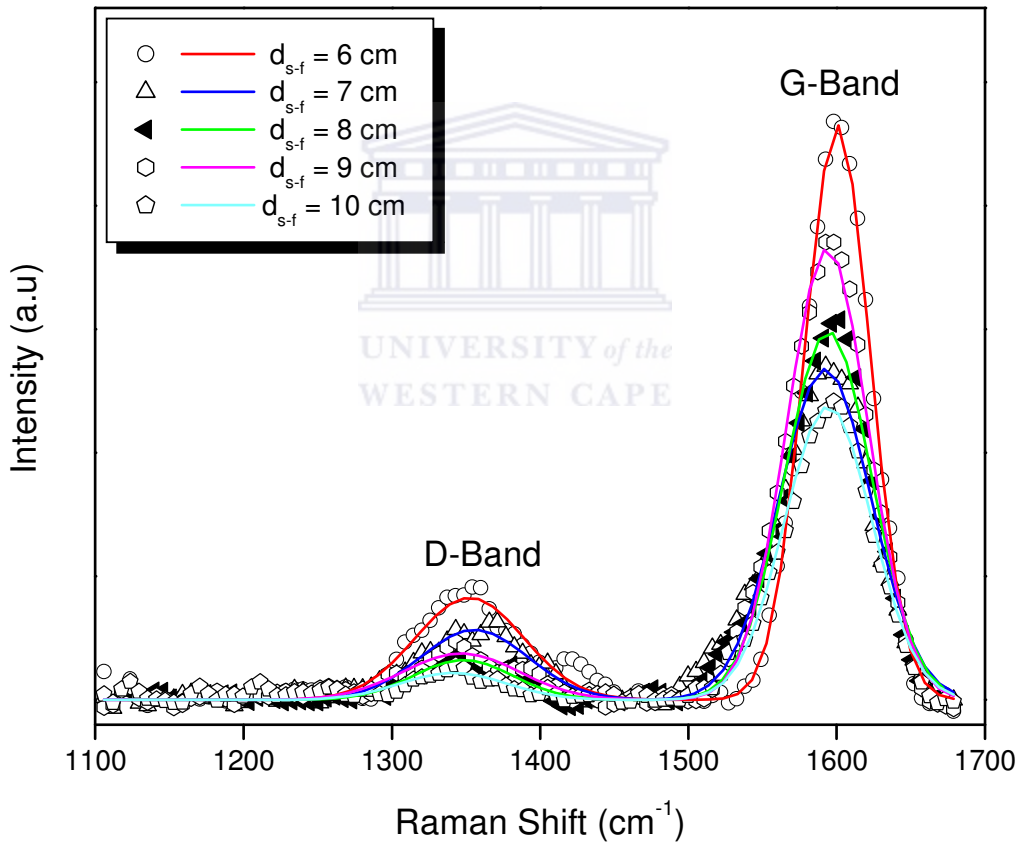

Figure 5.7: Raman spectra of CNTs grown at substrate-to-filament distances ranging between 6 and 10 cm

Table 5.4: Gaussian line-shape data for the Raman spectra of Figure 5.7

	D-Band				G-Band			
d_{s-f} (cm)	Area (a.u)	Position (cm^{-1})	FWHM (cm^{-1})	Intensity (a.u)	Area (a.u)	Position (cm^{-1})	FWHM (cm^{-1})	Intensity (a.u)
6	3794	1352	73	41	12963	1600	44	233
7	2596	1356	73	28	10526	1592	63	134
8	1358	1348	67	16	11030	1594	59	149
9	1847	1347	78	19	12677	1594	55	183
10	978	1342	71	11	8862	1594	59	119

The data of Table 5.4 shows an increase in the FWHM, accompanied by a decrease in intensity and area of the G-band at substrate-to-filament distances between 6 and 7 cm. This implies that the amount of graphitic material (i.e. MWCNTs) not only decreases, but also loses its structural perfection with the increase in d_{s-f} from 6 to 7 cm. The corresponding D-bands show a decrease in intensity as well as area under the curve with the increase in distance, implying that this is not a decrease in the structural defects of the MWCNTs (since the structures become less perfect) but rather a decrease in the amorphous carbon material.

At substrate-to-filament distances between 7 and 9 cm, the G-bands become narrower and are accompanied by an increase in intensity and area covered by the band. This implies an increase in the quantity and structural perfection of the MWCNTs with the increase in d_{s-f}. The corresponding D-bands show variations in their FWHM, intensities as well as areas as a result of varying forms and quantity of disordered material in the deposit.

Table 5.4 shows an increase in the FWHM along with a decrease in intensity and area of the G-band with the increase in d_{s-f} from 9 to 10 cm. The respective D-bands show a decrease in FWHM, intensity and area. These results indicate that the structural perfection of the MWCNTs decreased along with a decrease in the amount of disordered structures in the deposited material as d_{s-f} is increased from 9 to 10 cm. The SEM micrographs of Figure 4.11 showed the existence of aligned MWCNTs covered by an amorphous carbon layer at d_{s-f} =

10 cm. The relative ratios of the D to G-band areas show that minimal quantities of disordered structures are found in the material deposited at 10 cm, in accordance with the alignment of the MWCNTs.

Figure 5.8 shows XRD spectra of CNT structures grown at 6 and 10 cm, respectively. The absence of the graphitic peaks is readily observed for the MWCNTs grown at 6 cm, with only the presence of the two unidentified crystalline phases at 2θ ~ 33 and 62º, as discussed in section 5.3.2. The absence of the graphitic peaks is once again attributed to the possible alignment of the MWCNTs parallel to the incident x-ray beam in agreement with the study performed by Cao *et al*. [5.7].

The SEM images of Figure 4.11 showed that the MWCNTs are not necessarily aligned perpendicular to the substrate surface, i.e. parallel to the incident electron beam, hence the presence of the graphite (0 0 2) peak at 2θ ~ 26º for the aligned MWCNTs grown at d_{s-f} = 10 cm. However, the high noise level of Figure 5.8 (b) do not allow for the identification of the graphite (1 0 0) peak. The asymmetric shape of the (0 0 2) again confirms that the CNTs are multi-walled and the presence of the hump at low 2θ angles is a result of the amorphous layer covering the aligned MWCNTs.

The results of Figures 5.7 and 5.8 suggest that a substrate-to-filament distance of 10 cm is optimum for the synthesis of MWCNTs aligned in a mat-like structure. The Raman spectroscopy results also show minimal amorphous carbon material at d_{s-f} = 10 cm; the greatest contributor being the amorphous carbon material covering the MWCNTs. Thus it is concluded that the increase in d_{s-f} promotes the alignment of the CNTs and a decrease in the disorder of the deposited material.

The alignment is attributed to the interaction of Van der Waals forces acting between the closely grown CNTs. The close proximity of the tubes is a result of densely packed Ni nano-islands.

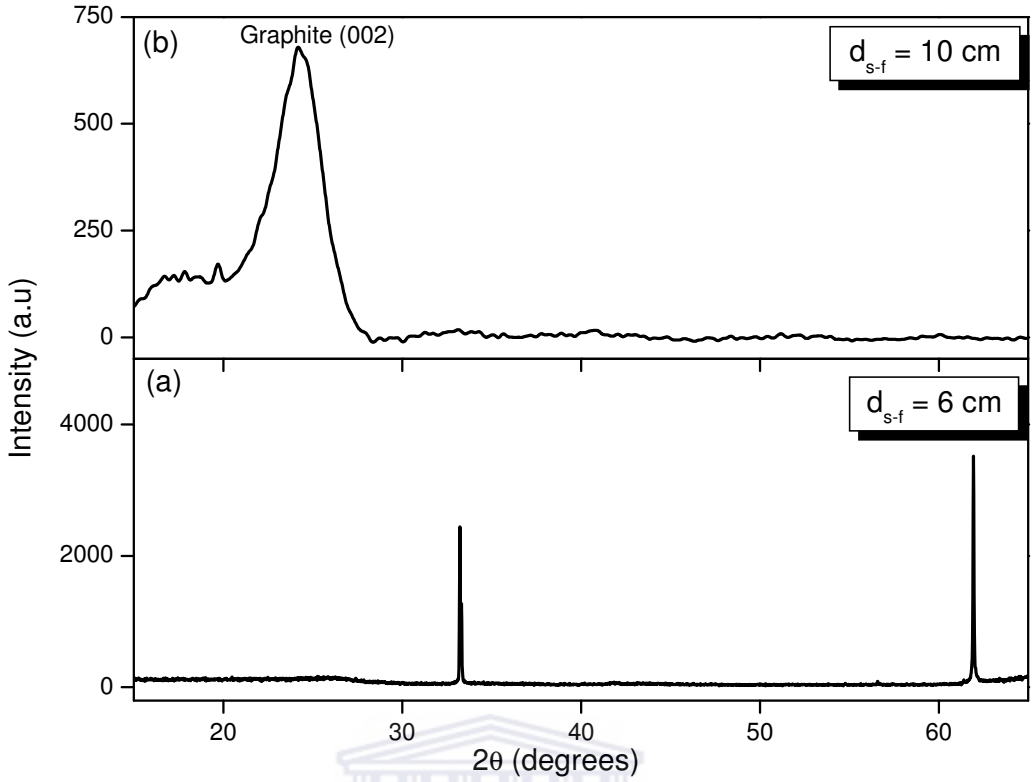

Figure 5.8: XRD spectra of CNTs grown at (a) 6 and (b) 10 cm

Secondary reactions refer to reactions occurring between the species originally formed during the pyrolisis of the methane/hydrogen gas mixture by the hot filament. An increased substrate-to-filament distance means that the species formed via the pyrolisis process have a longer path to travel towards the substrate. This results in an increase in the probability for these species to react with each other via secondary reactions, which could subsequently lead to the formation of different reactant species.

It is argued that at a substrate-to-filament distance of 10 cm, favourable hydrogen species are formed via secondary reactions that absorb over the Ni nano-islands. This weakens the metal-metal bond and subsequently increases the mobility of the surface atoms of the Ni nano-islands. The increased mobility, known as faceting or reconstruction [5.9] then allows the Ni nano-particles to agglomerate into closely packed Ni nano-islands.

5.4 Summary

This chapter investigated the effect of the deposition parameters on the resulting carbon nanotubes' structural properties, using Raman spectroscopy and x-ray diffraction. The parameters that were investigated include the furnace temperature, deposition pressure, methane/hydrogen dilution and the substrate-to-filament distance, d_{s-f}.

Firstly, the effect of the furnace temperature on the CNT structure was investigated. The Raman and XRD results showed that the increase in temperature results in an increase in tube diameter and a decrease in the structural perfection and amorphous carbon in the deposited material. This was argued to be as a result of a change in the Ni nano-island phase and atomic mobility caused by the increase in temperature. Furthermore, it was reasoned that the nano-island phase transition may result in an increase in particle diameter, which then also results in an increased CNT diameter. The increase in temperature also results in the nano-islands becoming 'liquid-like' which promotes the formation of nano-particles and other non-CNT material, i.e. increases the disorder in the deposited material. Hence it was concluded that 500 ºC is the optimum furnace temperature for the deposition of MWCNTs with high structural perfection and minimal amorphous carbon in the deposited material.

Secondly, the study on the effect of the deposition pressure on the CNT structure led to the conclusion that a deposition pressure between 150 and 200 Torr is optimum, since the amount of defects in the MWCNTs as well as amorphous carbon material in the deposited material is at a minimum. Between this pressure range it was shown that an optimum supply of methane gas to the system resulted in a methane decomposition rate that complements the diffusion rate of the carbon molecules through the Ni nano-islands. Furthermore, it was shown that high deposition pressures, i.e. 200 to 400 Torr, result in an oversupply of methane to the system, which in turn results in a decomposition rate of the methane molecule that is higher than the diffusion

rate of the carbon molecules. This results in an oversupply of carbon in the form of amorphous carbon. In contrast, at low pressures the decomposition rate of the methane molecule is insufficient for adequate diffusion of the carbon molecules through the nano-islands to occur, thus resulting in the formation of defect-containing CNTs and other nano-structures.

Thirdly, it was shown that the hydrogen greatly influences the morphology of the Ni nano-islands by chemically binding to the surface of the Ni nano-islands thereby weakening the metal-metal bond leading to an induced mobility of the surface atoms of the nano-islands. It was shown that minimal concentrations of hydrogen, i.e. f_{CH4} = 0.67 are needed for the above process to operate optimally. The Raman and XRD spectra results of Figures 5.5 and 5.6 showed increased levels of structural defects at f_{CH4} = 0.08 and 0.16 respectively and high quantity of amorphous carbon material at f_{CH4} = 1.

Finally, the results of Figures 5.7 and 5.8 suggested that a substrate-to-filament distance of 10 cm is optimum for the synthesis of MWCNTs aligned in a mat-like structure. The alignment was ascribed to the interaction of Van der Waals forces acting between the closely grown CNTs; the close proximity of the tubes being a result of densely packed Ni nano-islands. It was reasoned that at a substrate-to-filament distance of 10 cm, favourable hydrogen species are formed via secondary reactions. These hydrogen species then absorb over the Ni nano-islands thereby weakening the metal-metal bond consequently resulting in an increase in the mobility of the surface atoms of the Ni nano-islands. The increased mobility, known as faceting or reconstruction then allows the Ni nano-particles to agglomerate into closely packed Ni nano-islands.

Hence, it is concluded that the optimum deposition parameters for the HWCVD of aligned MWCNTs with lengths up to 50 μm along with minimal structural defects and amorphous carbon in the deposited material are as follows: a furnace temperature of 500 ºC, deposition pressure ranging between 150 and 200 Torr, methane/hydrogen dilution of 0.67 and a substrate-to-filament distance of 10 cm.

References

[5.1] P. Delhaes, M. Couzi, M. Trinquecoste, J. Dentzer, H. Hamidou and C. Vix-Guterl, Carbon, **44** (2006) 3005

[5.2] Z. Wang, Q. Wu, F. -Y. Zang and Y. -Y. Cui, Materials Letters, In Press (2006)

[5.3] F. Tuinstra and J. L. Koenig, Journal of Chemical Physics, **53** (1970) 1126

[5.4] T. Danis, M. Kadlecikova, A. Vojackova, J. Breza, M. Michalka, D. Buc, R. Redhammer and M. Vojs, Vacuum, **81** (2006) 22

[5.5] E. Boccaleri, A. Arrais, Alberto Frache, W. Gianelli, P. Fino and G. Camino, Materials Science and Engineering B, **131** (2006) 72

[5.6] S. McCaldin, M. Bououdina, D. M. Grant and G. S. Walker, Carbon, **44** (2006) 2273

[5.7] A. Cao, C. Xu, J Liang, D. Wu and Bingqing Wei, Chemical Physics Letters, **344** (2001) 13

[5.8] C.-M. Chen, Y.-M. Dai, J. G. Huang and J.-M. Jehng, Carbon, **44** (2006) 1808

[5.9] C. Park, N. M. Rodriguez and R. T. K. Baker, Journal of Catalysis, **169** (1997) 212

[5.10] W. T. Owens, N. M. Rodriquez and R. T. K. Baker, Journal of Physical Chemistry, 96 (1992) 5048

SUMMARY

Since their discovery in 1991 by Sumio Iijima, carbon nanotubes (CNTs) have shown promise in various potential applications such as catalyst support for fuel cells, micro-sensors, field emission displays, etc. due to their excellent electronic, optical, magnetic and mechanical properties. Carbon nanotubes exist in two forms: single-wall (SWCNTs) and multi-wall carbon nanotubes (MWCNTs), which are usually grown by three main synthesis techniques, namely arc-discharge, laser vaporization and chemical vapour deposition (CVD).

Presently, CNT researchers experience difficulties in the prediction of the growth of CNTs. This stems from the inability to accurately control the deposition parameters of the underlying system. Due to its repeaTable and controllable nature, hot-wire CVD has been identified as a possible solution to this predicament. In addition, HWCVD is also identified as an industrially applied technique since it allows for mass production of CNTs, once optimized.

This study focused on the construction of a HWCVD system and optimizing it for the synthesis of CNTs with micro-sized lengths and high structural perfection. The optimization was achieved by investigating the effects of the deposition parameters on the morphology and structural properties of the CNTs. These parameters were the furnace temperature, which determines the substrate temperature, the deposition pressure, the methane/hydrogen dilution ratio and the substrate-to-filament distance.

The morphology, internal structure an structural properties of the CNTs were investigated using field emission scanning electron microscopy (FESEM), transmission electron microscopy (TEM), Raman spectroscopy and x-ray diffraction (XRD), respectively.

The results of chapters four and five showed that MWCNTs were successfully synthesized and that the deposition parameters had the following effect on the morphology and structure of the tubes:

- *Effect of furnace temperature*: An increase in the furnace temperature results in an increased MWCNT diameter, which is accompanied by an increase in the structural defects of the tubes as well as the concentration of amorphous carbon in the deposited material.

- *Effect of deposition pressure*: Low deposition pressures result in increased levels of structural defects in the MWCNTs, whereas high deposition pressures yield an increase in the amount of amorphous carbon in the deposit.

- *Effect of methane/hydrogen dilution*: High concentrations of hydrogen in the feed gas resulted in an increase in the structural defects of the MWCNTs, whereas no hydrogen in the feed gas led to an increase in the amorphous carbon and other carbonaceous nano-structures in the synthesized material.

- *Effect of substrate-to-filament distance*: Increasing the substrate-to-filament distance promoted the alignment of the MWCNTs in a mat-like structure and is accompanied by a decrease in the structural defects of the tubes as well as the non-CNT structures.

It is therefore concluded that the optimum deposition parameters for the HWCVD of aligned MWCNTs with micro-sized lengths, minimal structural defects and minute quantities of amorphous carbon in the deposited material are as follows: a furnace temperature of 500 ºC, deposition pressure ranging between 150 and 200 Torr, methane/hydrogen dilution of 0.67 and a substrate-to-filament distance of 10 cm.

Future optimization studies of the HWCVD system should include an investigation into the effect of the filament temperature and total flow rate of the methane and hydrogen gas on the CNT morphology and structure. This could not be performed in this study due to limitations in the design of the system. Furthermore, the effect of different types of transition metal catalysts on the growth of CNTs, as well as a method of supplying it to the HWCVD system (i.e. in the gas phase) should also be investigated, seeing that difficulties were experienced in growing SWCNTs.

To obtain greater insight into the growth process of carbon nanotubes, in-situ characterization should be performed. These techniques should include in-situ mass spectrometry (for investigation of the species that forms during the growth process) as well as in-situ laser spectroscopy measurements of the absorbance and thickness profiles of aligned CNTs. In addition, the carbon micro-coils synthesized with the HWCVD system will also be a subject of future studies by our research group.